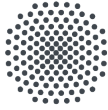


Theory of Leaky Mode Propagation in Optical Waveguide Geometries

Izzatjon Allayarov



University of Stuttgart
2020



University of Stuttgart
Germany

THEORY OF LEAKY MODE PROPAGATION IN OPTICAL WAVEGUIDE GEOMETRIES

Von der Fakultät Mathematik und Physik
der Universität Stuttgart zur Erlangung der Würde
eines Doktors der Naturwissenschaften (Dr. rer. nat.)
genehmigte Abhandlung

vorgelegt von

Izzatjon Mukhiddinovich Allayarov

aus Gurlan, Usbekistan

Hauptberichter:	Jun.-Prof. Dr. Thomas Weiss
Mitberichter:	Prof. Dr. Günter Wunner
Vorsitzende:	Prof. Dr. Stefanie Barz
Tag der Einreichung:	05.06.2020
Tag der mündlichen Prüfung:	17.07.2020

4. Physikalisches Institut der Universität Stuttgart
June 2020

Izzatjon Allayarov: *Theory of Leaky Mode Propagation in Optical Waveguide Geometries*, 2020

DECLARATION

I hereby certify that this dissertation is entirely my own work except where otherwise indicated. Passages and ideas from other sources have been clearly indicated.

Stuttgart, June 2020
Izzatjon Allayarov

In memory of my brother
Maqsadjon Mukhiddinovich Aminov
(1990–2009)

SCIENTIFIC CONTRIBUTIONS

ARTICLES IN PEER-REVIEWED SCIENTIFIC JOURNALS

Articles within the scope of this thesis:

- [A1] S. Upendar, **I. Allayarov**, M. A. Schmidt, and T. Weiss: *Analytical mode normalization and resonant state expansion for bound and leaky modes in optical fibers—an efficient tool to model transverse disorder*, Opt. Express **26**, 22536–22546 (2018). DOI 10.1364/oe.26.022536, cit. on pp. 4, 7, 16, 24–25, 27, 40, 42, 91.
- [A2] **I. Allayarov**, S. Upendar, M. A. Schmidt, and T. Weiss: *Analytic mode normalization for the Kerr nonlinearity parameter: Prediction of nonlinear gain for leaky modes*, Phys. Rev. Lett. **121**, 213905 (2018). DOI 10.1103/physrevlett.121.213905, cit. on pp. 4, 16, 35, 42, 49–51, 62, 67–68.
- [A3] **I. Allayarov**, M. A. Schmidt, and T. Weiss: *Theory of four-wave mixing for bound and leaky modes*, Phys. Rev. A **101**, 043806 (2020). DOI 10.1103/physreva.101.043806, cit. on pp. 4, 42, 57.

Other articles beyond the scope of this thesis:

- [O1] **I. Allayarov** and E. N. Tsoy: *Dynamics of fronts in optical media with linear gain and nonlinear losses*, Phys. Lett. A **377**, 550–554 (2013). DOI 10.1016/j.physleta.2012.12.029, cit. on p. 68.
- [O2] E. N. Tsoy, **I. Allayarov**, and F. K. Abdullaev: *Stable localized modes in asymmetric waveguides with gain and loss*, Opt. Lett. **39**, 4215–4218 (2014). DOI 10.1364/ol.39.004215.
- [O3] **I. Allayarov** and E. N. Tsoy: *Dynamics of Airy beams in nonlinear media*, Phys. Rev. A **90**, 023852 (2014). DOI 10.1103/physreva.90.023852.

Contributed talks (presenting author):

- [T1] **I. Allayarov**, M. Schäferling, M. L. Nesterov, and T. Weiss: *Efficiency analysis of a finite-difference modal method for the derivation of electromagnetic fields*, DPG Frühjahrstagung der Sektion Kondensierte Materie (SKM), Regensburg (Germany), 2016.
- [T2] **I. Allayarov**, M. Schäferling, and T. Weiss: *Efficient calculation of electromagnetic fields in the finite-difference modal method with adaptive coordinates*, Matheon-Workshop: 10th Annual Meeting Photonic Devices, Berlin (Germany), 2017.
- [T3] **I. Allayarov**, M. Schäferling, M. L. Nesterov, and T. Weiss: *Adaptive spatial resolution in the finite-difference modal method for the derivation of electromagnetic fields*, DPG Frühjahrstagung der Sektion Kondensierte Materie (SKM), Dresden (Germany), 2017.
- [T4] **I. Allayarov**, S. Upendar, M. A. Schmidt, and T. Weiss: *A new definition for the Kerr nonlinearity parameter*, DPG Frühjahrstagung der Sektion Atome, Moleküle, Quantenoptik und Plasmen (SAMOP), Erlangen (Germany), 2018.
- [T5] **I. Allayarov**, S. Upendar, M. A. Schmidt, and T. Weiss: *A new definition for the Kerr nonlinearity parameter*, XXVI International Workshop on Optical Wave and Waveguide Theory and Numerical Modelling (OWTNM), Bad Sassendorf (Germany), 2018.
- [T6] **I. Allayarov**, S. Upendar, M. A. Schmidt, and T. Weiss: *The impact of a new approach for the Kerr nonlinearity parameter on four-wave mixing*, DPG Frühjahrstagung der Sektion Atome, Moleküle, Quantenoptik und Plasmen (SAMOP), Rostock (Germany), 2019.
- [T7] **I. Allayarov**, S. Upendar, M. A. Schmidt, and T. Weiss: *A New Theoretical Formulation for the Nonlinear Pulse Propagation in Waveguide Geometries*, OSA Nonlinear Optics (NLO), Hawaii (USA), 2019.

Contributions as co-author:

- [C1] S. Upendar, **I. Allayarov**, G. Li, M. A. Schmidt, and T. Weiss: *Resonant State Expansion in Fiber Geometries*, CLEO Pacific Rim Conference, Hong Kong SAR (China), 2018.
- [C2] S. Upendar, **I. Allayarov**, M. A. Schmidt, and T. Weiss: *Resonant state expansion for disordered claddings in photonic crystal fibers*, DPG Frühjahrstagung der Sektion Kondensierte Materie (SKM), Berlin (Germany), 2018.
- [C3] S. Upendar, **I. Allayarov**, M. A. Schmidt, and T. Weiss: *Resonant state expansion for exterior perturbations in photonic crystal fibers*, DPG Frühjahrstagung der Sektion Atome, Moleküle, Quantenoptik und Plasmen (SAMOP), Rostock (Germany), 2019.
- [C4] S. Upendar, **I. Allayarov**, M. A. Schmidt, and T. Weiss: *Resonant State Expansion in Fiber Geometries*, International School and Conference on Disorder in Materials Science (DisoMAT), Potsdam (Germany), 2019.

CONTENTS

1	INTRODUCTION	1
2	RESONANT STATES OF WAVEGUIDE GEOMETRIES	7
2.1	Maxwell's equations and resonant states	7
2.1.1	Maxwell's equations in time domain	8
2.1.2	Maxwell's equations in frequency domain	9
2.1.3	Propagation equation	10
2.2	Expansion of the Green's dyadic	13
2.2.1	Green's dyadic in reciprocal space	13
2.2.2	Green's dyadic in real space	16
2.3	Poles on the complex frequency plane	18
2.4	Analytic mode normalization	20
2.4.1	Conventional normalization schemes	20
2.4.2	Analytical normalization scheme	24
2.4.3	Example: Step-profile fiber	27
3	MASTER EQUATION FOR PULSE PROPAGATION	35
3.1	Derivation of general master equation	35
3.2	Nonlinear Schroedinger equation	37
3.3	The Kerr nonlinearity parameter	40
3.4	Nonlinear gain and loss	49
3.5	The nonlinear gain and pulse propagation	52
4	GENERALIZED THEORY OF FOUR-WAVE MIXING	57
4.1	Bound-mode theory	58
4.2	General coupled amplitude equations	62
4.3	Modulation instability in hollow-core fibers	68
4.4	Optical system and simulation details	71
4.4.1	The optical system parameters	72
4.4.2	Nonlinearity parameters	75
4.4.3	Simulation details	75
4.5	Results and discussion	80
4.5.1	Quasicontinuous-wave regime	80
4.5.2	Ultrafast regime	82

5	DIPOLE EMISSION IN HOLLOW-CORE FIBERS	87
5.1	Dipole fields in fibers	88
5.1.1	Dipole fields from the Green's dyadic	89
5.1.2	Dipole fields from the reciprocity principle	90
5.2	Purcell factor	92
5.3	Dipole emission in hollow-core fibers	93
6	CONCLUSION AND OUTLOOK	101
	BIBLIOGRAPHY	105

ABSTRACT

Optical waveguides can support bound or leaky modes, depending on their geometrical and optical parameters. These modes are electromagnetic waves that propagate along the waveguide with a distinct transverse intensity profile and a propagation constant. Since bound modes exhibit an exponentially decaying transverse intensity profile, their propagation can easily be described within the standard theories. However, in leaky modes, the energy transversely radiates away from the waveguide, which results in to an exponentially growing transverse intensity profile. This makes the application of the standard theoretical formulations for the description of leaky modes questionable.

This thesis is dedicated to present a new theory of leaky modes propagation in optical waveguide geometries. The theory is based on a powerful and rigorous method for open systems in electrodynamics, namely the resonant-state expansion, together with an analytic mode normalization. The general master equation of the theory allows a rigorous description of both bound and leaky modes in waveguide geometries within a single theoretical framework.

We apply our theory to the nonlinear pulse propagation in a widely used types of waveguides in modern nonlinear optics, namely hollow-core fibers, that are dominated by leaky modes. At the beginning, we show that in the single-mode approximation, the master equation transforms into the well-known nonlinear Schroedinger equation with a new and general definition for the Kerr nonlinearity parameter. We find that for leaky modes the Kerr nonlinearity parameter can be a complex quantity with a negative imaginary part providing the nonlinear gain for the overall attenuating pulses. This nonlinear gain results in a stronger spectral broadening, which is demonstrated here on the example of a liquid-filled capillary-type fibers.

Next, we extend our theory for parametric processes such as four-wave mixing, which implies coupling between different modes and wavelengths. In this case, our theory predicts a more efficient generation of the so-called Stokes and anti-Stokes side-bands with an earlier onset than expected from the previous theory for bound modes. These effects are demonstrated numerically for a gas-filled hollow-core annulus fiber that supports leaky modes. Moreover, we demonstrate that

leaky modes yield modulation instability in hollow-core fibers, not only in the anomalous but also in the normal dispersion regime. The modulation instability can occur for all frequencies, which is a fundamental difference to bound modes.

In addition, we investigate the change of the emission of a dipole coupled to an optical fiber since such systems have important applications in quantum light sources and sensors. In this case, our theory can be straightforwardly applied to derive the electromagnetic fields that are generated by the dipole in complex waveguide geometries, including different types of hollow-core fibers.

ZUSAMMENFASSUNG

Optische Wellenleiter können gebundene Moden oder Leckmoden unterstützen, abhängig von ihren geometrischen und optischen Kenngrößen. Diese Moden stellen elektromagnetische Wellen mit einem genau umschriebenen transversalen Profil und einer Ausbreitungskonstante dar, die entlang des Wellenleiters propagieren. Da gebundene Moden in transversaler Richtung über ein exponentiell abklingendes Intensitätsprofil verfügen, kann ihre Ausbreitung auf einfache Art und Weise im Rahmen der herkömmlichen Theorien beschrieben werden. In Leckmoden tritt jedoch in transversaler Richtung Energie aus dem Wellenleiter aus, was ein exponentiell anwachsendes transversales Intensitätsprofil zur Folge hat. Dies macht die Anwendung der herkömmlichen theoretischen Formulierungen für die Beschreibung von Leckmoden problematisch.

Die vorliegende Arbeit hat sich zum Ziel gesetzt, eine neue Theorie zur Ausbreitung von Leckmoden in optischen Wellenleitern vorzustellen. Die Theorie basiert auf einer leistungsstarken und konsequenten Beschreibungsmethode für offene Systeme in der Elektrodynamik, und zwar der Resonanzzustandsentwicklung, zusammen mit einer analytischen Modennormierung. Die allgemeine Mastergleichung der Theorie erlaubt eine konsequente Beschreibung sowohl von gebundenen Moden als auch von Leckmoden in Wellenleitergeometrien in einem einheitlichen theoretischen Rahmen.

Wir wenden unsere Theorie auf die nichtlineare Pulsausbreitung in einem in der modernen nichtlinearen Optik vielgenutzten Typ von Wellenleitern an, und zwar den Hohlkernfasern, welche dominiert werden von Leckmoden. Anfangs zeigen wir, dass sich die Mastergleichung unter der Einzelmodennäherung in die wohlbekanntere nichtlineare Schrödingergleichung überführen lässt mit einer neuen und allgemeinen Definition des Kerr-Nichtlinearitätsparameters. Für Leckmoden finden wir heraus, dass der Kerr-Nichtlinearitätsparameters eine komplexwertige Größe sein kann, die über einen negativen Imaginärteil verfügt, welcher eine nichtlineare Verstärkung für die insgesamt gedämpften Pulse bereitstellt. Diese nichtlineare Verstärkung hat eine verstärkte spektrale Verbreiterung zur Folge, was hier am Beispiel einer flüssigkeitsgefüllten Kapillarfaser gezeigt wird.

Als nächstes erweitern wir unsere Theorie um parametrische Prozesse wie Vier-Wellen-Mischung, die eine Kopplung zwischen verschiedenen Moden und Wellenlängen beinhaltet. In diesem Fall sagt unsere Theorie eine effizientere Erzeugung und ein früheres Einsetzen der sogenannten Stokes und Anti-Stokes Seitenbänder voraus als es nach der herkömmlichen Theorie über gebundene Moden zu erwarten wäre. Diese Effekte werden numerisch für eine gasgefüllte Hohlkernringfaser gezeigt, welche Leckmoden unterstützt. Des Weiteren zeigen wir, dass Leckmoden Modulationsinstabilität in Hohlkernfasern erzeugen, nicht nur im Bereich der anomalen Dispersion, sondern auch im Bereich der normalen Dispersion. Die Modulationsinstabilität kann bei allen Frequenzen auftreten, was einen grundlegenden Unterschied zu gebundenen Moden darstellt.

Zusätzlich untersuchen wir die Änderung der Emission eines Dipols, der an eine optische Faser koppelt, da solche Systeme bedeutende Anwendungen für Quantenlichtquellen und Sensoren haben. In diesem Fall kann unsere Theorie auf einfache Art und Weise dazu verwendet werden, die Felder des Dipols in komplexen Wellenleitergeometrien einschließlich verschiedener Arten von Hohlkernfasern herzuleiten.

INTRODUCTION

Nowadays, optical waveguides are a key elements of many modern devices and systems which are used in different fields. The prime example are communication systems based on optical fibers, which outperform traditional electrical cabling systems in terms of their compactness and high information rate. Apart from that, optical fibers have other important applications in sensing, optical imaging, medicine, power transmission, etc.

In most of these applications, common or relatively weak light sources are used. Therefore, the response of a waveguide medium to the light field is practically linear. However, propagation of a high power laser beams or pulses in such waveguides leads to a nonlinear interaction between the light and the medium. In this case, one can observe various interesting nonlinear effects and objects such as self-focusing and optical solitons [5, 6]. The origin of these effects is the nonlinear refraction, i.e., the power dependence of the refractive index, which is in turn known as the Kerr effect [5, 7–10]:

$$n = n_0 + n_2 P, \quad (1.1)$$

where n_0 and n_2 are the linear and the nonlinear refractive indices, respectively, and $P \propto |A|^2$ is the power, which is proportional to the field amplitude A .

In the simplest case, the dynamics of the optical wave is described by the well-known nonlinear Schroedinger equation [5, 6, 10]:

$$\frac{\partial A}{\partial z} = -i \frac{\tilde{\beta}^{(2)}}{2} \frac{\partial^2 A}{\partial t^2} + i\gamma |A|^2 A, \quad (1.2)$$

where $\tilde{\beta}^{(2)}$ is the second-order dispersion coefficient, γ is the Kerr nonlinearity parameter that inversely proportional to the optical confinement (i.e., mode area [5]). Note that in the one-dimensional case, Eq. (1.2) is an exactly integrable model, which has been shown within inverse scattering method [11, 12]. The solutions of this equation corre-

spond to the well-known solitons [5]. The fundamental soliton has the following general form [5, 10, 13]:

$$A(z, t) = A_o \operatorname{sech}\left(\frac{t + \nu z - t_s}{t_o}\right) e^{ik_s z - i\omega_s t + i\phi_s}, \quad (1.3)$$

where $t_o = T_o/\eta$ and $\omega_s = \delta/T_o$ are the width and the frequency, respectively, of the soliton with the initial phase ϕ_s located at the position t_s . Here, δ and η are the real and the imaginary parts of the eigenvalue of the so-called Zakharov-Shabat scattering problem [11]. The fundamental soliton's amplitude A_o , velocity ν , and wave number k_s are given by

$$A_o = \eta \left(\frac{|\tilde{\beta}^{(2)}|}{\gamma T_o^2} \right)^{1/2}, \quad \nu = \delta \frac{|\tilde{\beta}^{(2)}|}{T_o^2}, \quad k_s = (\eta^2 - \delta^2) \frac{|\tilde{\beta}^{(2)}|}{2T_o^2}.$$

In these equations, $\tilde{\beta}^{(2)}$ and γ are assumed to be a negative and a real number, respectively, and T_o is the characteristic time defined by the initial condition. Thus, all soliton parameters are defined by the real δ and the imaginary η parts of the eigenvalue of the scattering problem and the waveguide's linear and nonlinear characteristics. Another interesting point here is that the width and the amplitude of the soliton is inversely proportional to each other.

As one can see, within the nonlinear Schroedinger model, the linear and the nonlinear effects are characterized by a single $\tilde{\beta}^{(2)}$ and a γ parameter, respectively. Accordingly, consistency between simulation results based on this model and the experimental measurements partially depends on if these parameters are accurately calculated. The linear properties of optical waveguides can be measured or calculated since there are a lot of experimental and numerical methods that provide accurate results. For conventional step-profile fibers, for which the guiding mechanism of light is total internal reflection and hence modes are truly guided (bounded) [5, 14–16], the nonlinearity parameter γ can also be evaluated within the conventional and well-known approaches.

However, there are modern and advanced type of waveguides with complex transverse geometry, namely hollow-core waveguides [5, 17]. For instance, a conventional step-profile fiber with inverted core and cladding refractive indices can also be considered as simple hollow-core fiber with step-profile refractive index. The scanning electron microscope images of different hollow-core waveguides are shown in Fig. 1.1.

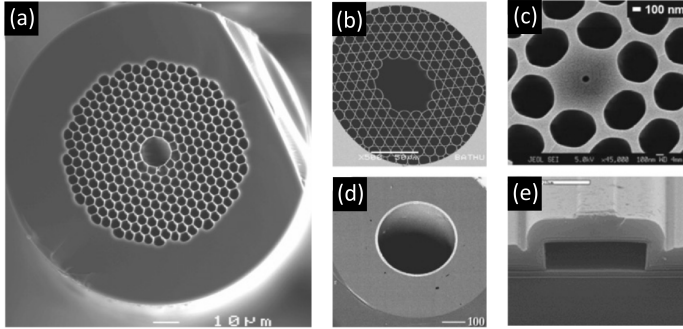


Figure 1.1. Scanning electron microscope images of different types of hollow-core waveguides: (a) Hollow-core photonic crystal fiber, (b) Kagomé fiber, (c) nano-scaled hollow-core fiber, (d) Bragg-grating fiber, (e) rectangular hollow-core antiresonant reflecting optical waveguide. [Image adapted with permission from Ref. [17]. Copyright Taylor and Francis Group.]

Nowadays, hollow-core photonic crystal fibers represent a novel class of fibers that are widely used in the context of nonlinear photonics. They offer a plethora of additional degrees of freedom to control the optical properties compared to conventional fibers. For instance, the linear dispersion properties of gas-filled hollow-core fibers can be controlled through changing the gas temperature and the pressure, in addition to modifying its geometrical parameters, which in fact allows to achieve octave spanning supercontinua [see Fig. 1.2 (a)] [17, 18]. Moreover, gas filled hollow-core photonic crystal fibers can substantially enhance another important process, namely four-wave mixing [see Fig. 1.2 (b)] [19]. On the other hand, geometric resonances of hollow-core fibers can be used for light generation [20]. Furthermore, using gases as a nonlinear medium allows for applying high-power laser sources without damaging the waveguide [21, 22]. Additionally, nonlinear effects in such fibers can be enhanced by using different nonlinear liquids [23–26].

The standard formulations for the nonlinear pulse propagation in step-profile fibers with bound modes are not capable of treating the pulse propagation in hollow-core fibers accurately. The reason is the following: As it is mentioned above, the conventional step-profile fibers carry bound core modes with an exponential decay of the electromagnetic fields in the homogeneous surrounding due to the total internal

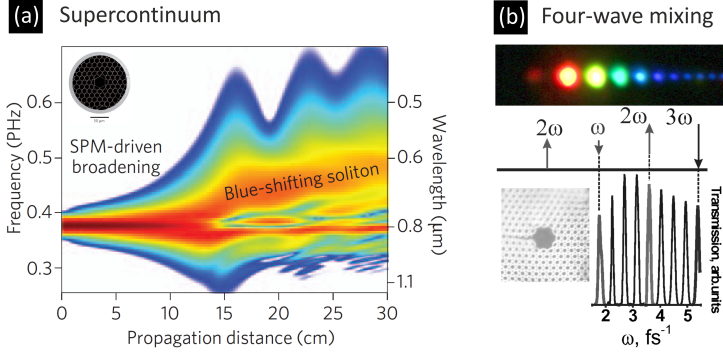


Figure 1.2. Nonlinear pulse propagation in hollow-core fibers: (a) Supercontinuum generation in a Kagomé photonic crystal fiber filled by argon. [Image adapted with permission from Ref. [18]. Copyright Macmillan Publishers Limited.] (b) four-wave mixing in hollow-core fiber with air holes. [Image adapted with permission from Refs. [19, 27]. Copyright The Optical Society.]

reflection. However, the total internal reflection is broken in case of hollow-core fibers. Therefore, hollow-core fibers are dominated by another class of modes, namely leaky modes [28]. Such modes lose energy due to the radiation perpendicular to the direction of propagation, which corresponds to having an imaginary part of the corresponding propagation constant. As a direct consequence, the electromagnetic fields of leaky modes diverge with distance from the fiber center [A1–A3]. Hence, the nonlinearity parameter γ of leaky modes vanishes in the framework of conventional approaches. Thus, the system would exhibit no Kerr nonlinearity at all, which is unphysical.

Essentially, the main problem with leaky modes is the normalization. In optical waveguides, the total electromagnetic field can be described as a sum of the fields of different modes. Within such schemes, all modes must be normalized and satisfy a certain orthogonality condition. Bound modes of step-profile fiber usually are normalized by an integral of the absolute square value of the electric fields or the axial component of the time-averaged Poynting vector over the entire cross section of the fiber. However, these normalizations are not applicable in the case of leaky modes, since they grow in transverse direction. Several approaches have been suggested to bypass this issue, such as using

a restricted area of normalization defined by radiation caustic [28] and applying a complex coordinate transformation to regions outside the spatial inhomogeneities [29, 30] for suppressing the divergence (equivalent to perfectly matched layers [31]). Nevertheless, in most cases these approaches are prone to failure or are not effective, since they include several free parameters that need to be adapted to a specific geometry.

Here, one should mention that, there are an iterative approaches for the nonlinearity parameter that do not require any normalization and can be applied for both bound and leaky modes [32, 33]. However, iterative methods purely rely on numerical calculations and hence can be quite time consuming.

Thus, an accurate description of the nonlinear propagation of leaky modes is not straightforward in contrast to bound modes. It has challenging problems concerning the mode normalization and characterization of the nonlinear properties. In this dissertation, we present solutions to these challenges by a thorough study of leaky modes within our new theory for nonlinear pulse propagation in waveguide geometries.

The dissertation is structured as follows: In Chapter 2, we start by presenting the foundations of the resonant-state expansion, which is the base of our new theory for the pulse propagation. After giving a definition of resonant states/modes, we discuss the expansion of the Green's dyadic in the basis of resonant states and derive orthogonality and normalization conditions of these states from the reciprocity theorem.

In Chapter 3, we derive a general master equation for the nonlinear pulse propagation in waveguides. After this, we consider a single-mode limit of the master equation that simplifies into the standard nonlinear Schroedinger equation with a closed expression for the Kerr nonlinearity parameter. In addition, we investigate the spectral broadening of an initial pulse, i.e., supercontinuum generation within this model by carrying out numerical simulations.

Chapter 4 focuses on a generalized theory of four-wave mixing. After a detailed derivation of new coupled equations for four-wave mixing from the master equation, at first, we review modulation instability of the steady-state within the generalized theory. In the following section, we apply our theory to a gas-filled annulus fiber and demonstrate numerically that our theory predicts a more efficient power conversion between waves in comparison with the conventional theory.

Single photon emitters coupled to optical fibers have important applications in quantum light sources and sensors. Therefore, in the last

Chapter 5, we consider the linear propagation of leaky modes excited by a point current source. At first, we derive the total electromagnetic field of an oscillating dipole by using the Green's dyadic and the reciprocity principle. After this, we investigate the change of the spontaneous emission rate of a dipole in hollow-core fibers.

Finally, Chapter 6, concludes the main results of all studies presented and provides a short outlook about the possible improvements and the future development of the presented theory.

~

RESONANT STATES OF WAVEGUIDE GEOMETRIES

This chapter is partially based on the following publication [A1]:

S. Upendar, **I. Allayarov**, M. A. Schmidt, and T. Weiss: "*Analytical mode normalization and resonant state expansion for bound and leaky modes in optical fibers – an efficient tool to model transverse disorder*", *Opt. Express*, **26** 22536–22546 (2018).
DOI 10.1364/oe.26.022536

This chapter provides a brief introduction to the fundamental equations of the light field propagation in optical waveguides. Therefore, at the beginning, we consider Maxwell's equations in the absence of sources and define the eigensolutions/modes of the system as a resonant states. Next, we show that the Greens's dyadic, i.e., the solution of Maxwell's equations for a point current source, can be represented as a sum over the resonant states. Since eigensolutions of a source-free system are defined up to arbitrary factor, first of all, we discuss conventional ways of normalization. After this, we derive our analytical normalization scheme as well as the orthogonality condition for resonant states. In addition, at the end of the chapter, we give an exact form of this normalization scheme for a simple step-profile fiber geometry and use it to normalize the fundamental bound and leaky modes of the fiber.

2.1 MAXWELL'S EQUATIONS AND RESONANT STATES

The following subsections briefly introduce Maxwell's equations in time and frequency domains, and the constitutive relations with the approach in which the induced polarization is split into the linear and nonlinear parts. Next, taking into account translational symmetry of the equations, we obtain the propagation equation and define resonant states of waveguide geometries.

2.1.1 Maxwell's equations in time domain

The propagation of optical fields in waveguides is described by the macroscopic Maxwell's equations. In the Gaussian unit system, these equations have the form [34]

$$\nabla \times \mathbf{E}(\mathbf{r}; t) = -\frac{1}{c} \frac{\partial \mathbf{B}(\mathbf{r}; t)}{\partial t}, \quad (2.1a)$$

$$\nabla \times \mathbf{H}(\mathbf{r}; t) = \frac{1}{c} \frac{\partial \mathbf{D}(\mathbf{r}; t)}{\partial t} + \frac{4\pi}{c} \mathbf{j}(\mathbf{r}; t), \quad (2.1b)$$

$$\nabla \cdot \mathbf{D}(\mathbf{r}; t) = 4\pi[\rho_f(\mathbf{r}; t) + \rho_b(\mathbf{r}; t)], \quad (2.1c)$$

$$\nabla \cdot \mathbf{B}(\mathbf{r}; t) = 0. \quad (2.1d)$$

Here, \mathbf{E} and \mathbf{H} are electric and magnetic field vectors, respectively, and \mathbf{D} and \mathbf{B} denote the corresponding electric displacement (induction) and magnetic induction. The sources of the electromagnetic field are represented by the current density \mathbf{j} and the free ρ_f and bound ρ_b contributions of charge density.

The electric and magnetic inductions \mathbf{D} and \mathbf{B} are related with the electric and magnetic fields \mathbf{E} and \mathbf{H} through the following constitutive relations [34]:

$$\mathbf{D}(\mathbf{r}; t) = \mathbf{E}(\mathbf{r}; t) + 4\pi\mathbf{P}(\mathbf{r}; t), \quad (2.2a)$$

$$\mathbf{B}(\mathbf{r}; t) = \mathbf{H}(\mathbf{r}; t) + 4\pi\mathbf{M}(\mathbf{r}; t), \quad (2.2b)$$

where \mathbf{P} and \mathbf{M} are the polarization and the magnetization vectors, respectively.

The most of optical waveguides are made of nonmagnetic materials. Furthermore, at optical frequencies, the magnetization \mathbf{M} can be neglected, i.e., $\mathbf{M} \approx 0$. However, in order to keep our formulation as general as possible, we assume that the magnetization \mathbf{M} and the magnetic field \mathbf{H} are linearly connected as $\mathbf{M} = \chi_m^{(1)} \mathbf{H}$ via the first-order magnetic susceptibility constant $\chi_m^{(1)}$. In contrast, the polarization \mathbf{P} is split into the linear $\mathbf{P}_L = \chi_e^{(1)} \mathbf{E}$ with the first-order electric susceptibility constant

$\chi_e^{(1)}$ and the nonlinear \mathbf{P}_L parts. Thus, the constitutive relations can be written in the form

$$\mathbf{D}(\mathbf{r}; t) = \varepsilon(\mathbf{r})\mathbf{E}(\mathbf{r}; t) + 4\pi\mathbf{P}_{NL}(\mathbf{r}; t), \quad (2.3a)$$

$$\mathbf{B}(\mathbf{r}; t) = \mu(\mathbf{r})\mathbf{H}(\mathbf{r}; t), \quad (2.3b)$$

where $\varepsilon = 1 + 4\pi\chi_e^{(1)}$ is the permittivity and $\mu = 1 + 4\pi\chi_m^{(1)}$ is the permeability. Additionally, for the sake of completeness, we keep the tensorial form of ε and μ .

Using the constitutive relations, the curl part of Maxwell's equations are now given by

$$\nabla \times \mathbf{E}(\mathbf{r}; t) = -\frac{\mu(\mathbf{r})}{c} \frac{\partial \mathbf{H}(\mathbf{r}; t)}{\partial t}, \quad (2.4a)$$

$$\begin{aligned} \nabla \times \mathbf{H}(\mathbf{r}; t) &= \frac{\varepsilon(\mathbf{r})}{c} \frac{\partial \mathbf{E}(\mathbf{r}; t)}{\partial t} + \\ &\frac{4\pi}{c} \left[\mathbf{j}(\mathbf{r}; t) + \frac{\partial \mathbf{P}_{NL}(\mathbf{r}; t)}{\partial t} \right]. \end{aligned} \quad (2.4b)$$

2.1.2 Maxwell's equations in frequency domain

When dealing with waveguide geometries, it is often convenient to work in frequency domain rather than in time domain. Therefore, first of all, let us introduce the following direct Fourier transform

$$f(\mathbf{r}; \omega) = \int_{-\infty}^{+\infty} f(\mathbf{r}; t) e^{i\omega t} dt, \quad (2.5)$$

and convolution

$$f \star g = \frac{1}{2\pi} \int_{-\infty}^{+\infty} f(\omega - \omega') g(\omega) d\omega'. \quad (2.6)$$

The corresponding inverse transformations are

$$f(\mathbf{r}; t) = \frac{1}{2\pi} \int_{-\infty}^{+\infty} f(\mathbf{r}; \omega) e^{-i\omega t} d\omega, \quad (2.7)$$

and

$$f * g = \int_{-\infty}^{+\infty} f(t-t')g(t)dt', \quad (2.8)$$

respectively.

Thus, the frequency-domain representation of the curl Maxwell's equations can be written as

$$\nabla \times \mathbf{E}(\mathbf{r}; \omega) = ik_0 \mu(\mathbf{r}; \omega) \mathbf{H}(\mathbf{r}; \omega), \quad (2.9a)$$

$$\nabla \times \mathbf{H}(\mathbf{r}; \omega) = -ik_0 \varepsilon(\mathbf{r}; \omega) \mathbf{E}(\mathbf{r}; \omega) + \frac{4\pi}{c} \left[\mathbf{j}(\mathbf{r}; \omega) - i\omega \mathbf{P}_{\text{NL}}(\mathbf{r}; \omega) \right], \quad (2.9b)$$

where $k_0 = \omega/c$ is the free space wave number. For the sake of simplicity, we denote the fields with the same letters as in the case of time domain. Whenever it is necessary to distinguish both, we will write the time or frequency dependence explicitly.

After some algebra, Eqs. (2.9a) and (2.9b) can be cast into a compact operator form [35]:

$$\underbrace{\begin{bmatrix} \varepsilon(\mathbf{r}; \omega)k_0 & -\nabla \times \\ -\nabla \times & \mu(\mathbf{r}; \omega)k_0 \end{bmatrix}}_{\equiv \mathbb{M}(\mathbf{r}; \omega)} \underbrace{\begin{bmatrix} \mathbf{E}(\mathbf{r}; \omega) \\ i\mathbf{H}(\mathbf{r}; \omega) \end{bmatrix}}_{\equiv \mathbf{F}(\mathbf{r}; \omega)} = \underbrace{\begin{bmatrix} \mathbf{J}_{\mathbf{E}}(\mathbf{r}; \omega) \\ i\mathbf{J}_{\mathbf{H}}(\mathbf{r}; \omega) \end{bmatrix}}_{\equiv \mathbf{J}(\mathbf{r}; \omega)}, \quad (2.10)$$

where $\mathbf{J}_{\mathbf{E}} = -4\pi i/c(\mathbf{j} - i\omega \mathbf{P}_{\text{NL}})$ is the general electric current source, and the magnetic current $\mathbf{J}_{\mathbf{H}} \equiv \mathbf{o}$ is introduced artificially for symmetry purposes.

2.1.3 Propagation equation

In waveguide geometries, the permittivity and the permeability tensors ε and μ , respectively, possess a translational symmetry in one spatial direction, which we choose to be the z direction. Hence, it is convenient to Fourier transform Maxwell's equations along this direction using

$$\hat{f}(\mathbf{r}_{\parallel}, \beta; \omega) = \frac{1}{2\pi} \int_{-\infty}^{+\infty} f(\mathbf{r}_{\parallel}, z; \omega) e^{-i\beta z} dz, \quad (2.11)$$

where \mathbf{r}_{\parallel} denotes the spatial coordinates in the transverse xy plane, and the hat implies that we are in Fourier space or simply in reciprocal β space. In order to transform back to real z space, we use

$$\hat{f}(\mathbf{r}_{\parallel}, z; \omega) = \int_{-\infty}^{+\infty} f(\mathbf{r}_{\parallel}, \beta; \omega) e^{i\beta z} d\beta. \quad (2.12)$$

Note that hereinafter, we usually omit the limits $(-\infty, +\infty)$ of the integral in any Fourier transformation.

Thus, applying Eq. (2.11) to Eqs. (2.9a) and (2.9b), we obtain the propagation equation:

$$\underbrace{\begin{bmatrix} \varepsilon(\mathbf{r}_{\parallel}; \omega) k_0 & -\hat{\nabla}_{\beta} \times \\ -\hat{\nabla}_{\beta} \times & \mu(\mathbf{r}_{\parallel}; \omega) k_0 \end{bmatrix}}_{\equiv \hat{\mathbb{M}}(\mathbf{r}_{\parallel}, \beta; \omega)} \underbrace{\begin{bmatrix} \hat{\mathbf{E}}(\mathbf{r}_{\parallel}, \beta; \omega) \\ i\hat{\mathbf{H}}(\mathbf{r}_{\parallel}, \beta; \omega) \end{bmatrix}}_{\equiv \hat{\mathbf{F}}(\mathbf{r}_{\parallel}, \beta; \omega)} = \underbrace{\begin{bmatrix} \hat{\mathbf{J}}_{\mathbf{E}}(\mathbf{r}_{\parallel}, \beta; \omega) \\ i\hat{\mathbf{J}}_{\mathbf{H}}(\mathbf{r}_{\parallel}, \beta; \omega) \end{bmatrix}}_{\equiv \hat{\mathbf{J}}(\mathbf{r}_{\parallel}, \beta; \omega)}. \quad (2.13)$$

Here, $\hat{\nabla}_{\beta} \equiv [\partial/\partial x, \partial/\partial y, i\beta]^T$ and T denotes the transpose operation. For the sake of brevity, hereinafter we omit the ω dependence in the equations. However, when needed, the dependence on ω will be mentioned explicitly.

Solving Eq. (2.13) in the absence of sources, i.e., in case of $\hat{\mathbf{J}} = 0$, leads to the eigenvalue problem

$$\hat{\mathbb{M}}(\mathbf{r}_{\parallel}, \beta_m) \hat{\mathbf{F}}(\mathbf{r}_{\parallel}, \beta_m) = 0, \quad (2.14)$$

that gives eigenvalues β_m and eigenvectors $\hat{\mathbf{F}}_m = \hat{\mathbf{F}}(\mathbf{r}_{\parallel}, \beta_m)$ of the system, numbered by the index m . We restrict our considerations to solutions that satisfy outgoing boundary conditions (also known as the Sommerfeld's radiation condition [36]):

$$\hat{\mathbf{F}}_m(\mathbf{r}_{\parallel}) \rightarrow \frac{e^{i\kappa_m \rho}}{\rho^{1/2}} \quad \text{for } \rho \rightarrow \infty, \quad (2.15)$$

where $\rho = |\mathbf{r}_{\parallel}|$ is the radial distance and $\kappa_m = (\varepsilon \mu k_0^2 - \beta_m^2)^{1/2}$ is the in-plane component of the wavenumber.

We define these eigensolutions as resonant states of the system [35, 37–40]. In theory of optical waveguides the resonant states are usually called the waveguide modes. In this terminology, $\hat{\mathbf{F}}_m$ represents the mode fields with the propagation constant β_m . For a homogeneous

medium with refractive index n_{ho} , modes are either decaying exponentially [evanescent modes, $\text{Re}(\beta_m) = 0$, $\text{Im}(\beta_m) > 0$] or they are propagating outwards [radiating modes, $0 < \beta_m < n_{\text{ho}}k_0$]. If we consider a spatially modulated, i.e., structured region surrounded by homogeneous space (e.g., an optical fiber), the propagation constant β_m is in general a complex quantity. It can be real, if the refractive index of the spatially modulated region is higher than surrounding medium. In this case the total internal reflection takes place, the waveguide modes are bound, and mode fields decay exponentially in the surrounding region. For instance, conventional step-profile optical fiber with $n_{\text{cl}} < n_{\text{co}}$, where n_{co} and n_{cl} are the core and the cladding refractive indices, respectively, supports bound modes with the real propagation constant defined in the range $n_{\text{cl}}k_0 \leq \beta_m < n_{\text{co}}k_0$ [28, 41]. Otherwise, i.e., in the case of $n_{\text{cl}} > n_{\text{co}}$, the propagation constant satisfies $\text{Re}(\beta_m) > 0$, $\text{Im}(\beta_m) > 0$. Waveguide modes in this case are leaky and the outgoing boundary conditions require that the field distributions of leaky modes $\hat{\mathbf{F}}_m$ with radiation to the far field grow with distance to the structured region [28, 38].

Here, we note that due to the reciprocity theorem [42], for each eigenvector $\hat{\mathbf{F}}_m$ with eigenvalue β_m , there is another "reciprocal conjugate" eigenvector $\hat{\mathbf{F}}_m^{\text{R}} \equiv \hat{\mathbf{F}}_{-m}$ with eigenvalue $-\beta_m$. Here, R denotes the reciprocal conjugation. Under the transformation $\beta_m \rightarrow -\beta_m$, Eq. (2.14) must be invariant. Hence, there are two possibilities that fulfil this condition. Either

$$\begin{bmatrix} E_x \rightarrow +E_x \\ E_y \rightarrow +E_y \\ E_z \rightarrow -E_z \end{bmatrix}, \quad \begin{bmatrix} H_x \rightarrow -H_x \\ H_y \rightarrow -H_y \\ H_z \rightarrow +H_z \end{bmatrix}, \quad \text{for } \beta_m \rightarrow -\beta_m, \quad (2.16)$$

or

$$\begin{bmatrix} E_x \rightarrow -E_x \\ E_y \rightarrow -E_y \\ E_z \rightarrow +E_z \end{bmatrix}, \quad \begin{bmatrix} H_x \rightarrow +H_x \\ H_y \rightarrow +H_y \\ H_z \rightarrow -H_z \end{bmatrix}, \quad \text{for } \beta_m \rightarrow -\beta_m. \quad (2.17)$$

In this thesis, we stick in the first convention. Note that for bound modes, the reciprocal conjugation is equivalent to the complex conjugation.

2.2 EXPANSION OF THE GREEN'S DYADIC

The Green's function approach is a powerful and widely used concept in electromagnetic field theory [43–45]. Therefore, in this section, we introduce the concept of the dyadic Green function and derive its explicit spectral representation based on the resonant states of the optical system. For the sake of completeness, we also define the Green's dyadic in the real space.

2.2.1 Green's dyadic in reciprocal space

The Green's dyadic is typically defined as a solution of Eq. (2.13) for a point source located at \mathbf{r}'_{\parallel} that satisfies the outgoing boundary condition Eq. (2.15):

$$\hat{\mathbb{M}}(\mathbf{r}_{\parallel}, \beta) \hat{\mathbf{G}}_{\beta}(\mathbf{r}_{\parallel}, \mathbf{r}'_{\parallel}) = \hat{\mathbb{I}} \delta(\mathbf{r}_{\parallel} - \mathbf{r}'_{\parallel}), \quad (2.18)$$

where $\hat{\mathbb{I}}$ is the 6×6 identity matrix. As shown in [35, 37–40, 46, 47], the Green's dyadic $\hat{\mathbf{G}}_{\beta}(\mathbf{r}_{\parallel}, \mathbf{r}'_{\parallel})$ can be expanded into the basis of resonant states. From a mathematical point of view, this follows from the Mittag-Leffler theorem [48]. In this context, resonant states denote a finite number of poles of the Green's dyadic in the complex β plane:

$$\hat{\mathbf{G}}_{\beta}(\mathbf{r}_{\parallel}, \mathbf{r}'_{\parallel}) = \sum_m \frac{\hat{R}_m(\mathbf{r}_{\parallel}, \mathbf{r}'_{\parallel})}{\beta - \beta_m} + \hat{\mathbf{G}}_{\beta}^{\text{cut}}. \quad (2.19)$$

Here, \hat{R}_m denotes the residue of $\hat{\mathbf{G}}_{\beta}$ around β_m . Sometimes in Eq. (2.19) along with the poles, we have to take into account the so-called cut contribution $\hat{\mathbf{G}}_{\beta}^{\text{cut}}$ of the Green's dyadic. The cut has to be considered if $\hat{\mathbf{G}}_{\beta}$ is a multi-valued function with an infinite number of Riemann sheets [38, 48, 49]. In this thesis, we neglect the cut contribution in the Green's dyadic, assuming that the poles are located far from the cut.

Now, let us find the exact form of the residue \hat{R}_m . For that, we proceed in the same manner as usually for the resonant state expansion, i.e., we assume a source term that vanishes at resonance [35, 37–39, 47]:

$$\hat{\mathbb{M}}(\mathbf{r}_{\parallel}, \beta) \hat{\mathbf{F}}(\mathbf{r}_{\parallel}, \beta) = \hat{\mathbf{J}}(\mathbf{r}_{\parallel}, \beta), \quad (2.20)$$

with

$$\hat{\mathbf{J}}(\mathbf{r}_{\parallel}, \beta) = \prod_m (\beta - \beta_m) \hat{\xi}_m(\mathbf{r}_{\parallel}), \quad (2.21)$$

where $\hat{\xi}_m$ is some arbitrary function. In this case, the right hand side of Eq. (2.20) vanishes at resonance, and it reduces to the eigenvalue problem Eq. (2.14). In principle, we can assume any functional dependence on the right hand side with the order of $O(\beta - \beta_m)$ for $\beta \rightarrow \beta_m$. Furthermore, $\hat{\xi}_m$ should be located in the regions of spatial inhomogeneities, i.e., not in the homogeneous surrounding. In addition, we have to be careful in the case of degenerate resonant states.

Thus, the solution of Eq. (2.20) can be written as

$$\hat{\mathbf{F}}(\mathbf{r}_{\parallel}, \beta) = \int \hat{\mathbf{G}}_{\beta}(\mathbf{r}_{\parallel}, \mathbf{r}'_{\parallel}) \hat{\mathbf{J}}(\mathbf{r}'_{\parallel}, \beta) d\mathbf{r}'_{\parallel}. \quad (2.22)$$

Considering this solution in the limit $\beta \rightarrow \beta_m$, we get:

$$\begin{aligned} \hat{\mathbf{F}}_m(\mathbf{r}_{\parallel}) &= \lim_{\beta \rightarrow \beta_m} \hat{\mathbf{F}}(\mathbf{r}_{\parallel}, \beta) = \\ &= \lim_{\beta \rightarrow \beta_m} \sum_{m'} \frac{\beta - \beta_m}{\beta - \beta_{m'}} \int \hat{\mathbf{R}}_{m'}(\mathbf{r}_{\parallel}, \mathbf{r}'_{\parallel}) \cdot \hat{\sigma}(\mathbf{r}'_{\parallel}, \beta) d\mathbf{r}'_{\parallel} = \\ &= \sum_{m'} \delta_{mm'} \int \hat{\mathbf{R}}_{m'}(\mathbf{r}_{\parallel}, \mathbf{r}'_{\parallel}) \cdot \hat{\sigma}_m(\mathbf{r}'_{\parallel}) d\mathbf{r}'_{\parallel} = \\ &= \int \hat{\mathbf{R}}_m(\mathbf{r}_{\parallel}, \mathbf{r}'_{\parallel}) \cdot \hat{\sigma}_m(\mathbf{r}'_{\parallel}) d\mathbf{r}'_{\parallel}, \end{aligned} \quad (2.23)$$

with

$$\hat{\sigma}(\mathbf{r}_{\parallel}, \beta) = \prod_{n \neq m} (\beta - \beta_n) \hat{\xi}_n(\mathbf{r}_{\parallel}), \quad (2.24)$$

and $\hat{\sigma}_m(\mathbf{r}_{\parallel}) \equiv \hat{\sigma}(\mathbf{r}_{\parallel}, \beta_m)$. Thus, taking into account the last expression, we can assume the following form of the residue:

$$\hat{\mathbf{R}}_m(\mathbf{r}_{\parallel}, \mathbf{r}'_{\parallel}) = -\frac{1}{2N_m} \hat{\mathbf{F}}_m(\mathbf{r}_{\parallel}) \otimes \hat{\mathbf{G}}_m(\mathbf{r}'_{\parallel}). \quad (2.25)$$

Here, $\hat{\mathbf{G}}_m$ is an unknown vector and \otimes denotes the outer product. By rewriting Eq. (2.23) as

$$\hat{\mathbf{F}}_m(\mathbf{r}_{\parallel}) = \hat{\mathbf{F}}_m(\mathbf{r}_{\parallel}) \left[-\frac{1}{2N_m} \int \hat{\mathbf{G}}_m(\mathbf{r}'_{\parallel}) \cdot \hat{\sigma}_m(\mathbf{r}'_{\parallel}) d\mathbf{r}'_{\parallel} \right], \quad (2.26)$$

we can see that our assumption should fulfil the condition

$$-\frac{1}{2N_m} \int \hat{\mathbf{G}}_m(\mathbf{r}_{\parallel}) \cdot \hat{\sigma}_m(\mathbf{r}_{\parallel}) d\mathbf{r}_{\parallel} = 1, \quad (2.27)$$

with N_m being the normalization constant of the resonant states that should be defined. The factor "-1/2" is introduced for the later convenience.

In the following, first of all, we derive the unknown vector $\hat{\mathbf{G}}_m$. For that we use reciprocity theorem. Let us consider two fields $\hat{\mathbf{F}}(\mathbf{r}_{\parallel}, \beta)$ and $\hat{\mathbf{F}}(\mathbf{r}_{\parallel}, -\beta)$ originating in a sources $\hat{\mathbf{J}}(\mathbf{r}_{\parallel}, \beta)$ and $\hat{\mathbf{J}}(\mathbf{r}_{\parallel}, -\beta)$, respectively, and write the corresponding propagation equations:

$$\hat{\mathbb{M}}(\mathbf{r}_{\parallel}, \beta) \hat{\mathbf{F}}(\mathbf{r}_{\parallel}, \beta) = \hat{\mathbf{J}}(\mathbf{r}_{\parallel}, \beta), \quad (2.28a)$$

$$\hat{\mathbb{M}}(\mathbf{r}_{\parallel}, -\beta) \hat{\mathbf{F}}(\mathbf{r}_{\parallel}, -\beta) = \hat{\mathbf{J}}(\mathbf{r}_{\parallel}, -\beta). \quad (2.28b)$$

Multiplying Eq. (2.28a) with $\hat{\mathbf{F}}(\mathbf{r}_{\parallel}, -\beta)$ and Eq. (2.28b) with $\hat{\mathbf{F}}(\mathbf{r}_{\parallel}, \beta)$ from the left hand side, respectively, and then subtracting the second expression from the first one, we obtain:

$$\begin{aligned} \hat{\mathbf{F}}(\mathbf{r}_{\parallel}, -\beta) \cdot \hat{\mathbb{M}}(\mathbf{r}_{\parallel}, \beta) \hat{\mathbf{F}}(\mathbf{r}_{\parallel}, \beta) - \hat{\mathbf{F}}(\mathbf{r}_{\parallel}, \beta) \cdot \hat{\mathbb{M}}(\mathbf{r}_{\parallel}, -\beta) \hat{\mathbf{F}}(\mathbf{r}_{\parallel}, -\beta) = \\ \hat{\mathbf{F}}(\mathbf{r}_{\parallel}, -\beta) \cdot \hat{\mathbf{J}}(\mathbf{r}_{\parallel}, \beta) - \hat{\mathbf{F}}(\mathbf{r}_{\parallel}, \beta) \cdot \hat{\mathbf{J}}(\mathbf{r}_{\parallel}, -\beta). \end{aligned} \quad (2.29)$$

Using the following vector identity for two arbitrary vectors \mathbf{A} and \mathbf{B}

$$\mathbf{B} \cdot \hat{\nabla}_{\beta} \times \mathbf{A} - \mathbf{A} \cdot \hat{\nabla}_{-\beta'} \times \mathbf{B} = \nabla_{\parallel} \cdot (\mathbf{A} \times \mathbf{B}) + i(\beta - \beta')(\mathbf{A} \times \mathbf{B})_z, \quad (2.30)$$

the left hand side (LHS) of Eq. (2.29) can be transformed for symmetric permittivity and permeability tensors ($\epsilon^T = \epsilon$ and $\mu^T = \mu$) into

$$\text{LHS} = \nabla_{\parallel} \cdot \left[\hat{\mathbf{E}}(\mathbf{r}_{\parallel}, \beta) \times \hat{\mathbf{H}}(\mathbf{r}_{\parallel}, -\beta) - \hat{\mathbf{E}}(\mathbf{r}_{\parallel}, -\beta) \times \hat{\mathbf{H}}(\mathbf{r}_{\parallel}, \beta) \right], \quad (2.31)$$

with in-plane gradient ∇_{\parallel} . The subscript z in Eq. (2.30) denotes the z component of the vector.

Integration over spatial inhomogeneities in the \mathbf{r}_{\parallel} plane, this term vanishes since $\hat{\mathbf{F}}(\mathbf{r}_{\parallel}, \beta)$ and $\hat{\mathbf{F}}(\mathbf{r}_{\parallel}, -\beta)$ have the same outgoing boundary conditions [see Eq. (2.15)]. Thus, integrating Eq. (2.29) over all spatial inhomogeneities provides the reciprocity theorem:

$$\int \left[\hat{\mathbf{F}}(\mathbf{r}_{\parallel}, -\beta) \cdot \hat{\mathbf{J}}(\mathbf{r}_{\parallel}, \beta) - \hat{\mathbf{F}}(\mathbf{r}_{\parallel}, \beta) \cdot \hat{\mathbf{J}}(\mathbf{r}_{\parallel}, -\beta) \right] d\mathbf{r}_{\parallel} = 0. \quad (2.32)$$

Next, replacing $\hat{\mathbf{F}}(\mathbf{r}_{\parallel}, \beta)$ and $\hat{\mathbf{F}}(\mathbf{r}_{\parallel}, -\beta)$ in Eq. (2.32) with their definition in terms of Green's dyadic that is provided in Eq. (2.22), we obtain:

$$\begin{aligned} & \iint \hat{\mathbf{G}}_{-\beta}(\mathbf{r}_{\parallel}, \mathbf{r}'_{\parallel}) \hat{\mathbf{J}}(\mathbf{r}'_{\parallel}, -\beta) \cdot \hat{\mathbf{J}}(\mathbf{r}_{\parallel}, \beta) d\mathbf{r}_{\parallel} d\mathbf{r}'_{\parallel} = \\ & \iint \hat{\mathbf{G}}_{\beta}(\mathbf{r}_{\parallel}, \mathbf{r}'_{\parallel}) \hat{\mathbf{J}}(\mathbf{r}'_{\parallel}, \beta) \cdot \hat{\mathbf{J}}(\mathbf{r}_{\parallel}, -\beta) d\mathbf{r}_{\parallel} d\mathbf{r}'_{\parallel}. \end{aligned} \quad (2.33)$$

This is valid for arbitrary sources, hence, it yields

$$\hat{\mathbf{G}}_{\beta}(\mathbf{r}_{\parallel}, \mathbf{r}'_{\parallel}) = \hat{\mathbf{G}}_{-\beta}^{\text{T}}(\mathbf{r}'_{\parallel}, \mathbf{r}_{\parallel}). \quad (2.34)$$

Hence, we can infer that this symmetry property of the Green's dyadic results in $\hat{\mathbf{G}}_m = \hat{\mathbf{F}}_m^{\text{R}}$, i.e.,

$$\begin{aligned} \hat{\mathbf{R}}_m(\mathbf{r}_{\parallel}, \mathbf{r}'_{\parallel}) &= -\frac{\hat{\mathbf{F}}_m(\mathbf{r}_{\parallel}) \otimes \hat{\mathbf{F}}_m^{\text{R}}(\mathbf{r}'_{\parallel})}{2N_m} = \\ & -\frac{1}{2N_m} \begin{bmatrix} \hat{\mathbf{E}}_m(\mathbf{r}_{\parallel}) \otimes \hat{\mathbf{E}}_m^{\text{R}}(\mathbf{r}'_{\parallel}) & i\hat{\mathbf{E}}_m(\mathbf{r}_{\parallel}) \otimes \hat{\mathbf{H}}_m^{\text{R}}(\mathbf{r}'_{\parallel}) \\ i\hat{\mathbf{H}}_m(\mathbf{r}_{\parallel}) \otimes \hat{\mathbf{E}}_m^{\text{R}}(\mathbf{r}'_{\parallel}) & -\hat{\mathbf{H}}_m(\mathbf{r}_{\parallel}) \otimes \hat{\mathbf{H}}_m^{\text{R}}(\mathbf{r}'_{\parallel}) \end{bmatrix}. \end{aligned} \quad (2.35)$$

Thus, the Green's dyadic for a waveguide geometries in the reciprocal β space is given by [A1, A2]

$$\hat{\mathbf{G}}_{\beta}(\mathbf{r}_{\parallel}, \mathbf{r}'_{\parallel}) = -\sum_m \frac{\hat{\mathbf{F}}_m(\mathbf{r}_{\parallel}) \otimes \hat{\mathbf{F}}_m^{\text{R}}(\mathbf{r}'_{\parallel})}{2N_m(\beta - \beta_m)}. \quad (2.36)$$

2.2.2 Green's dyadic in real space

In the previous subsection, we have derived the spectral representation of the Green's dyadic for waveguide geometries in the reciprocal β space. It allows us to find the solution of Eq. (2.13) for an arbitrary source using Eq. (2.22). Nevertheless, in most of the cases, we are interested to find the solutions of Maxwell's equations in real space. We can get the solution $\hat{\mathbf{F}}(\mathbf{r}_{\parallel}, \beta)$ in real space by simply using the inverse Fourier transform of Eq. (2.12):

$$\mathbf{F}(\mathbf{r}) = \iint \hat{\mathbf{G}}(\mathbf{r}_{\parallel}, \mathbf{r}'_{\parallel}, \beta) \hat{\mathbf{J}}(\mathbf{r}'_{\parallel}, \beta) e^{i\beta z} d\beta d\mathbf{r}'_{\parallel}. \quad (2.37)$$

Taking into account Eq. (2.11) and changing the order of integration, we can write

$$\begin{aligned} \mathbf{F}(\mathbf{r}) &= \int \left[\frac{1}{2\pi} \int \hat{\mathbf{G}}(\mathbf{r}_{\parallel}, \mathbf{r}'_{\parallel}, \beta) e^{i\beta(z-z')} d\beta \right] \mathbf{J}(\mathbf{r}') d\mathbf{r}' \\ &= \int \mathbf{G}(\mathbf{r}, \mathbf{r}') \mathbf{J}(\mathbf{r}') d\mathbf{r}'. \end{aligned} \quad (2.38)$$

Here, we note that the expression in square brackets defines the inverse Fourier transform of the spectral representation of the Green's dyadic back to the z space. Thus,

$$\begin{aligned} \mathbf{G}(\mathbf{r}, \mathbf{r}') &= \frac{1}{2\pi} \int \hat{\mathbf{G}}(\mathbf{r}_{\parallel}, \mathbf{r}'_{\parallel}, \beta) e^{i\beta(z-z')} d\beta = \\ &= -\frac{1}{2\pi} \sum_m \int \frac{\hat{\mathbf{F}}_m(\mathbf{r}_{\parallel}) \otimes \hat{\mathbf{F}}_m^{\mathbf{R}}(\mathbf{r}'_{\parallel})}{2N_m(\beta - \beta_m)} e^{i\beta(z-z')} d\beta. \end{aligned} \quad (2.39)$$

This integral can be evaluated by employing the Cauchy's integral formula [48]. As we can see in Fig. 2.1, there are two possible contours. Here, we have to keep in mind that the Green's dyadic contains pairs of

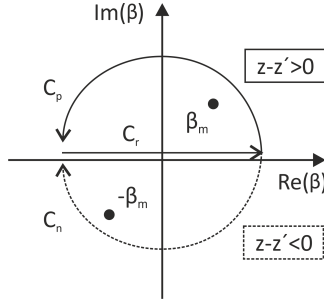


Figure 2.1. The poles and the contour of integration of the Green's dyadic on the complex β plane. The real axis line C_r can be closed on the complex half plane by C_p or C_n , depending on the observation position.

poles at $\beta = \pm\beta_m$ [35, 38]. When $z - z' > 0$, we may close the contour in the upper half plane (half circle C_p , solid line). If $z - z' < 0$, the

contour may be closed from below (half circle C_n , dashed line). Thus, we obtain [43, 48]:

$$\mathbf{G}(\mathbf{r}, \mathbf{r}') = \sum_m \frac{\hat{\mathbf{F}}_m(\mathbf{r}_{\parallel}) \otimes \hat{\mathbf{F}}_m^{\mathbf{R}}(\mathbf{r}'_{\parallel})}{2iN_m} e^{i\beta_m|z-z'|}. \quad (2.40)$$

Accordingly, the source field in real space is now given by

$$\mathbf{F}(\mathbf{r}) = \sum_m \frac{\hat{\mathbf{F}}_m(\mathbf{r}_{\parallel})}{2iN_m} \int \hat{\mathbf{F}}_m^{\mathbf{R}}(\mathbf{r}'_{\parallel}) \cdot \mathbf{J}(\mathbf{r}') e^{i\beta_m|z-z'|} d\mathbf{r}'. \quad (2.41)$$

Here, it should be noted the Green's dyadic and the fields are defined at a certain frequency.

2.3 POLES ON THE COMPLEX FREQUENCY PLANE

In the previous sections, we have expanded the Green's dyadic at a fixed frequency in the basis of resonant states that are defined on the complex β plane. However, alternatively, we can define the resonant states on the complex wave number (frequency) $k = \omega/c$ plane. In this case, the Green's dyadic has poles at $k = k_m$, which are the wave numbers of the resonant states of the system. Hence, it can be written as following [38, 39, 47, 50, 51]

$$\mathbf{G}_k(\mathbf{r}, \mathbf{r}') = \sum_m \frac{\mathbf{E}_m(\mathbf{r}) \otimes \mathbf{E}_m(\mathbf{r}')}{N_m k(k - k_m)}. \quad (2.42)$$

As it is already mentioned, in the first approach, we fix the frequency and search resonant states on the complex β plane. This is a more natural choice for guiding geometries with propagating modes that are typically characterized by propagation constant β_m [28]. While the second approach is more appropriate for open optical cavities, three-dimensional resonators and periodic structures [39, 47, 50, 51]. The latter description for guiding geometries would mean to fix real valued β and search for the resonant states on the complex frequency plane. This allows to consider global excitation of waveguide modes, e.g., induced by incident plane wave from the side of the optical fiber.

Before deriving our new normalization scheme for the resonant states of waveguide geometries, let us first discuss normalization schemes used for the resonant states defined on the complex frequency plane.

In most cases, the electric field \mathbf{E}_m of the mode of a resonator is normalized as [52]

$$N_m = \int_V \varepsilon(\mathbf{r}) \mathbf{E}_m^2(\mathbf{r}) d\mathbf{r}. \quad (2.43)$$

However, for an open resonators this volume integral diverges since the fields of an open system grow exponentially outside of the system due to their leakage. It can only be used for lossless systems or approximately for low loss cases by artificially choosing a finite integration volume [see Section 2.4.1]. In Refs. [53–56], it has been suggested the following normalization scheme:

$$N_m = \lim_{V \rightarrow \infty} \int_V \varepsilon(\mathbf{r}) \mathbf{E}_m^2(\mathbf{r}) d\mathbf{r} - \frac{1}{2ik_m} \oint_{S_V} \mathbf{E}_m^2(\mathbf{r}) dS, \quad (2.44)$$

where S_V is the surface that surrounds volume V . This normalization scheme provides much more accurate results for leaky modes of an open resonators in comparison to Eq. (2.43), because of the second surface term that suppresses divergence of the first volume integral. Despite that fact Eq. (2.44) works quite well in numerical simulations for a finite volume V , in Ref. [50] authors showed that it can diverge in the limit $V \rightarrow \infty$ and provided the correct mode normalization that can be written as [35, 39, 50]:

$$N_m = V_m + S_m, \quad (2.45)$$

with the volume term

$$V_m = \int_V \mathbf{E}_m(\mathbf{r}) \cdot \hat{\varepsilon}(\mathbf{r}) \mathbf{E}_m(\mathbf{r}) d\mathbf{r}, \quad (2.46)$$

and the surface term

$$S_m = \frac{1}{2k_m^2} \oint_{S_V} \left[\mathbf{E}_m(\mathbf{r}) \cdot \frac{\partial}{\partial s} (\mathbf{r} \cdot \nabla) \mathbf{E}_m(\mathbf{r}) - \frac{\partial \mathbf{E}_m(\mathbf{r})}{\partial s} \cdot (\mathbf{r} \cdot \nabla) \mathbf{E}_m(\mathbf{r}) \right] dS. \quad (2.47)$$

Here, $\hat{\varepsilon}$ is the permittivity tensor and $\partial/\partial s$ denotes the normal derivative.

In alternative to these analytical normalization schemes, one can extend real coordinates \mathbf{r} into the complex plane through a certain coordinate transformation that is essentially equivalent to absorbing boundary conditions. Such approaches are widely used in numerical calculations. For instance, a similar approach is introduced by authors in Ref. [31] for a description of plasmonic nanoresonators. We will discuss the concept of complex coordinate transformation a bit more in detail in the next section within the normalization of the resonant states of guiding geometries.

2.4 ANALYTIC MODE NORMALIZATION

In the previous sections, we have constructed the explicit form of the Green's dyadic that can be expressed as an expansion into the basis of resonant states. As we have mentioned previously, these states are the eigensolutions of Maxwell's equations in the absence of sources. This means that the electric $\hat{\mathbf{E}}_m$ and the magnetic $\hat{\mathbf{H}}_m$ field distributions of the resonant states are defined up to an arbitrary scalar factor. However, the Green's dyadic must be uniquely defined. That is why we have introduced the normalization constant N_m in Eq. (2.25) that is supposed to provide a correct weight for these field distributions.

In the last section, we have reviewed normalization of the modes of open resonators. In this section, we discuss different possibilities and ways for normalization of the resonant states of waveguide geometries. Hence, first of all, we review briefly the conventional normalization schemes from the literature. After this, we derive our analytical and rigorous normalization scheme for the resonant states.

2.4.1 Conventional normalization schemes

Traditionally, the normalization constant of the eigenstates of the homogeneous Maxwell's equations Eq. (2.14) is defined as an integral of the absolute square value of the electric fields

$$N_m = \int_{-\infty}^{+\infty} |\mathbf{E}_m(\mathbf{r}_{\parallel})|^2 d\mathbf{r}_{\parallel}, \quad (2.48)$$

or the axial component of the time-averaged Poynting vector $S_{m,z} = c\text{Re}[(\mathbf{E}_m \times \mathbf{H}_m^*)_z]/8\pi$ over the entire transverse region of the optical system [28]:

$$N_m = \int_{-\infty}^{+\infty} S_{m,z}(\mathbf{r}_{\parallel}) d\mathbf{r}_{\parallel}. \quad (2.49)$$

These definitions work well for the eigenfunctions that decay in the transverse region outside the optical system. According to the boundary condition Eq. (2.15), the bound and evanescent modes of waveguides fulfill this condition since their eigenvalues are real and purely positive imaginary numbers, respectively. Here, we note that these normalization schemes can be analytically calculated for simple step-profile fibers [57].

However, the resonant states of an open electromagnetic systems diverge in the transverse region. For example, this is the case for leaky modes of hollow-core waveguides. In this case, it is obvious that the normalization schemes Eq. (2.48) and Eq. (2.49) are not applicable in their current form, since $N_m = \infty$. Nevertheless, they can be still used under certain approximations. Here, as an example, we briefly consider two of them. The first and more straightforward approximation is based on the radiation caustic [28]. In order to explain the idea, let us consider a simple step-profile hollow-core fiber with $n_{\text{cl}} > n_{\text{co}}$. In Fig. 2.2 (a), it is shown a schematic representation of the intensity distribution of the fundamental leaky mode over the cross section of the fiber. There, we can define a cylindrical surface with radius r_{rad} (indicated by white dashed line) that corresponds to the minimum of the intensity distribution. This surface can be identified as the source of the leaky mode radiation [see Fig. 2.2 (b)] and therefore, it is called the radiation caustic [28].

Thus, in the region $0 \leq \rho < r_{\text{rad}}$, the fields of a leaky mode behave similar to the fields of a bound mode. Hence, the normalization constant Eq. (2.49) in the case of a leaky mode can be approximated as

$$N_m \approx \int_0^{2\pi} \int_0^{r_{\text{rad}}} \rho S_{m,z}(\rho, \phi) d\rho d\phi. \quad (2.50)$$

A similar approximation can also be done for Eq. (2.48).

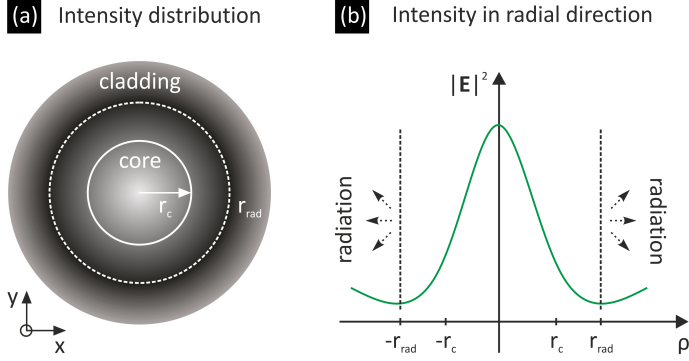


Figure 2.2. Schematic illustration of the radiation caustic that defines the area of integration in the normalization schemes Eq. (2.48) and Eq. (2.49). **(a)** The intensity distribution of the fundamental leaky mode of a step-profile hollow-core fiber with radius r_c . **(b)** The intensity distribution in radial direction. The minimum of the intensity at r_{rad} defines the so-called radiation caustic, i.e., the origin of radiation.

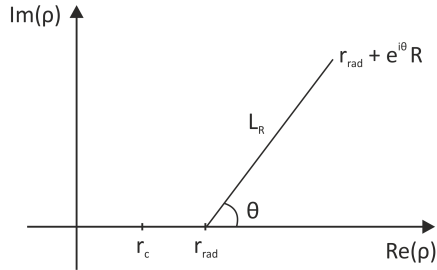


Figure 2.3. Schematic illustration of the contour of integration on the complex ρ plane in the normalization scheme Eq. (2.52). [Image is based on Fig. 1 from Ref. [30].]

The radiation caustic radius is defined in surrounding region of the fiber, i.e., $r_{\text{rad}} \geq r_c$. For low-order modes this radius is not sharply defined. Therefore, it is necessary to analyze the fields of every mode additionally. However, for high-order leaky modes (i.e., for the azimuthal mode number $m \gg 1$) it can be defined as following [28]:

$$r_{\text{rad}} = \frac{m}{\text{Re}(\chi_m^{\text{cl}})}. \quad (2.51)$$

It is important to note that the normalization based on the radiation caustic provides acceptable results only for bound and nearly bound modes with a small attenuation coefficient, i.e., $|\text{Im}(\beta_m)| \ll |\text{Re}(\beta_m)|$. Since the attenuation coefficient is $\text{Im}(\beta_m) \propto \lambda^2/r_c^3$ for hollow-core fibers [58], Eq. (2.50) can be used if the core radius of the fiber is much bigger than the wavelength of interest, i.e., $r_c \gg \lambda$.

In addition, based on the radiation caustic one can classify leaky modes [28]. The physical mechanism of the energy leakage through r_{rad} is known as tunneling. Hence, the modes for which the radiation caustic radius $r_c < r_{\text{rad}} < \infty$ are called tunneling leaky modes [59–61]. The modes in the case $r_{\text{rad}} = r_c$ are referred to as refracting leaky modes. In this context, it is clear that if $r_{\text{rad}} = \infty$, there is no energy leakage and the leaky mode becomes a bound mode.

In another approach, it is suggested to introduce a complex coordinate system to regions outside the spatial inhomogeneities for suppressing the divergence of leaky modes [29, 30]. As it can be seen in Fig. 2.3, this can be done by simply deforming the contour of integration into the complex ρ plane. The contour should be chosen in such a way that in the limit $R \rightarrow \infty$ and for a certain angle θ , the following normalization scheme based on Eq. (2.49) [similarly Eq. (2.48)] converges:

$$N_m = \lim_{R \rightarrow \infty} \int_0^{2\pi} \left(\int_0^{r_{\text{rad}}} \rho S_{m,z}(\rho, \phi) d\rho + \int_{L_R} \rho S_{m,z}(\rho, \phi) d\rho \right) d\phi. \quad (2.52)$$

Essentially, this approach is equivalent to the well-known perfectly matched layers (PML) that are widely used in different commercial technical simulation software packages such as Comsol Multiphysics [31, 50]. In comparison to the concept of the radiation caustic, the second approach is mathematically exact. However, it can be tedious to implement and the standard orthogonality conditions are not valid in this approach [28].

2.4.2 Analytical normalization scheme

As we have seen in the previous subsection, the normalization of resonant states is not straightforward within the conventional approaches. It becomes especially problematic for the resonant states of hollow-core waveguides. In order to solve this problem once and for all, in this section, we derive an exact analytical form of the normalization scheme.

For that, following other related works [A1, 35, 37, 38], let us consider Eq. (2.28a) and Eq. (2.28b) in the form:

$$\hat{\mathbb{M}}(\mathbf{r}_{\parallel}, \beta) \hat{\mathbf{F}}(\mathbf{r}_{\parallel}, \beta) = (\beta - \beta_m) \hat{\sigma}(\mathbf{r}_{\parallel}, \beta), \quad (2.53a)$$

$$\hat{\mathbb{M}}(\mathbf{r}_{\parallel}, -\beta_m) \hat{\mathbf{F}}_m^R(\mathbf{r}_{\parallel}) = 0. \quad (2.53b)$$

We multiply Eq. (2.53a) with $\hat{\mathbf{F}}_m^R$, and Eq. (2.53b) with $\hat{\mathbf{F}}$ from the left side. Then, subtracting the second expression from the first one, we obtain:

$$\begin{aligned} & \hat{\mathbf{F}}_m^R(\mathbf{r}_{\parallel}) \cdot \hat{\mathbb{M}}(\mathbf{r}_{\parallel}, \beta) \hat{\mathbf{F}}(\mathbf{r}_{\parallel}, \beta) - \hat{\mathbf{F}}(\mathbf{r}_{\parallel}, \beta) \cdot \hat{\mathbb{M}}(\mathbf{r}_{\parallel}, -\beta_m) \hat{\mathbf{F}}_m^R(\mathbf{r}_{\parallel}) = \\ & (\beta - \beta_m) \hat{\mathbf{F}}_m^R(\mathbf{r}_{\parallel}) \cdot \hat{\sigma}(\mathbf{r}_{\parallel}, \beta). \end{aligned} \quad (2.54)$$

Using the vector identity of Eq. (2.30), after some algebra, we obtain:

$$\begin{aligned} & \left[\nabla_{\parallel} + i(\beta - \beta_m) \hat{\mathbf{e}}_z \right] \cdot \left[\hat{\mathbf{E}}(\mathbf{r}_{\parallel}, \beta) \times \hat{\mathbf{H}}_m^R(\mathbf{r}_{\parallel}) - \hat{\mathbf{E}}_m^R(\mathbf{r}_{\parallel}) \times \hat{\mathbf{H}}(\mathbf{r}_{\parallel}, \beta) \right] = \\ & i(\beta - \beta_m) \hat{\mathbf{F}}_m^R(\mathbf{r}_{\parallel}) \cdot \hat{\sigma}(\mathbf{r}_{\parallel}, \beta), \end{aligned} \quad (2.55)$$

where $\hat{\mathbf{e}}_z$ denotes the unit vector in the z direction. Dividing by $\beta - \beta_m$, integrating over the spatial inhomogeneities in the limit $\beta \rightarrow \beta_m$, and taking into account Eq. (2.27), we get

$$\begin{aligned} & \lim_{\beta \rightarrow \beta_m} \int \frac{\nabla_{\parallel}}{i(\beta - \beta_m)} \cdot \left[\hat{\mathbf{E}}(\mathbf{r}_{\parallel}, \beta) \times \hat{\mathbf{H}}_m^R(\mathbf{r}_{\parallel}) - \hat{\mathbf{E}}_m^R(\mathbf{r}_{\parallel}) \times \hat{\mathbf{H}}(\mathbf{r}_{\parallel}, \beta) \right] d\mathbf{r}_{\parallel} + \\ & \int \left[\hat{\mathbf{E}}(\mathbf{r}_{\parallel}, \beta) \times \hat{\mathbf{H}}_m^R(\mathbf{r}_{\parallel}) - \hat{\mathbf{E}}_m^R(\mathbf{r}_{\parallel}) \times \hat{\mathbf{H}}(\mathbf{r}_{\parallel}, \beta) \right]_z d\mathbf{r}_{\parallel} = -2N_m. \end{aligned} \quad (2.56)$$

For evaluating the limit $\beta \rightarrow \beta_m$, we Taylor expand $\hat{\mathbf{F}}(\mathbf{r}_{\parallel}, \beta)$ around β_m :

$$\hat{\mathbf{F}}(\mathbf{r}_{\parallel}, \beta) = \sum_{n \geq 0} \frac{(\beta - \beta_m)^n}{n!} \frac{\partial^n \hat{\mathbf{F}}(\mathbf{r}_{\parallel}, \beta)}{\partial \beta^n} \Bigg|_{\beta_m}, \quad (2.57)$$

where $\hat{\mathbf{F}}$ stands for $\hat{\mathbf{E}}$ and $\hat{\mathbf{H}}$. Substituting Eq. (2.57) in Eq. (2.56) yields

$$\int \nabla_{\parallel} \cdot \left[\frac{\partial \hat{\mathbf{E}}(\mathbf{r}_{\parallel}, \beta)}{\partial \beta} \Big|_{\beta_m} \times \hat{\mathbf{H}}_m^{\text{R}}(\mathbf{r}_{\parallel}) - \hat{\mathbf{E}}_m^{\text{R}}(\mathbf{r}_{\parallel}) \times \frac{\partial \hat{\mathbf{H}}(\mathbf{r}_{\parallel}, \beta)}{\partial \beta} \Big|_{\beta_m} \right] d\mathbf{r}_{\parallel} + \int i \left[\hat{\mathbf{E}}(\mathbf{r}_{\parallel}, \beta) \times \hat{\mathbf{H}}_m^{\text{R}}(\mathbf{r}_{\parallel}) - \hat{\mathbf{E}}_m^{\text{R}}(\mathbf{r}_{\parallel}) \times \hat{\mathbf{H}}(\mathbf{r}_{\parallel}, \beta) \right]_z d\mathbf{r}_{\parallel} = -2iN_m. \quad (2.58)$$

The first term of Eq. (2.58) can be converted to a line integral by using the divergence theorem. If we use more convenient cylindrical coordinates, the curve of integration is a circle of radius R outside the region of inhomogeneities. Furthermore, using the aforementioned relations between $\hat{\mathbf{F}}_m^{\text{R}}$ and $\hat{\mathbf{F}}_m$ [see Eq. (2.16)], we can rewrite Eq. (2.58) in more compact form as [A1]

$$N_m = S_m + L_m, \quad (2.59)$$

with the surface term

$$S_m = \int_0^{2\pi} \int_0^R \rho (\hat{E}_{m,\rho} \hat{H}_{m,\phi} - \hat{E}_{m,\phi} \hat{H}_{m,\rho}) d\rho d\phi, \quad (2.60)$$

and the line term

$$L_m = \frac{\beta_m R}{2i\kappa_m} \int_0^{2\pi} \left[\frac{\partial \hat{E}_{m,\phi}}{\partial \kappa} \hat{H}_{m,z} + \frac{\partial \hat{E}_{m,z}}{\partial \kappa} \hat{H}_{m,\phi} - \frac{\partial \hat{H}_{m,\phi}}{\partial \kappa} \hat{E}_{m,z} - \frac{\partial \hat{H}_{m,z}}{\partial \kappa} \hat{E}_{m,\phi} \right]_{\beta_m, R} d\phi. \quad (2.61)$$

Here, $\kappa = (n_{\text{sur}}^2 k_o^2 - \beta^2)^{1/2}$ and n_{sur} is the refractive index of the homogeneous surrounding. Note that the surface S_m and the line L_m terms of normalization N_m , as well as the field distributions are written in cylindrical coordinates. The second index in the fields stand for the corresponding vector field component. Furthermore, the subscripts β_m and R at the right rectangular bracket of Eq. (2.61) denote that the integrand should be evaluated at these parameters.

The current form of the line term, i.e., Eq. (2.61) contains the derivatives with respect to the untypical variable κ . In order to convert them

into the usual spatial derivatives, first, we use the following relations between the κ and ρ derivatives of the axial components of the fields:

$$\frac{\partial \hat{E}_{m,z}}{\partial \kappa} = \frac{\rho}{\kappa} \frac{\partial \hat{E}_{m,z}}{\partial \rho}, \quad (2.62a)$$

$$\frac{\partial \hat{H}_{m,z}}{\partial \kappa} = \frac{\rho}{\kappa} \frac{\partial \hat{H}_{m,z}}{\partial \rho}. \quad (2.62b)$$

Next, the in-plane components of the fields can be expressed by the axial one as [28, 41]:

$$\hat{E}_{m,\rho} = \frac{i\beta}{\kappa^2} \frac{\partial \hat{E}_{m,z}}{\partial \rho} + \frac{ik_o\mu}{\kappa^2\rho} \frac{\partial \hat{H}_{m,z}}{\partial \phi}, \quad (2.63a)$$

$$\hat{H}_{m,\rho} = \frac{i\beta}{\kappa^2} \frac{\partial \hat{H}_{m,z}}{\partial \rho} - \frac{ik_o\varepsilon}{\kappa^2\rho} \frac{\partial \hat{E}_{m,z}}{\partial \phi}, \quad (2.63b)$$

$$\hat{E}_{m,\phi} = \frac{i\beta}{\kappa^2\rho} \frac{\partial \hat{E}_{m,z}}{\partial \phi} - \frac{ik_o\mu}{\kappa^2} \frac{\partial \hat{H}_{m,z}}{\partial \rho}, \quad (2.63c)$$

$$\hat{H}_{m,\phi} = \frac{i\beta}{\kappa^2\rho} \frac{\partial \hat{H}_{m,z}}{\partial \phi} + \frac{ik_o\varepsilon}{\kappa^2} \frac{\partial \hat{E}_{m,z}}{\partial \rho}. \quad (2.63d)$$

Finally, we can write the following integral identity

$$\int_0^{2\pi} d\phi \frac{\partial f}{\partial \phi} g = - \int_0^{2\pi} d\phi f \frac{\partial g}{\partial \phi}, \quad (2.64)$$

where f and g stand for components of $\hat{\mathbf{E}}_m$ and $\hat{\mathbf{H}}_m$, respectively. Thus, taking into account all these relations and after some algebra and rear-

rangements, we can write the line term in more symmetrical form with respect to the electric and the magnetic fields [A1]:

$$\begin{aligned}
 L_m = & \frac{\varepsilon \mu k_o^2 + \beta_m^2}{2\chi_m^4} \int_0^{2\pi} \left(\hat{E}_{m,z} \frac{\partial \hat{H}_{m,z}}{\partial \phi} - \hat{H}_{m,z} \frac{\partial \hat{E}_{m,z}}{\partial \phi} \right) d\phi + \\
 & \frac{k_o \beta_m R^2}{2\chi_m^4} \int_0^{2\pi} \left\{ \mu \left[\left(\frac{\partial \hat{H}_{m,z}}{\partial \rho} \right)^2 - \rho \hat{H}_{m,z} \frac{\partial}{\partial \rho} \left(\frac{1}{\rho} \frac{\partial \hat{H}_{m,z}}{\partial \rho} \right) \right] + \right. \\
 & \left. \varepsilon \left[\left(\frac{\partial \hat{E}_{m,z}}{\partial \rho} \right)^2 - \rho \hat{E}_{m,z} \frac{\partial}{\partial \rho} \left(\frac{1}{\rho} \frac{\partial \hat{E}_{m,z}}{\partial \rho} \right) \right] \right\} d\phi. \quad (2.65)
 \end{aligned}$$

In addition to the unique normalization scheme, the resonant states of a certain waveguide geometry satisfy a certain orthogonality condition. In order to derive this orthogonality relation, we consider the following two equations:

$$\hat{M}(\mathbf{r}_{\parallel}, \beta_m) \hat{F}_m(\mathbf{r}_{\parallel}) = 0, \quad (2.66a)$$

$$\hat{M}(\mathbf{r}_{\parallel}, -\beta_m) \hat{F}_m^R(\mathbf{r}_{\parallel}) = 0. \quad (2.66b)$$

After repeating the steps that have been done to derive the normalization, for $\beta_n \neq \beta_m$, we obtain the orthogonality condition for resonant states [see Section 5.1.2]:

$$\begin{aligned}
 \int \left[\nabla_{\parallel} + i(\beta_n - \beta_m) \hat{e}_z \right] \cdot \left[\hat{E}_n(\mathbf{r}_{\parallel}) \times \hat{H}_m^R(\mathbf{r}_{\parallel}) - \right. \\
 \left. \hat{E}_m^R(\mathbf{r}_{\parallel}) \times \hat{H}_n(\mathbf{r}_{\parallel}) \right] d\mathbf{r}_{\parallel} = 0. \quad (2.67)
 \end{aligned}$$

2.4.3 Example: Step-profile fiber

Here, as an example, we apply our analytical normalization scheme to a simple step-profile fiber. For that, first of all, we have to find the exact eigensolutions of Eq. (2.14) for

$$\varepsilon(\mathbf{r}_{\parallel}) = \begin{cases} n_{co}^2 & \text{for } \rho < r_c, \\ n_{cl}^2 & \text{for } \rho > r_c, \end{cases} \quad (2.68)$$

and $\mu(\mathbf{r}_{||}) = 1$. In this case, for the z component $\hat{F}_{m,z}$ of the field $\hat{\mathbf{F}}_m$, we can make the following ansatz:

$$\hat{F}_{m,z}(\mathbf{r}_{||}) = \begin{cases} F_o^{\text{co}} J_m(\chi_m^{\text{co}} \rho) e^{im\phi} & \text{for } \rho < r_c, \\ F_o^{\text{cl}} H_m^{(1)}(\chi_m^{\text{cl}} \rho) e^{im\phi} & \text{for } \rho > r_c, \end{cases} \quad (2.69)$$

where J_m and $H_m^{(1)}$ are Bessel and the first kind Hankel functions, respectively, and $F_o^{\text{co}} = (E_o^{\text{co}}, H_o^{\text{co}})^T$ and $F_o^{\text{cl}} = (E_o^{\text{cl}}, H_o^{\text{cl}})^T$ are their amplitudes in the core and cladding regions, respectively. By using the boundary conditions that $\hat{F}_{m,z}$ and $\hat{F}_{m,\phi}$ must be continuous, including at $\rho = r_c$, this yields eigenvalue problem [28, 41]:

$$\begin{pmatrix} R_m^{\text{co}} & 0 & -R_m^{\text{cl}} & 0 \\ 0 & R_m^{\text{co}} & 0 & -\frac{n_{\text{cl}}}{n_{\text{co}}} R_m^{\text{cl}} \\ \frac{\beta_m}{k_{\text{co}}} Y_m^{\text{co}} & -X_m^{\text{co}} & -\frac{\beta_m \chi_m^{\text{co}}}{k_{\text{co}} \chi_m^{\text{cl}}} Y_m^{\text{cl}} & \frac{n_{\text{cl}} \chi_m^{\text{co}}}{n_{\text{co}} \chi_m^{\text{cl}}} X_m^{\text{cl}} \\ X_m^{\text{co}} & -\frac{\beta_m}{k_{\text{co}}} Y_m^{\text{co}} & -\frac{n_{\text{cl}}^2 \chi_m^{\text{co}}}{n_{\text{co}}^2 \chi_m^{\text{cl}}} X_m^{\text{cl}} & \frac{n_{\text{cl}} \beta_m \chi_m^{\text{co}}}{n_{\text{co}} k_{\text{co}} \chi_m^{\text{cl}}} Y_m^{\text{cl}} \end{pmatrix} \begin{pmatrix} E_o^{\text{co}} \\ H_o^{\text{co}} \\ E_o^{\text{cl}} \\ H_o^{\text{cl}} \end{pmatrix} = 0, \quad (2.70)$$

with

$$R_m^{\text{co}} \equiv R_m^{\text{co}}(\chi_m^{\text{co}} r_c) = J_m(\chi_m^{\text{co}} r_c), \quad (2.71a)$$

$$R_m^{\text{cl}} \equiv R_m^{\text{cl}}(\chi_m^{\text{cl}} r_c) = H_m^{(1)}(\chi_m^{\text{cl}} r_c), \quad (2.71b)$$

$$X_m^{\text{reg}} = \frac{1}{2} [R_{m-1}^{\text{reg}} - R_{m+1}^{\text{reg}}], \quad (2.71c)$$

$$Y_m^{\text{reg}} = \frac{1}{2} [R_{m-1}^{\text{reg}} + R_{m+1}^{\text{reg}}]. \quad (2.71d)$$

Here, $k_{\text{reg}} = n_{\text{reg}} k_o$, and "reg" (region) stands for "co" (core) and "cl" (cladding). The zeros of the determinant of the 4×4 matrix in Eq. (2.70) correspond to the eigenvalues β_m of the system.

After some algebra, we obtain the exact form of the amplitudes:

$$E_o^{\text{co}} = E_o, \quad (2.72a)$$

$$E_o^{\text{cl}} = \frac{R_m^{\text{co}}}{R_m^{\text{cl}}} E_o, \quad (2.72b)$$

$$H_o^{\text{co}} = \frac{\beta_m}{k_{\text{co}}} \frac{Y_m^{\text{co}} E_o^{\text{co}} - \frac{\chi_m^{\text{co}}}{\chi_m^{\text{cl}}} Y_m^{\text{cl}} E_o^{\text{cl}}}{X_m^{\text{co}} - \frac{\chi_m^{\text{co}}}{\chi_m^{\text{cl}}} \frac{R_m^{\text{co}}}{R_m^{\text{cl}}} X_m^{\text{cl}}}, \quad (2.72c)$$

$$H_o^{\text{cl}} = \frac{k_{\text{cl}}}{k_{\text{co}}} \frac{R_m^{\text{co}}}{R_m^{\text{cl}}} H_o^{\text{co}}, \quad (2.72d)$$

where E_o is an arbitrary constant. As it is shown in Eqs. (2.63a) to (2.63d), the $\hat{F}_{m,\rho}$ and $\hat{F}_{m,\phi}$ components of the mode field $\hat{\mathbf{F}}_m$ can be expressed by its $\hat{F}_{m,z}$ component [28, 41]. Thus, using these solutions, after some simplifications, we obtain the following analytical expressions for the surface S_m and line L_m terms:

$$S_m = n_{\text{co}} S_m^{\text{co}} + n_{\text{cl}} S_m^{\text{cl}}, \quad (2.73)$$

$$L_m = n_{\text{cl}} L_m^{\text{cl}}, \quad (2.74)$$

with

$$S_m^{\text{reg}} = C_1^{\text{reg}} \left[\left(E_o^{\text{reg}} \right)^2 + \left(H_o^{\text{reg}} \right)^2 \right] \left(\left. I_{m-1}^{\text{reg}}(\rho) \right|_o^{r_c} + \left. I_{m+1}^{\text{reg}}(\rho) \right|_o^{r_c} \right) - C_2^{\text{reg}} E_o^{\text{reg}} H_o^{\text{reg}} \left(\left. I_{m-1}^{\text{reg}}(\rho) \right|_{r_c}^R - \left. I_{m+1}^{\text{reg}}(\rho) \right|_{r_c}^R \right), \quad (2.75)$$

and

$$L_m^{\text{cl}} = -C_1^{\text{cl}} \left[\left(E_o^{\text{cl}} \right)^2 + \left(H_o^{\text{cl}} \right)^2 \right] \left(\left. I_{m-1}^{\text{cl}}(\rho) \right|^R + \left. I_{m+1}^{\text{cl}}(\rho) \right|^R \right) + C_2^{\text{cl}} E_o^{\text{cl}} H_o^{\text{cl}} \left(\left. I_{m-1}^{\text{cl}}(\rho) \right|^R - \left. I_{m+1}^{\text{cl}}(\rho) \right|^R \right). \quad (2.76)$$

In these equations $I_m^{reg}(\rho)$ defines the integral of the squared Bessel functions [62]:

$$I_m^{reg}(\rho) = \int \rho \left[R_m^{reg}(\chi_m^{reg} \rho) \right]^2 d\rho = \frac{\rho^2}{2} \left\{ \left[R_m^{reg}(\chi_m^{reg} \rho) \right]^2 - R_{m-1}^{reg}(\chi_m^{reg} \rho) R_{m+1}^{reg}(\chi_m^{reg} \rho) \right\}. \quad (2.77)$$

Finally, the coefficients C_1^{reg} and C_2^{reg} are defined as

$$C_1^{reg} = -\frac{\pi \beta_m k_{reg}}{2 (\chi_m^{reg})^2}, \quad (2.78a)$$

$$C_2^{reg} = -\frac{\pi \beta_m^2 + k_{reg}^2}{2 (\chi_m^{reg})^2}. \quad (2.78b)$$

In the case of TE and TM modes ($m = 0$), C_1^{reg} and C_2^{reg} must be multiplied by factor of 2 since their fields do not depend on ϕ . Furthermore, one can note that $L_m^{cl} = -2S_m^{cl}$. Hence, we can write

$$N_m = n_{co} S_m^{co} - n_{cl} S_m^{cl}. \quad (2.79)$$

Let us now consider the fundamental bound and leaky modes of two geometries with a core radius $r_c = 0.3 \mu\text{m}$ at a wavelength of $\lambda_o = 800 \text{ nm}$. In the first geometry, we assume that the fiber core is made of bismuth oxide (Bi_2O_3) doped glass with refractive index of $n_{co} = 2.05$ [63] and air cladding with $n_{cl} = 1$. The fiber with these parameters carries bound modes and the panel (a) of Fig. 2.4 displays the spatial distribution of the z -component of the real-valued Poynting vector of the fundamental bound mode that propagates with the propagation constant $\beta_m = 14.455 \mu\text{m}^{-1}$. We can see that the fields of the bound mode decay exponentially outside of the core and fully satisfy the boundary condition Eq. (2.15).

Fig. 2.4 (b) shows the fundamental leaky mode ($\beta_m = 11.15 + 1.63i \mu\text{m}^{-1}$) of the second geometry, which is a step-profile hollow-core fiber. The fiber has the same geometrical parameters as in the first one, but the core is filled by carbon disulfide (CS_2) with refractive index of $n = 1.6$ [64], while the cladding material is bismuth oxide (Bi_2O_3) doped glass with refractive index of $n_{co} = 2.05$. In contrast to the bound modes that exist in the first geometry, the second geometry exhibit the leaky modes with fields that grow in the exterior with distance from the core.

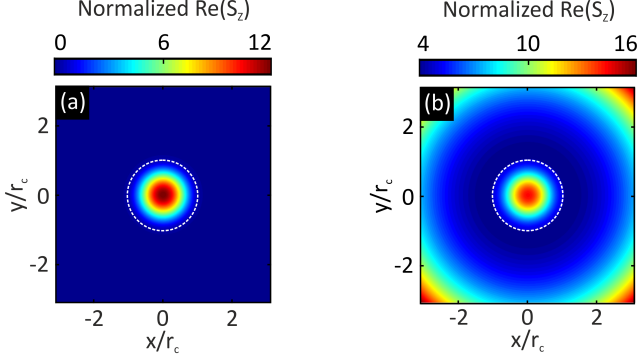


Figure 2.4. Spatial distribution of the z -component of the real-valued Poynting vector of the fundamental fiber modes at $\lambda_o = 800$ nm for two geometries with core radius $r_c = 0.3 \mu\text{m}$ (indicated by white dashed circle): (a) Bound mode in a cylindrical step-index fiber with bismuth oxide (Bi_2O_3) doped glass core with refractive index of $n = 2.05$ and air cladding with $n = 1$, (b) leaky mode in a Bi_2O_3 capillary filled with carbon disulfide (CS_2 , $n = 1.6$). The effective refractive index $n_{\text{eff}} = \beta_m/k_o$ of the corresponding fundamental modes are $n_{\text{eff}} = 1.84$ and $n_{\text{eff}} = 1.42 + 0.21i$, respectively. The mode fields are normalized with respect to Eq. (2.59) and the corresponding normalization constants are $N_m = -0.645$ and $N_m = 0.37 - 0.66i$, respectively.

Panels (a) and (b) in Fig. 2.5 display the real and the imaginary parts of the surface S_m and the line L_m terms of the normalization as well as the total normalization constant N_m of the fundamental leaky mode of the second geometry [see Fig. 2.4 (b)] as a function of the radius of normalization r_n . As we can see, the surface S_m and the line L_m terms oscillate and diverge since the fields grow in the cladding region. However, the total normalization constant N_m does not depend on the radius of normalization. Similar pictures can be obtained for all other higher-order hybrid $\text{HE}_{mn}/\text{EH}_{mn}$ and transverse $\text{TE}_{mn}/\text{TM}_{mn}$ modes.

Let us now repeat the calculations for the fundamental bound mode [see Fig. 2.4 (a)]. The results are shown in Fig. 2.6. As we can see, the real part of the surface S_m and the line L_m terms are already converged at $r_n = 1.5r_c$, while their imaginary parts are zero. As in the previous case, the sum of S_m and L_m remains constant for all r_n and gives the normalization constant N_m . Furthermore, for bound modes the line term vanishes at $r_n \rightarrow \infty$ as expected.

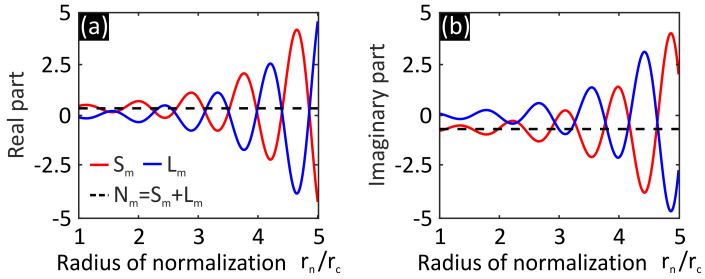


Figure 2.5. The real (a) and imaginary (b) parts of the surface term S_m (red solid line) and line term L_m (blue solid line) of the analytical normalization Eq. (2.59) for the fundamental leaky mode shown in Fig. 2.4 (b) as a function of the radius of normalization r_n . The surface and line terms diverge due to the divergent nature of the leaky mode fields, while their sum gives the normalization constant $N_m = 0.37 - 0.66i$ (black dashed line).

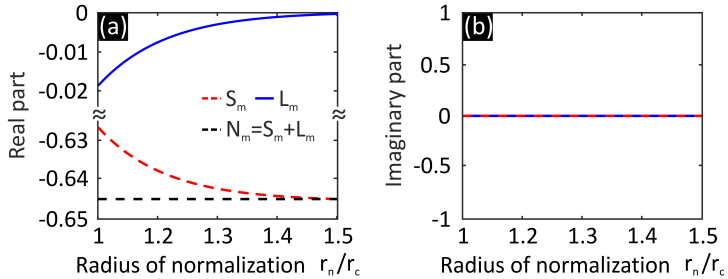


Figure 2.6. The real (a) and imaginary (b) parts of the surface term S_m (red dashed line) and line term L_m (blue solid line) of the analytical normalization Eq. (2.59) for the fundamental bound mode shown in Fig. 2.4 (a) as a function of the radius of normalization r_n . The surface and line terms converge exponentially and their sum gives the normalization constant $N_m = -0.645$ (black dashed line).

Thus, we showed that our new normalization scheme can be applied for both bound and leaky modes of waveguide geometries. Within the new scheme, in order to calculate the exact normalization constant, one can use the minimum area that includes all spatial inhomogeneities. As we will see in the next chapters, this distinctive feature of the new normalization scheme becomes important in the description of the nonlinear pulse propagation.

In conclusion, in this chapter, we provided a brief introduction to the resonant-state expansion. Following the previous works, we have constructed the Green's dyadic *ab initio* from the Maxwell's equations using eigensolutions of the waveguide that we define as the resonant states. Furthermore, we have derived the correct normalization scheme and the orthogonality condition for the resonant states. Additionally, as an example, we have applied this normalization scheme for bound and leaky modes of a step-profile fibers and obtained the exact analytical form of the normalization.

~

This chapter is based on the following publication [A2]:

I. Allayarov, S. Upendar, M. A. Schmidt, and T. Weiss: "*Analytic mode normalization for the Kerr nonlinearity parameter: Prediction of nonlinear gain for leaky modes*", Phys. Rev. Lett., **121** 213905 (2018).
DOI 10.1103/physrevlett.121.213905

In this chapter, we use an expansion of Green's dyadic with the analytic mode normalization that has been obtained in the previous chapter to derive a master equation for the nonlinear pulse propagation that allows for a rigorous description of both bound and leaky modes in waveguide geometries. After obtaining the master equation, we consider its particular case, namely in the single-mode approximation that simplifies to the standard nonlinear Schroedinger equation. In the framework of approximation, we discuss our new vectorial approach for the Kerr nonlinearity parameter that has a nonvanishing imaginary part and compare it with conventional formulations. At the end of the chapter, we investigate the impact of the imaginary part of the Kerr nonlinearity parameter on the pulse broadening within numerical simulations.

3.1 DERIVATION OF GENERAL MASTER EQUATION

In the previous chapter, we have derived an expansion of the Green's dyadic in terms of resonant states. This allows us to express the resulting field $\hat{\mathbf{F}}$ for an arbitrary source $\hat{\mathbf{J}}$ in Eq. (2.13) as:

$$\hat{\mathbf{F}}(\mathbf{r}_{\parallel}, \beta; \omega) = \int \hat{\mathbf{G}}_{\beta}(\mathbf{r}_{\parallel}, \mathbf{r}'_{\parallel}; \omega) \hat{\mathbf{J}}(\mathbf{r}'_{\parallel}, \beta; \omega) d\mathbf{r}'_{\parallel} =$$

$$- \sum_m \frac{\hat{\mathbf{F}}_m(\mathbf{r}_{\parallel}; \omega)}{2N_m[\beta - \beta_m(\omega)]} \int \hat{\mathbf{F}}_m^R(\mathbf{r}'_{\parallel}; \omega) \cdot \hat{\mathbf{J}}(\mathbf{r}'_{\parallel}, \beta; \omega) d\mathbf{r}'_{\parallel}. \quad (3.1)$$

Next, we can make the ansatz that the field on the left hand side can be expressed as a superposition of resonant states, i.e.,

$$\hat{\mathbf{F}}(\mathbf{r}_{||}, \beta; \omega) = \sum_m \hat{a}_m(\beta, \omega) \frac{1}{N_m^{1/2}} \hat{\mathbf{F}}_m(\mathbf{r}_{||}; \omega), \quad (3.2)$$

where \hat{a}_m is the modal amplitude. By comparing the right hand side of Eq. (3.1) with ansatz Eq. (3.2), and evaluating the result for each $\hat{\mathbf{F}}_m$ independently, we obtain:

$$i[\beta - \beta_m(\omega)] \hat{a}_m(\beta, \omega) = \frac{1}{2iN_m^{1/2}} \int \hat{\mathbf{F}}_m^{\mathbf{R}}(\mathbf{r}_{||}; \omega) \cdot \hat{\mathbf{J}}(\mathbf{r}_{||}, \beta; \omega) d\mathbf{r}_{||}. \quad (3.3)$$

Applying the inverse Fourier transform of Eq. (2.12) to Eq. (3.3) yields

$$\left[\frac{\partial}{\partial z} - i\beta_m(\omega) \right] a_m(z; \omega) = \frac{1}{2iN_m^{1/2}} \int \mathbf{F}_m^{\mathbf{R}}(\mathbf{r}_{||}; \omega) \cdot \mathbf{J}(\mathbf{r}_{||}, z; \omega) d\mathbf{r}_{||}. \quad (3.4)$$

For the system without external current source

$$\mathbf{J}(\mathbf{r}_{||}, z; \omega) = \begin{bmatrix} -\frac{4\pi\omega}{c} \mathbf{P}_{\text{NL}}(\mathbf{r}_{||}, z; \omega) \\ \mathbf{o} \end{bmatrix}, \quad (3.5)$$

i.e, the nonlinear polarization becomes the main source, which yields

$$\left[\frac{\partial}{\partial z} - i\beta_m(\omega) \right] a_m(z; \omega) = \frac{2\pi i \omega}{c} \int \mathbf{e}_m^{\mathbf{R}}(\mathbf{r}_{||}; \omega) \cdot \mathbf{P}_{\text{NL}}(\mathbf{r}_{||}, z; \omega) d\mathbf{r}_{||}, \quad (3.6)$$

where $\mathbf{e}_m^{\mathbf{R}} \equiv \mathbf{E}_m^{\mathbf{R}}/N_m^{1/2}$ is the normalized reciprocal conjugate electric field.

Finally, after transformation from frequency to time domain using Eq. (2.7), we obtain the general master equation for the nonlinear pulse propagation:

$$\begin{aligned} \frac{\partial a_m(z; t)}{\partial z} &= i\beta_m(t) * a_m(z; t) \\ &\quad - \frac{2\pi}{c} \frac{\partial}{\partial t} \int \mathbf{e}_m^{\mathbf{R}}(\mathbf{r}_{||}; t) * \mathbf{P}_{\text{NL}}(\mathbf{r}; t) d\mathbf{r}_{||}. \end{aligned} \quad (3.7)$$

Here, $*$ denotes convolutions in time domain. This equation is fully vectorial and contains no approximation so far. The only limitation of

Eq. (3.7) is that the expansion of the Green's dyadic in terms of resonant states is not straightforward in the external regions outside the spatial inhomogeneities [47, 51, 65]. Thus, the nonlinear polarization should be restricted to the region of spatial inhomogeneities, i.e., excluding the homogeneous exterior.

3.2 NONLINEAR SCHROEDINGER EQUATION

The general master equation for the nonlinear pulse propagation in waveguide geometries contains the nonlinear polarization as a source in general form. In this section, we consider the nonlinear polarization within a certain approximations and obtain the corresponding propagation equation, namely the well-known nonlinear Schroedinger equation.

In general, the nonlinear polarization \mathbf{P}_{NL} can be expressed as a power series in the electric field \mathbf{E} as

$$\begin{aligned} \mathbf{P}_{\text{NL}}(\mathbf{r}; t) = & \chi_e^{(2)}(t) * \mathbf{E}(\mathbf{r}; t)\mathbf{E}(\mathbf{r}; t) + \\ & \chi_e^{(3)}(t) * \mathbf{E}(\mathbf{r}; t)\mathbf{E}(\mathbf{r}; t)\mathbf{E}(\mathbf{r}; t) + \\ & \chi_e^{(4)}(t) * \mathbf{E}(\mathbf{r}; t)\mathbf{E}(\mathbf{r}; t)\mathbf{E}(\mathbf{r}; t)\mathbf{E}(\mathbf{r}; t) + \dots \quad (3.8) \end{aligned}$$

In Eq. (3.8), the first term vanishes in most cases, since the second-order electric susceptibility $\chi_e^{(2)} = 0$ for an isotropic medium such as liquids, gases, and glasses [9]. Hence, we solely consider the third-order nonlinear term with $\chi_e^{(3)}$ as the dominating contribution in \mathbf{P}_{NL} [5]. While the fourth- and other higher-order contributions can become relevant in specific nonlinear polymers [e.g., polydiacetylene para-toluene sulfonate (PTS) [66]] and semiconductor-doped glasses at relatively high pulse intensity [67, 68], their impact can be neglected in our case.

For further simplification, we firstly assume an instantaneous third-order nonlinear response, i.e., $\chi_e^{(3)}(t) = \chi_e^{(3)}\delta(t - t')$. The third-order electric susceptibility $\chi_e^{(3)}$ is a fourth-rank tensor, due to the vectorial nature of the fields, and its components depend on the class of the crystal. The spatial symmetry of an isotropic medium restricts $3^4 = 81$ elements of $\chi_{e,ijkl}^{(3)}$, where $(i, j, k, l = x, y, z)$, to 21 nonzero elements, of

which only three are independent [9]. Hence, these nonzero elements can be expressed as [9, 15]:

$$\chi_{e,ijkl}^{(3)} = \chi_{e,xxyy}^{(3)}\delta_{ij}\delta_{kl} + \chi_{e,xyxy}^{(3)}\delta_{ik}\delta_{jl} + \chi_{e,xyyx}^{(3)}\delta_{il}\delta_{jk}, \quad (3.9)$$

and diagonal elements of the tensor are

$$\chi_{e,iiii}^{(3)} = \chi_{e,xxyy}^{(3)} + \chi_{e,xyxy}^{(3)} + \chi_{e,xyyx}^{(3)}. \quad (3.10)$$

Additionally, by using intrinsic permutation symmetry of the tensor and taking into account the nonresonant electronic nature of the nonlinearity, we can write $\chi_{e,xxyy}^{(3)} = \chi_{e,xyxy}^{(3)} \approx \chi_{e,xyyx}^{(3)}$ [9]. Finally, all these approximations allow us to write the following:

$$\mathbf{P}_{\text{NL}}(\mathbf{r}; t) = \frac{\chi_{e,xxxx}^{(3)}}{4} \left[2\mathbf{E}(\mathbf{r}; t)|\mathbf{E}^*(\mathbf{r}; t)|^2 + \mathbf{E}^*(\mathbf{r}; t)\mathbf{E}^2(\mathbf{r}; t) \right]. \quad (3.11)$$

For the electric fields in Eq. (3.11), we use the Fourier transform of Eq. (3.2) from frequency to time domain. Considering pulses that are centered around a frequency ω_0 with a finite spectral width, and assuming that \mathbf{e}_m depends only weakly on the frequency around ω_0 , the fields can be written as

$$\begin{aligned} \mathbf{E}(\mathbf{r}; t) &= \sum_m a_m(z; t) * \mathbf{e}_m(\mathbf{r}_{\parallel}; t) + \text{c.c.} \\ &\approx \sum_m a_m(z; t) \mathbf{e}_m(\mathbf{r}_{\parallel}) + \text{c.c.} \\ &= \mathbf{e}_o(\mathbf{r}; t) e^{-i\omega_0 t} + \text{c.c.}, \end{aligned} \quad (3.12)$$

where $\mathbf{e}_m(\mathbf{r}_{\parallel}) \equiv \mathbf{e}_m(\mathbf{r}_{\parallel}; \omega_0)$, and $\mathbf{e}_o(\mathbf{r}; t)$ is the envelope for the dominant plane wave with frequency ω_0 .

Thus, the propagation equation becomes

$$\begin{aligned} \frac{\partial a_m(z; t)}{\partial z} &\approx i\beta_m(t) * a_m(z; t) - \\ &\frac{1}{c} \sum_{n,p,q} \frac{\partial}{\partial t} \left[\alpha_{mnpq} a_n(z; t) a_p^*(z; t) a_q(z; t) \right], \end{aligned} \quad (3.13)$$

with the overlap integral

$$\alpha_{mnpq} = \int n_2(\mathbf{r}_{\parallel}) \left\{ 2 \left[\mathbf{e}_m^R(\mathbf{r}_{\parallel}) \cdot \mathbf{e}_q(\mathbf{r}_{\parallel}) \right] \left[\mathbf{e}_n(\mathbf{r}_{\parallel}) \cdot \mathbf{e}_p^*(\mathbf{r}_{\parallel}) \right] + \left[\mathbf{e}_m^R(\mathbf{r}_{\parallel}) \cdot \mathbf{e}_p^*(\mathbf{r}_{\parallel}) \right] \left[\mathbf{e}_n(\mathbf{r}_{\parallel}) \cdot \mathbf{e}_q(\mathbf{r}_{\parallel}) \right] \right\} d\mathbf{r}_{\parallel}. \quad (3.14)$$

Here, $n_2 = 2\pi\chi_{e,xxxx}^{(3)}/4$ is the nonlinear refractive index. In the single-mode approximation, we can transform Eq. (3.13) into the standard nonlinear Schroedinger equation. For that, firstly, we separate β_m into real and imaginary parts $\bar{\beta}_m$ and $\bar{\alpha}_m$, respectively. Expanding them into Taylor series around ω_o yields

$$\beta_m(\omega) \equiv \bar{\beta}_m(\omega) + i\bar{\alpha}_m(\omega) \approx \sum_{n \geq 0} \left(\frac{\bar{\beta}_m^{(n)}}{n!} + i \frac{\bar{\alpha}_m^{(n)}}{n!} \right) (\omega - \omega_o)^n, \quad (3.15)$$

where

$$\bar{\beta}_m^{(n)} = \left. \frac{\partial^n \bar{\beta}_m}{\partial \omega^n} \right|_{\omega_o}, \quad (3.16a)$$

$$\bar{\alpha}_m^{(n)} = \left. \frac{\partial^n \bar{\alpha}_m}{\partial \omega^n} \right|_{\omega_o}, \quad (3.16b)$$

are the n th-order dispersion and loss coefficients, respectively. However, here, we only keep up to the second-order dispersion and assume a constant modal loss with $\bar{\alpha}_m(\omega) \approx \bar{\alpha}_m(\omega_o) \equiv \bar{\alpha}_m^{(o)}$. Hence, by introducing

$$a_m(z; t) \equiv A_m(z; t) e^{-i\omega_o t + i\bar{\beta}_m^{(o)} z}, \quad (3.17)$$

we obtain the well-known nonlinear Schoedinger equation [5]

$$\begin{aligned} \frac{\partial A_m(z; \tau)}{\partial z} &\approx i\gamma_m \left(1 - \frac{1}{i\omega_o} \frac{\partial}{\partial \tau} \right) |A_m(z; \tau)|^2 A_m(z; \tau) - \\ & i \frac{\bar{\beta}_m^{(2)}}{2} \frac{\partial^2 A_m(z; \tau)}{\partial \tau^2} - \bar{\alpha}_m^{(o)} A_m(z; \tau), \end{aligned} \quad (3.18)$$

where $\gamma_m = k_o \alpha_{mmmm}$ is the Kerr nonlinearity parameter and $\tau = t - \bar{\beta}_m^{(1)} z$ is the so-called retarded time. Here, we would like to emphasize that Eq. (3.18) is obtained in a rigorous way without any slowly-varying approximation and more general due to the analytic mode normalization in contrast to conventional formulations.

3.3 THE KERR NONLINEARITY PARAMETER

The definition of the Kerr nonlinearity parameter γ that we have obtained in the previous section within the single-mode approximation is general and fully vectorial. It can be readily applied to both bound [see Fig. 2.4 (a)] and leaky [see Fig. 2.4 (b)] modes due to the analytic mode normalization. In the case of leaky modes, the analytic mode normalization Eq. (2.59) provides the correct weight to the fields, thus, γ are complex quantities, in agreement with previous findings within the iterative [32, 33] and the perturbative approaches [16]. Particularly, our approach for the Kerr nonlinearity parameter γ is similar to that derived in Ref. [16]. However, authors in Ref. [16] use the standard normalization scheme based on the axial component of the Poynting vector [see Section 2.4.1] leading to an incorrect value of γ for leaky modes. In contrast, our approach with the correct mode normalization ensures a straightforward and efficient implementation in numerical calculations [A1].

Here, we discuss this new definition of the Kerr nonlinearity parameter γ in more details and compare it with previous perturbative approaches. First of all, let us briefly review the conventional approaches of the Kerr nonlinearity parameter that are widely used in the literature. Depending on the underlying approximation, we can divide these approaches in scalar and vectorial ones. The standard scalar approach is based on a weakly-guiding approximation and given by Agrawal [5]:

$$\gamma_{\text{Agrawal}} = \frac{n_2 k_0}{A_{\text{eff}}^{\text{Agrawal}}}, \quad (3.19)$$

with the effective mode area

$$A_{\text{eff}}^{\text{Agrawal}} = \frac{\left[\int_{-\infty}^{+\infty} |\mathbf{E}_{m,\parallel}(\mathbf{r}_{\parallel})|^2 d\mathbf{r}_{\parallel} \right]^2}{\int_{-\infty}^{+\infty} |\mathbf{E}_{m,\parallel}(\mathbf{r}_{\parallel})|^4 d\mathbf{r}_{\parallel}}. \quad (3.20)$$

Here, $\mathbf{E}_{m,\parallel} = (E_{m,x}, E_{m,y})$ denotes the transverse components of the electric field of the corresponding mode. The numerator in Eq. (3.20) is basically the squared scalar normalization constant introduced in Section 2.4.1 [see Eq. (2.48)]. The current definition of the Kerr nonlinearity parameter γ can be slightly improved by using the z -component of the real-valued Poynting vector $S_{m,z}$ instead of the transverse mode

fields \mathbf{E}_{\parallel} in the effective mode area [see Eq. (3.20)]. This has been suggested by Foster et al. [14]. Thus, we can write Foster's definition of the Kerr nonlinearity parameter as

$$\gamma_{\text{Foster}} = \frac{n_2 k_0}{A_{\text{eff}}^{\text{Foster}}}, \quad (3.21)$$

where

$$A_{\text{eff}}^{\text{Foster}} = \frac{\left[\int_{-\infty}^{+\infty} S_{m,z}(\mathbf{r}_{\parallel}) d\mathbf{r}_{\parallel} \right]^2}{\int_{-\infty}^{+\infty} [S_{m,z}(\mathbf{r}_{\parallel})]^2 d\mathbf{r}_{\parallel}}. \quad (3.22)$$

In this case, the numerator in Eq. (3.22) is the squared normalization constant based on the axial component of the Poynting vector introduced in Section 2.4.1 [see Eq. (2.49)].

Essentially, these definitions are scalar approaches since they do not take into account the axial component of the fields. The vectorial definition of the Kerr nonlinearity parameter γ is obtained from Afshar et al. [15]:

$$\gamma_{\text{Afshar}} = k_0 \frac{\int_{-\infty}^{+\infty} n^2(\mathbf{r}_{\parallel}) n_2(\mathbf{r}_{\parallel}) \left[2|\mathbf{E}_m(\mathbf{r}_{\parallel})|^4 + |\mathbf{E}_m^2(\mathbf{r}_{\parallel})|^2 \right] d\mathbf{r}_{\parallel}}{3 \left[\int_{-\infty}^{+\infty} S_{m,z}(\mathbf{r}_{\parallel}) d\mathbf{r}_{\parallel} \right]^2}. \quad (3.23)$$

In a similar fashion to the Foster's definition, this vectorial approach can be written as:

$$\gamma_{\text{Afshar}} = \frac{\tilde{n}_2 k_0}{A_{\text{eff}}^{\text{Foster}}}, \quad (3.24)$$

with a redefined nonlinear refractive index averaged over spatial inhomogeneities and weighted with respect to the fields [15]:

$$\tilde{n}_2 = \frac{\int_{-\infty}^{+\infty} n^2(\mathbf{r}_{\parallel}) n_2(\mathbf{r}_{\parallel}) \left[2|\mathbf{E}_m(\mathbf{r}_{\parallel})|^4 + |\mathbf{E}_m^2(\mathbf{r}_{\parallel})|^2 \right] d\mathbf{r}_{\parallel}}{3 \int_{-\infty}^{+\infty} [S_{m,z}(\mathbf{r}_{\parallel})]^2 d\mathbf{r}_{\parallel}}. \quad (3.25)$$

This vectorial definition provides more accurate results compared to the scalar approaches. However, it becomes less accurate or fails

completely in case of leaky modes. The reason is that the mode fields are still normalized with respect to the axial component of the time-averaged Poynting vector S_z over the entire cross section of the fiber. As we have discussed in Section 2.4.1, this normalization scheme diverges in the case of leaky modes, and hence, results in an unphysical value for the Kerr nonlinearity parameter. As we have shown in the example of the fundamental bound [see Fig. 2.6] and leaky [see Fig. 2.5] modes of the step-profile fiber, the analytical mode normalization Eq. (2.59) based on resonant state expansion does not depend on the area/radius of integration.

For the sake of completeness and convenience, we rewrite our approach for γ based on the resonant-state expansion in a similar form as previous scalar and vectorial approaches:

$$\gamma_{\text{RSE}} = k_o \int_0^{A_{\min}} n_2(\mathbf{r}_{\parallel}) \left\{ 2 \left[\mathbf{e}_m^{\text{R}}(\mathbf{r}_{\parallel}) \cdot \mathbf{e}_m(\mathbf{r}_{\parallel}) \right] \left[\mathbf{e}_m(\mathbf{r}_{\parallel}) \cdot \mathbf{e}_m^*(\mathbf{r}_{\parallel}) \right] + \left[\mathbf{e}_m^{\text{R}}(\mathbf{r}_{\parallel}) \cdot \mathbf{e}_m^*(\mathbf{r}_{\parallel}) \right] \left[\mathbf{e}_m(\mathbf{r}_{\parallel}) \cdot \mathbf{e}_m(\mathbf{r}_{\parallel}) \right] \right\} d\mathbf{r}_{\parallel}, \quad (3.26)$$

where A_{\min} denotes the minimum that includes all spatial inhomogeneities, i.e., the same area is used in the analytical normalization.

The effective mode area within our formulation of the Kerr nonlinearity parameter can be defined as follows:

$$A_{\text{eff}}^{\text{RSE}} = \left\{ \int_0^{A_{\min}} \left\{ 2 \left[\mathbf{e}_m^{\text{R}}(\mathbf{r}_{\parallel}) \cdot \mathbf{e}_m(\mathbf{r}_{\parallel}) \right] \left[\mathbf{e}_m(\mathbf{r}_{\parallel}) \cdot \mathbf{e}_m^*(\mathbf{r}_{\parallel}) \right] + \left[\mathbf{e}_m^{\text{R}}(\mathbf{r}_{\parallel}) \cdot \mathbf{e}_m^*(\mathbf{r}_{\parallel}) \right] \left[\mathbf{e}_m(\mathbf{r}_{\parallel}) \cdot \mathbf{e}_m(\mathbf{r}_{\parallel}) \right] \right\} d\mathbf{r}_{\parallel} \right\}^{-1}. \quad (3.27)$$

In this definition the effective mode area is in general a complex quantity. Note that the electric fields \mathbf{e}_m in Eq. (3.26) and Eq. (3.27) are already normalized according to Eq. (2.59).

As it has been mentioned at the beginning of Chapter 2, all equations in this dissertation are given in Gaussian units, consistent with our publications[A1–A3]. However, one can straightforwardly reformulate the equations in SI units by using the following changes: The permittivity ε and permeability μ have to be replaced by the relative ones, and one

needs to substitute the magnetic field \mathbf{H} with $Z_0\mathbf{H}^{\text{SI}}$, where Z_0 is the vacuum impedance, while the electric field \mathbf{E} simply becomes \mathbf{E}^{SI} . Next, for the conversion of the third-order electric susceptibility from Gaussian to SI units we can use $\chi_e^{(3)} = 4\pi/(3 \times 10^4)^2[\chi_e^{(3)}]^{\text{SI}}$ [69]. In order to allow for an easier comparison with experimental results, we present our simulation results in the following sections and chapters in SI units.

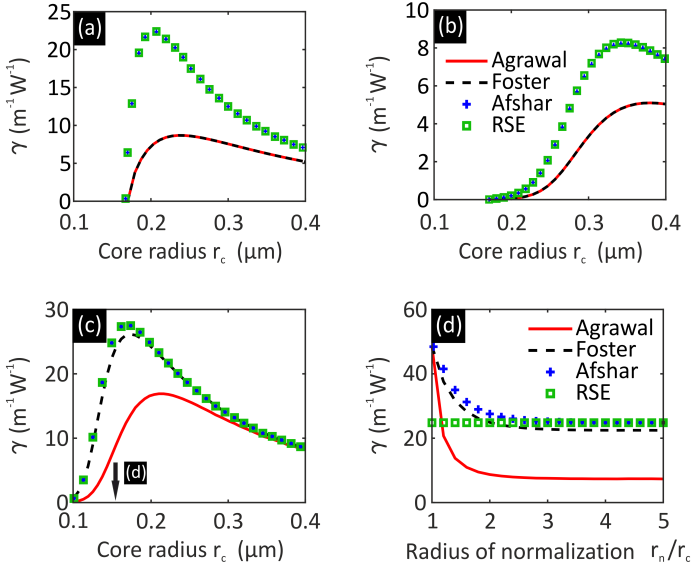


Figure 3.1. Comparison of different perturbative approaches for calculating the Kerr nonlinearity parameter γ of different modes of a cylindrical step-index fiber with bismuth oxide (Bi_2O_3) doped glass core with refractive index of $n = 2.05$ in air with $n = 1$ at $\lambda_0 = 800 \text{ nm}$: γ of the first transverse electric (TE_{01}) (a), the transverse magnetic (TM_{01}) (b), and the fundamental (HE_{11}) (c) bound modes as a function of core radius r_c for a radius of normalization $r_n = 5r_c$; (c) dependence of γ of the fundamental bound mode on r_n for $r_c = 0.15 \mu\text{m}$, indicated by the arrow in (c).

Let us now compare our approach for the calculation of the Kerr nonlinearity parameter γ with other perturbative formulations in case of bound modes. Since bound modes exhibit a real propagation constant, reciprocal conjugation can be replaced by usual complex conjugation,

i.e., $\mathbf{E}_m^R = \mathbf{E}_m^*$. Hence, one can show that our γ has exactly the same form as in the vectorial approach Eq. (3.23) described in Refs. [15, 16, 57], whereas the scalar approaches of Refs. [5, 14] are approximately valid. Panels (a) and (b) in Fig. 3.1 display the Kerr nonlinearity parameter γ of the first transverse electric (TE₀₁) and transverse magnetic (TM₀₁) bound modes of a cylindrical step-profile fiber with bismuth oxide Bi₂O₃ doped glass [$n_2 = 3.2 \times 10^{-19} \text{ m}^2 \text{ W}^{-1}$] core surrounded by air [$n_2 = 5.7 \times 10^{-23} \text{ m}^2 \text{ W}^{-1}$] as a function of core radius r_c , respectively. The results have been obtained by the weakly guiding approximation [Agrawal, red line, Eq. (3.19)], its slightly improved version suggested in [Foster, black dashed line, Eq. (3.21)], the fully vectorial approach [Afshar, blue crosses, Eq. (3.23)], and our approach based on the resonant-state expansion [RSE, green square dots, Eq. (3.26)]. It can be seen that our approach provides exactly the same results as the fully vectorial one. In contrast, both scalar approaches (Agrawal, Foster) deviate significantly for small core radii since they do not take into account the inhomogeneity of the waveguide structure i.e., $n(\mathbf{r}_{\parallel})$ and $n_2(\mathbf{r}_{\parallel})$ completely as well as the vectorial nature of electromagnetic fields [15]. However, in this case, these scalar approaches give the same results, which is due to the absence of the longitudinal component of the fields of TE ($E_{m,z} = 0$) and TM ($H_{m,z} = 0$) modes [28]. Indeed, Eq. (3.22) can be written as [15]

$$A_{\text{eff}}^{\text{Foster}} = \frac{\left\{ \int_{-\infty}^{+\infty} \left[\beta_m |\mathbf{E}_{m,\parallel}|^2 + i \mathbf{E}_{m,\parallel} \cdot \nabla_{\parallel} E_{m,z} \right] d\mathbf{r}_{\parallel} \right\}^2}{\int_{-\infty}^{+\infty} \left[\beta_m |\mathbf{E}_{m,\parallel}|^2 + i \mathbf{E}_{m,\parallel} \cdot \nabla_{\parallel} E_{m,z} \right]^2 d\mathbf{r}_{\parallel}}. \quad (3.28)$$

As we can see, in the case of transverse modes it simplifies to Eq. (3.20). In Fig. 3.1 (c), we show the same calculations for the fundamental (HE₁₁) bound mode of the step-profile fiber. In this case, both fully vectorial approaches (RSE and Afshar) provide the same result again as expected while the scalar approaches are still less accurate in subwavelength regime, i.e. $2r_c < \lambda_0$. One can note that for large core radii ($2r_c \gg \lambda_0$), all approaches provide similar results since the fields are almost concentrated in the core region and the in-plane components of the fields become dominating.

The advantage of our approach compared to the fully vectorial one is that in numerical calculations, we can restrict the area of normalization to the regions of spatial inhomogeneities, which is in the present waveguide geometry the fiber core. This can be seen in Fig. 3.1 (d), where γ

is displayed as a function of the radius of normalization r_n for a fixed core radius of $r_c = 1.5 \mu\text{m}$. While previous approaches [5, 14, 15] require some finite radius r_n of roughly $3r_c$ in order to exhibit a deviation of less than 5% of their exact value of normalization for $r_n \rightarrow \infty$, our approach is independent of the radius of normalization for all $r_n > r_c$, as expected from Eq. (2.59) and shown in Fig. 2.6. This fact makes numerical calculations more efficient, especially for complex fiber geometries such as photonic crystal fibers [70] and situations with extended evanescent fields.

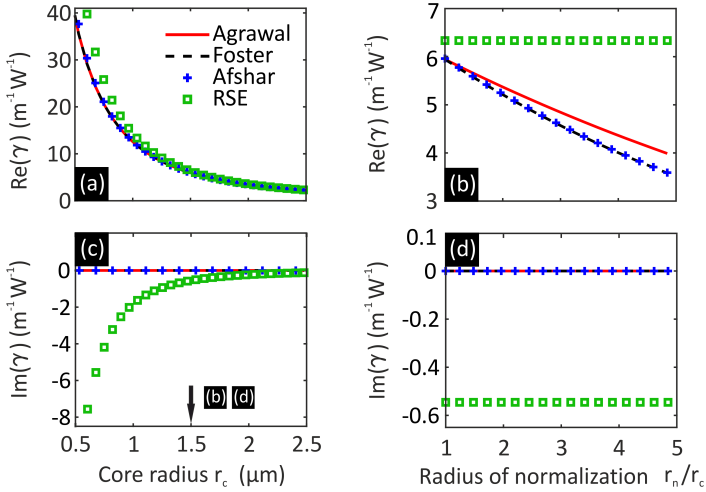


Figure 3.2. Comparison of different approaches for calculating γ of the fundamental (HE_{11}) leaky mode in a bismuth oxide Bi_2O_3 glass capillary filled with carbon disulfide CS_2 with $n = 1.6$ at $\lambda_o = 800 \text{ nm}$. The real (a) and the imaginary part (c) of γ as a function of core radius r_c for a radius of normalization $r_n = r_c$. Their dependence on radius of normalization r_n for $r_c = 1.5 \mu\text{m}$ which is indicated by the arrow in (c) is shown in panels (b) and (d), respectively.

Let us address leaky modes, for which most existing approaches cannot be used in a straightforward manner. As a rather simple example for leaky modes, we consider a Bi_2O_3 capillary fiber that has been used in different experiments [63, 71]. In our case, the capillary is filled with carbon disulfide CS_2 [$n_2 = 2.7 \times 10^{-18} \text{ m}^2 \text{ W}^{-1}$] [64, 72–74], which we assume here to be the only nonlinear material, since its nonlinear re-

fractive index is much higher than Bi_2O_3 doped glass. The dependence of the real and imaginary parts of the Kerr nonlinearity parameter γ on core radius r_c is shown in Fig. 3.2 (a) and (b), respectively. In the strong guidance or subwavelength regime ($2r_c < \lambda_o$), the scalar and the fully vectorial approach begin to deviate from our value for the real part of γ [Fig. 3.2 (a)]. As in the case of the bound modes, for large core radii ($2r_c \gg \lambda_o$), the deviation between the different approaches becomes smaller. Here, we have used $r_n = r_c$ as an optimum radius of normalization for each core radius, which corresponds to the minimum deviation between the real parts of γ of conventional formulations to our approach. Essentially, this optimal normalization radius is the position of the radiation caustic r_{rad} , i.e., $r_n = r_{\text{rad}}$ [28]. The normalization scheme based on the radiation caustic is discussed in Section 2.4.1.

The dependence of the real and imaginary parts of the Kerr nonlinearity parameter γ for the fundamental leaky mode on the normalization radius r_n is shown in Fig. 3.2 (b) and Fig. 3.2 (d), respectively, for a fixed core radius of $r_c = 1.5 \mu\text{m}$. As we can see, our approach yields the same γ for all radii of normalization, while the other approaches result in $\gamma \rightarrow 0$ for $r_n \rightarrow \infty$ due to incorrect normalization of the mode.

It is also interesting to consider the Kerr nonlinearity γ of the transverse electric (TE) and the transverse magnetic (TM) leaky modes of the capillary fiber since the mode with the lowest attenuation constant is not always the fundamental (HE_{11}) one. This becomes important in designing a high-power pulse compression systems based on the hollow-core fibers [21, 75, 76]. Indeed, as it has been shown in Ref. [58], the real $\tilde{\beta}_m$ and the imaginary $\tilde{\alpha}_m$ parts of the propagation constant β_m [zeros of the determinant of the 4×4 matrix in Eq. (2.70)] in case of $\kappa_m r_c \gg 1$ can be approximated as

$$\tilde{\beta}_{mn} = k_o \left[1 - \frac{1}{2} \left(\frac{u_{mn}}{k_o r_c} \right)^2 \right], \quad (3.29)$$

and

$$\tilde{\alpha}_{mn} = \frac{u_{mn}^2}{k_o^2 r_c^3} \begin{cases} \frac{1}{(n_r^2 - 1)^{1/2}} & \text{for TE}_{on} \text{ modes } (m = 0), \\ \frac{n_r^2}{(n_r^2 - 1)^{1/2}} & \text{for TM}_{on} \text{ modes } (m = 0), \\ \frac{1}{2} \frac{n_r^2 + 1}{(n_r^2 - 1)^{1/2}} & \text{for HE}_{mn}/\text{EH}_{mn} \text{ modes } (m \neq 0), \end{cases} \quad (3.30)$$

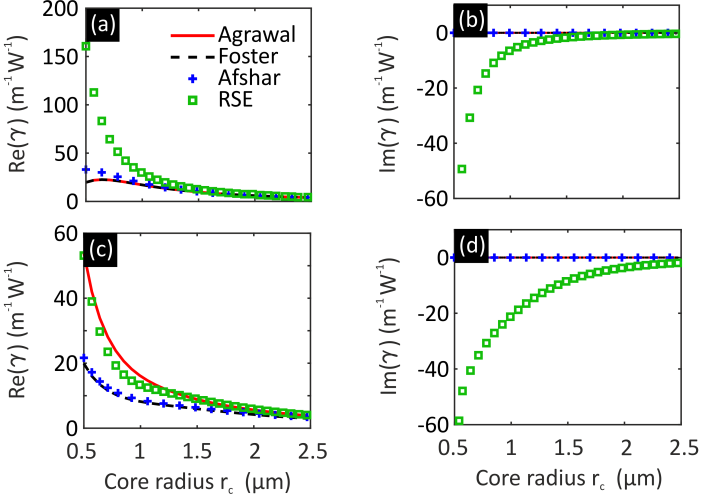


Figure 3.3. Comparison of different approaches for calculating γ of the first transverse electric TE_{01} (a), (b) and TM_{01} (c), (d) leaky modes in a silicon (Si) capillary with refractive index of $n = 3.45$ filled with nitrobenzene $\text{C}_6\text{H}_5\text{NO}_2$ with $n = 1.52$ at $\lambda_0 = 800$ nm. The real (a), (c) and the imaginary parts (b), (d) of γ of the leaky modes as a function of core radius r_c , respectively.

where u_{mn} is the m th root of the Bessel function $J_{n-1}(x)$ and $n_r = n_{\text{cl}}/n_{\text{co}}$. From Eq. (3.30), we find that the mode with the lowest modal loss is the first transverse electric TE_{01} leaky mode if $n_r > 2.02$ [58]. In order to fulfil this condition, we consider a capillary made of silicon (Si) with the linear and nonlinear refractive indices of $n_{\text{cl}} = 3.45$ and $[n_2 = 2.6 \times 10^{-18} \text{ m}^2 \text{ W}^{-1}]$ [77] and filled with nitrobenzene ($\text{C}_6\text{H}_5\text{NO}_2$) with $n_{\text{co}} = 1.52$ and $[n_2 = 6.9 \times 10^{-18} \text{ m}^2 \text{ W}^{-1}]$ [72, 73, 78]. The panels (a) and (b) in Fig. 3.3 display the real and the imaginary parts of γ of TE_{01} and TM_{01} leaky modes as a function of the core radius r_c of the capillary, respectively. As we can see, for a smaller core radius, in our approach the Kerr nonlinearity parameter γ of TE_{01} leaky mode is much larger than γ of TM_{01} . In the opposite direction, i.e., for $2r_c \gg \lambda_0$ the deviation between them becomes smaller as well as the deviation between different approaches. However, the imaginary part of γ of TE_{01} leaky mode tends to zero much faster than the imaginary part of γ of

TM_{01} . This can be useful to design a waveguide with certain nonlinear properties.

As we have shown in Figs. 3.2 and 3.3, for sufficiently large capillary radii relative to the wavelength, the deviation between the conventional perturbative approaches and our definition for γ becomes smaller. This can be correlated to the fact that the attenuation constant of modes of capillary fibers with radii much larger than the wavelength is $\bar{\alpha}_m \propto \lambda_0^2/r_c^3$ [see Eq. (3.30)] [58]. On the other hand, according to panels (b) and (d) of Fig. 3.2, the deviation between different approaches depends on the radius of normalization. However, it was only for one fixed core radius [indicated by black arrow in Fig. 3.2 (c)]. In order to show it for a wide range of the core radii, we have repeated those calculations and then found a difference between two vectorial approaches. In Fig. 3.4, we display the minimum deviation of the real part of γ (red solid line) and its absolute value (blue dashed line) between the approach by Afshar [see Eq. (3.23)] and our definition [see Eq. (3.26)] as a function of core radius r_c . As we can see, the minimum relative difference is quite big for the subwavelength region, although decreases rapidly over the core radius. Evidently, the imaginary part of γ_{RSE} is the main reason for the significant deviation for larger core radii.

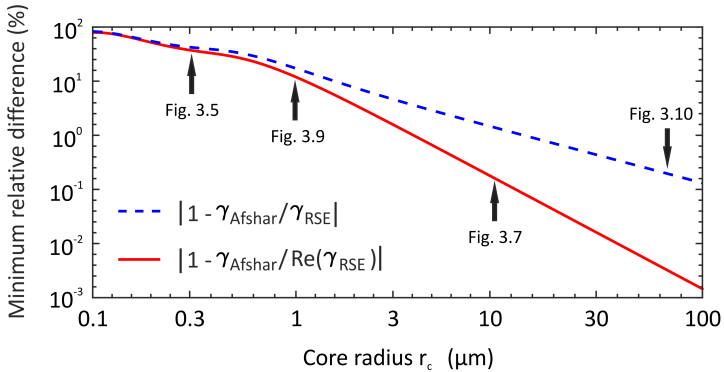


Figure 3.4. Minimum relative differences between the vectorial γ_{Afshar} and our γ_{RSE} (blue dashed line) as well as $\text{Re}(\gamma_{\text{RSE}})$ (red solid line) as a function of the core radius for the Bi_2O_3 doped glass capillary filled with carbon disulfide CS_2 at $\lambda_0 = 800$ nm.

3.4 NONLINEAR GAIN AND LOSS

As we have seen in the previous section, in contrast to bound modes and the other perturbative approaches that we have considered, our definition for the Kerr nonlinearity parameter γ_{RSE} [see Eq. (3.26)] provides a nonvanishing imaginary part in case of leaky modes. In this section, we discuss this imaginary part of γ and give a physical explanation.

As a matter of fact, it is already known from previous works [16, 32, 33] that the Kerr nonlinearity parameter can have an imaginary part. In these works authors have predicted the Kerr nonlinearity parameter γ with a positive imaginary part that corresponds to the additional nonlinear loss in addition to the modal loss $\tilde{\alpha}_m^{(0)}$. Indeed, if we approximate Eq. (3.18) as

$$\frac{\partial A_m(z; \tau)}{\partial z} \approx -[\tilde{\alpha}_m^{(0)} + \text{Im}(\gamma)P]A_m(z; \tau), \quad (3.31)$$

that has a solution

$$A_m(z; \tau) = e^{-[\tilde{\alpha}_m^{(0)} + \text{Im}(\gamma)P]z}, \quad (3.32)$$

where $P = |A_m(z; \tau)|^2$ is the initial pulse power. It is clear that in case of $\text{Im}(\gamma) > 0$ the field envelope A_m decays in a shorter propagation distance than only with the modal loss. However, we find that, depending on the fiber parameters, $\text{Im}(\gamma)$ can change its sign [A2]. In order to demonstrate this numerically, we consider the fundamental leaky mode in a capillary fiber of radius $r_c = 0.3 \mu\text{m}$ with a bismuth oxide Bi_2O_3 doped glass cladding ($n = 2.05$) and a varying refractive index in the core at a wavelength of $\lambda_0 = 800 \text{ nm}$. As we can see in Fig. 3.5 (c) the imaginary part of γ_{RSE} can change sign. Interestingly, it occurs around the refractive index of the core medium at $n \approx 1.9$ that is close to the minimum of the effective refractive index n_{eff} . It should be noted that such a behavior can be expected from iterative approaches for the calculation of the Kerr nonlinearity parameter γ [32, 33], which should yield a sign change of the imaginary part exactly at the minimum of the iteratively derived linear attenuation, while the homogeneous change of the refractive index in the core can be understood as a simplistic binary version of the first iteration.

The imaginary part of the Kerr nonlinearity parameter with a negative sign corresponds to the nonlinear gain. From the mathematical point of view, this can be easily seen from Eq. (3.32) by reversing the sign

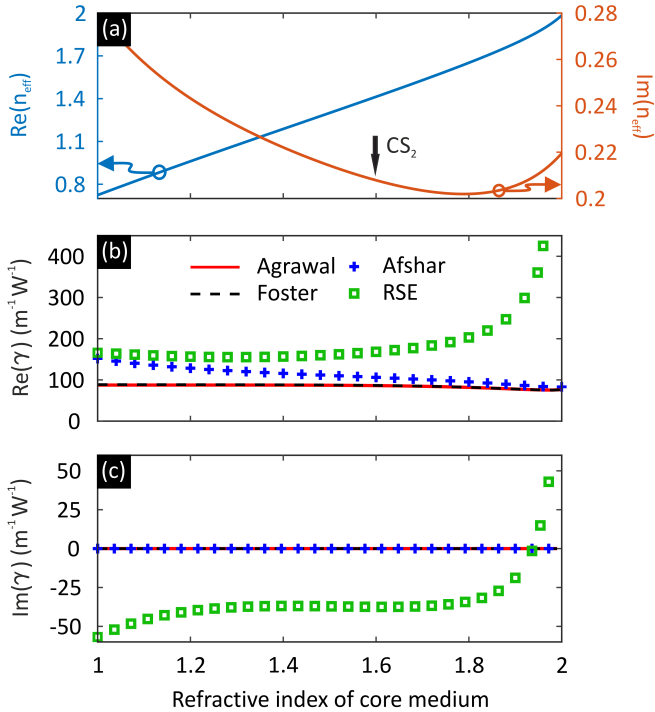


Figure 3.5. Numerical results of the fundamental leaky mode in a capillary fiber of radius $r_c = 0.3 \mu\text{m}$ with a Bi_2O_3 cladding ($n = 2.05$) and a varying refractive index in the core at a wavelength of $\lambda_o = 800 \text{ nm}$: **(a)** effective refractive index (n_{eff}), **(b)** real and **(c)** imaginary parts of the Kerr nonlinearity parameter γ . Red solid and black dashed lines have been calculated using the scalar approximations of Agrawal [Eq. (3.19)] [5] and Foster [Eq. (3.21)] [14], respectively, whereas blue crosses have been obtained by the vectorial approach of Afshar [Eq. (3.23)] [15]. The green squares have been calculated by our approach [Eq. (3.26)] [A2], which yields a nonvanishing imaginary part of γ . It can be seen in (c) that this imaginary part can change sign, i.e., can exhibit nonlinear loss and even nonlinear gain. The latter can be explained by a self-focusing of the nonlinear pulse [see Fig. 3.6], which reduces the pulse intensity at the interface to the cladding, which in turn decreases the amount of light that is transversely transmitted into the cladding and is radiating to the far field.

of $\text{Im}(\gamma)$. In this case constant modal loss $\tilde{\alpha}_m^{(o)}$ is decreased by $\text{Im}(\gamma)P$. Here, it seems that for high enough initial pulse power P nonlinear gain can dominate over the constant modal loss $\tilde{\alpha}_m^{(o)}$ so that $\text{Im}(\gamma)P > \tilde{\alpha}_m^{(o)}$. It means, that the field envelope A_m grows exponentially. This contradicts to the energy conservation law. Indeed, for pulses with such power, it is necessary to take into account higher order loss terms and probably other nonlinear effects such as filamentation and ionization of the medium [79].

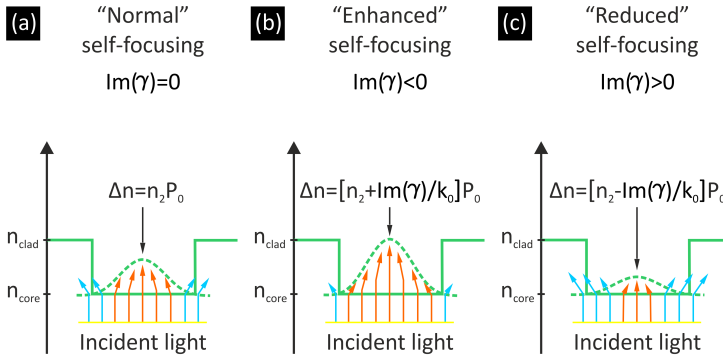


Figure 3.6. A physical interpretation of the nonlinear gain and loss. The interpretation is based on self-focusing that arises due to the optical Kerr effect. (a) "Normal" self-focusing corresponding to $\text{Im}(\gamma) = 0$ is chosen as a reference. (b) The negative imaginary part of γ enhances (with respect to the reference) the self-focusing in the core region and reduces the intensity near the core/cladding interface. This decreases the energy dissipation through the cladding that can be considered as a nonlinear gain. (c) The positive imaginary part of γ makes the self-focusing weaker (with respect to the reference) that increases the energy dissipation through the cladding and can be considered as a nonlinear loss.

The physical mechanism of the nonlinear gain and loss can be explained by a self-focusing [A2]. First of all, following Ref. [15], let us introduce the effective nonlinear refractive index $\tilde{n}_2 = n_2 - \text{Im}(\gamma)/k_0$ that depends on the waveguide geometry and field distributions. Now, imagine the case in which the imaginary part of the Kerr nonlinearity parameter is $\text{Im}(\gamma) = 0$. Due to the optical Kerr effect ($\Delta n = \tilde{n}_2 P$), the

actual refractive index at the center of the step-profile hollow-core fiber is higher than the near sides [see Fig. 3.6 (a)]. Therefore, the local total internal reflection takes place and as a direct consequence self-focusing of a light occurs. Let us call it the "normal" self-focusing case. Now, let the imaginary part of the Kerr nonlinearity parameter be $\text{Im}(\gamma) < 0$. In this case, the refractive index increment Δn is larger than the "normal" self-focusing case. This leads to a stronger local light confinement in the core region that reduces the intensity at the core/cladding interface [see Fig. 3.6 (b)], which in turn decreases the energy dissipation through the cladding. We can consider this reduction in energy dissipation as a nonlinear gain. In case of $\text{Im}(\gamma) > 0$, the effective nonlinear refractive index \tilde{n}_2 is decreased [see Fig. 3.6 (c)]. Accordingly, the central reduction in the refractive index lets more light escape the core. Hence, this in turn can be interpreted as nonlinear loss.

3.5 THE NONLINEAR GAIN AND PULSE PROPAGATION

In the previous sections, we have obtained the nonlinear Schroedinger equation [see Eq. (3.18)] with the new definition the Kerr nonlinearity parameter [see Eq. (3.26)] that can be applied to bound and leaky modes. Furthermore, we found that the Kerr nonlinearity parameter can have a negative imaginary part for leaky modes. This negative imaginary part of the Kerr nonlinearity parameter can be considered as a nonlinear gain. As a next step, we study the impact of this nonlinear gain on the pulse propagation.

For our numerical simulations, as a simple example, we consider the Bi_2O_3 ($n = 2.05$) capillary fiber with a radius of $r_c = 10 \mu\text{m}$ filled with CS_2 ($n = 1.6$). The numerical solution of Eq. (3.18) is calculated using the well-known split-step Fourier method [5]. Here, we use an enhanced version of the method that the nonlinear part of Eq. (3.18) is integrated by a fourth-order Runge-Kutta method [80–82]. The initial pulse used in our simulations has

$$A_m(z = 0; \tau) = P_o^{1/2} \text{sech}\left(\frac{\tau}{T_o}\right), \quad (3.33)$$

field profile with peak power $P_o = 15 \text{ kW}$ and full width at half-maximum $T_{\text{FWHM}} = 1.763 T_o = 140 \text{ fs}$. Since the initial pulse width is quite narrow, in Eq. (3.18), we consider the dispersion terms up to $\beta^{(4)}$.

The panels (c) and (d) of Fig. 3.7 display the spectral and temporal evolution of the fundamental leaky mode of the capillary fiber, respec-

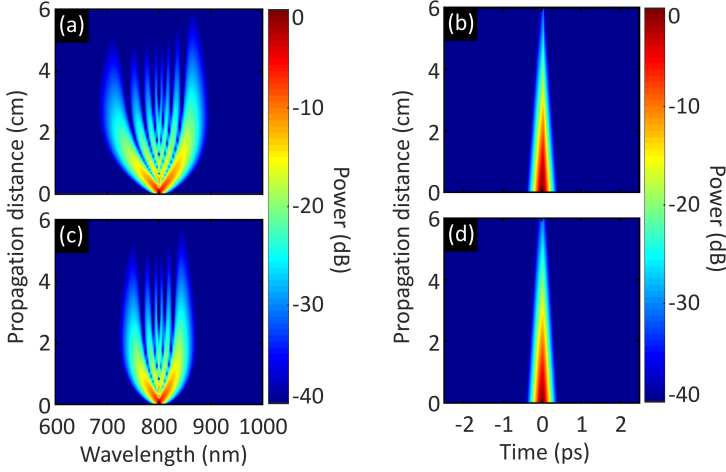


Figure 3.7. Numerical simulation showing the nonlinear pulse propagation inside a CS_2 -filled Bi_2O_3 doped glass capillary ($r_c = 10 \mu\text{m}$) with $\gamma_{\text{RSE}} = (141.7 - 1.9i) \text{ km}^{-1}\text{W}^{-1}$ [panels (a) and (b)] and $\gamma_{\text{Afshar}} = 141.5 \text{ km}^{-1}\text{W}^{-1}$ [panels (c) and (d)]. The input hyperbolic secant shape pulse at $\lambda_o = 800 \text{ nm}$ has $P_o = 15 \text{ kW}$ peak power and the full width at half-maximum of $T_{\text{FWHM}} = 140 \text{ fs}$. Calculated dispersion parameters of the fiber are $\tilde{\beta}^{(2)} = -0.82 \text{ ps}^2\text{km}^{-1}$, $\tilde{\beta}^{(3)} = 1.05 \times 10^{-3} \text{ ps}^3\text{km}^{-1}$, $\tilde{\beta}^{(4)} = -1.78 \times 10^{-6} \text{ ps}^4\text{km}^{-1}$, with an attenuation coefficient of $\tilde{\alpha}^{(o)} = 60.15 \text{ m}^{-1}$.

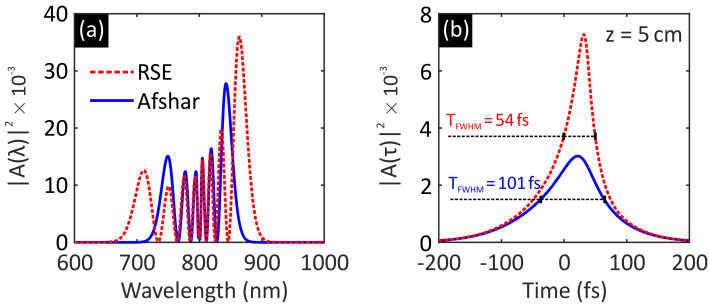


Figure 3.8. Comparison of the numerical simulation showed in Fig. 3.7 for the nonlinear pulse propagation in the capillary fiber at the propagation distance $z = 5 \text{ cm}$.

tively, obtained by solving Eq. (3.18) with $\gamma_{\text{Afsnar}} = 141.5 \text{ km}^{-1}\text{W}^{-1}$. The results in Fig. 3.7 (a) and Fig. 3.7 (b) have been obtained for $\gamma_{\text{RSE}} = (141.7 - 1.9i) \text{ km}^{-1}\text{W}^{-1}$ based on our approach. In the latter case [see Fig. 3.7 (a)], we can clearly see an increasing spectral broadening (also known as supercontinuum generation [82, 83]) compared to the fully vectorial approach [Fig. 3.7 (c)] that is accompanied by a narrowing in the corresponding temporal evolutions [Fig. 3.7 (b) and Fig. 3.7 (d)].

This can be seen more clearly in Fig. 3.8 that shows the comparison of simulation results (spectral and temporal evolutions) for two approaches at the propagation distance of $z = 5 \text{ cm}$. In our case, the full width at half maximum (FWHM) is roughly 2 times shorter than the case of the full vectorial approach. Here, the pulse asymmetry of shape is caused by the phenomenon of self-steepening [5]. This means that the negative imaginary part of the Kerr nonlinearity parameter leads to pulse compression, which in turn gives rise to spectral broadening.

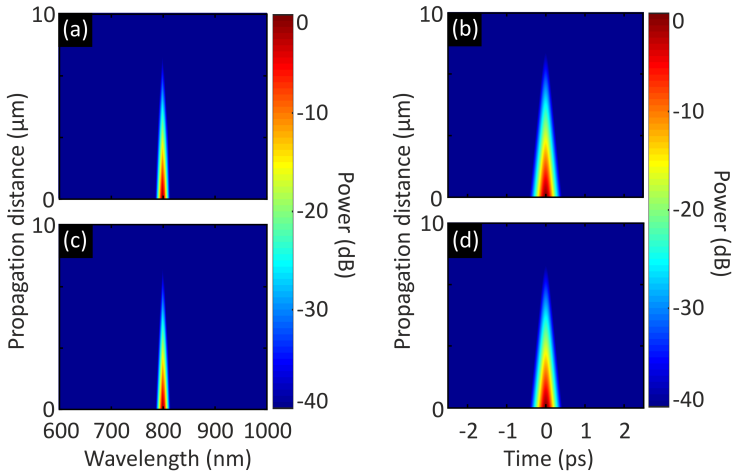


Figure 3.9. Numerical simulation showing the nonlinear pulse propagation inside a CS_2 -filled Bi_2O_3 doped glass capillary ($r_c = 1 \mu\text{m}$) with $\gamma_{\text{RSE}} = (14.37 - 1.81i) \text{ m}^{-1}\text{W}^{-1}$ [panels (a) and (b)] and $\gamma_{\text{Afsnar}} = 12.65 \text{ m}^{-1}\text{W}^{-1}$ [panels (c) and (d)]. The input hyperbolic secant shape pulse at $\lambda_o = 800 \text{ nm}$ has $P_o = 15 \text{ kW}$ peak power and the full width at half-maximum of $T_{\text{FWHM}} = 140 \text{ fs}$. Calculated dispersion parameters of the fiber are $\tilde{\beta}^{(2)} = -60.18 \text{ ps}^2\text{km}^{-1}$, $\tilde{\beta}^{(3)} = 5.87 \times 10^{-2} \text{ ps}^3\text{km}^{-1}$, $\tilde{\beta}^{(4)} = -5.22 \times 10^{-5} \text{ ps}^4\text{km}^{-1}$, with an attenuation coefficient of $\tilde{\alpha}^{(0)} = 59.11 \text{ mm}^{-1}$.

As we have discussed in the previous section, the imaginary part of the Kerr nonlinearity parameter γ_{RSE} acts as a nonlinear gain. This means that the initial pulse in simulations with γ_{RSE} should decay slower than with real γ_{Afshar} , which has been demonstrated in the above numerical simulations. Let us repeat the simulations for a smaller core radius that has an even higher imaginary part of the γ_{RSE} [see Fig. 3.2 (c)]. For that, we consider the same fiber with $r_c = 1 \mu\text{m}$. In this case, for the fundamental leaky mode, we obtain $\gamma_{\text{RSE}} = (14.37 - 1.81i) \text{ m}^{-1}\text{W}^{-1}$ and $\gamma_{\text{Afshar}} = 12.65 \text{ m}^{-1}\text{W}^{-1}$. As we can see in Fig. 3.9, in both cases, the results are quite similar with the initial pulse decaying rapidly because of the extremely high modal loss. It indicates that the fiber losses still dominate and the energy conservation is not violated despite that γ_{RSE} is now several orders higher than the previous case.

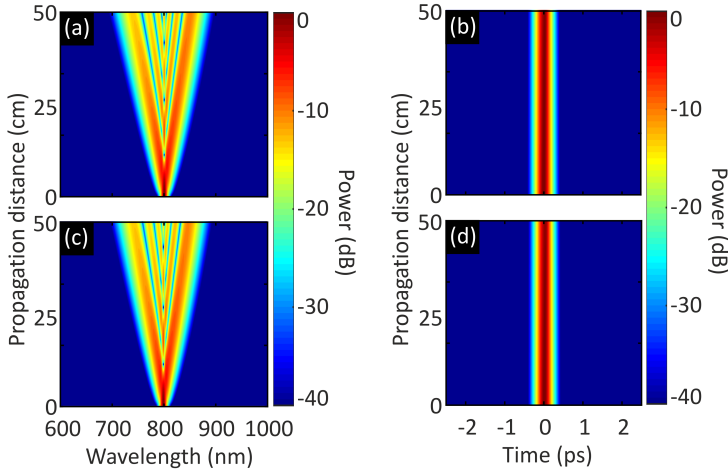


Figure 3.10. Numerical simulation showing the nonlinear pulse propagation inside a CS_2 -filled Bi_2O_3 doped glass capillary ($r_c = 70 \mu\text{m}$) with $\gamma_{\text{RSE}} = (2.28 - 5.43 \times 10^{-3}i) \text{ km}^{-1}\text{W}^{-1}$ [panels (a) and (b)] and $\gamma_{\text{Afshar}} = 2.28 \text{ km}^{-1}\text{W}^{-1}$ [panels (c) and (d)]. The input hyperbolic secant shape pulse at $\lambda_o = 800 \text{ nm}$ has $P_o = 15 \text{ kW}$ peak power and the full width at half-maximum of $T_{\text{FWHM}} = 140 \text{ fs}$. Calculated dispersion parameters of the fiber are $\tilde{\beta}^{(2)} = -1.68 \times 10^{-2} \text{ ps}^2\text{km}^{-1}$, $\tilde{\beta}^{(3)} = 2.28 \times 10^{-5} \text{ ps}^3\text{km}^{-1}$, $\tilde{\beta}^{(4)} = -3.55 \times 10^{-8} \text{ ps}^4\text{km}^{-1}$, with an attenuation coefficient of $\tilde{\alpha}^{(0)} = 0.17 \text{ m}^{-1}$.

For the completeness, consider the opposite case, i.e., the capillary with radius of $r_c = 70 \mu\text{m}$. In this case, the simulation results are shown

in Fig. 3.10 and the corresponding Kerr nonlinearity parameters are $\gamma_{\text{RSE}} = (2.28 - 5.43 \times 10^{-3}i) \text{ km}^{-1}\text{W}^{-1}$ [panels (c) and (d)] and $\gamma_{\text{Afshar}} = 2.28 \text{ km}^{-1}\text{W}^{-1}$ [panels (a) and (b)]. Since in both cases the real part of γ is the same and the imaginary part of γ_{RSE} is too small in comparison to the real part, there is almost no difference between the top and bottom panels.

Thus, we have presented here a new rigorous formulation for simulating nonlinear pulse propagation in waveguides and optical fibers based on the resonant-state expansion with analytic mode normalization. Most importantly, we find that, in the case of leaky modes, the Kerr nonlinearity parameter has an imaginary part that provides either nonlinear loss or nonlinear gain for overall attenuating pulses. We demonstrated here on the example of liquid-filled capillary-type fibers that this imaginary part can significantly influence the spectral and temporal evolution of an ultrashort pulse.

~

This chapter is based on the following publication [A3]:

I. Allayarov, S. Upendar, M. A. Schmidt, and T. Weiss: "*Theory of four-wave mixing for bound and leaky modes*", Phys. Rev. A, **101** 043806 (2020).

DOI 10.1103/physreva.101.043806

In the previous chapter, we have derived a master equation for the nonlinear pulse propagation that allows for a rigorous description of both bound and leaky modes in waveguide geometries. There, we showed that in the single-mode approximation, it simplifies to the standard nonlinear Schroedinger equation for bound and leaky modes. This approximation is widely used for description of supercontinuum generation. However, in order to describe a parametric processes such as four-wave mixing, the single-mode approximation has to be extended by taking into account the coupling between different modes at a certain wavelength or coupling of modes with different wavelengths.

Four-wave mixing is one of the interesting nonlinear phenomena that occurs in optical fibers due to the third-order nonlinear polarization [5]. It has been studied extensively over the last several decades [84–89]. Traditionally, four-wave mixing is used to generate waves at certain frequencies or amplify a pre-existing weak signal [90, 91]. However, it is a highly undesired effect for applications such as in optical fiber communications where it leads to interchannel crosstalk [92, 93]. At the same time, four-wave mixing is one of the main nonlinear mechanisms for supercontinuum generation in optical fibers in combination with self-phase and cross-phase modulations [5].

From the quantum physics point of view, the process of four-wave mixing relates to the annihilation of two incident (pump) photons at different frequencies and the simultaneous creation of two photons at new frequencies, while the laws of conservation of energy and momentum have to be fulfilled [see lower left inset of Fig. 4.1 (a)]. Historically, the photons at new frequencies are either called Stokes (at lower frequency) or anti-Stokes (at higher frequency) photons. In this context, the pro-

cess of annihilation of two photons at the same frequency is known as degenerate four-wave mixing. In optical fibers, four-wave mixing originates from the Kerr-type nonlinearity. Efficient four-wave mixing can only occur if there is no phase mismatch between pump, Stokes, and anti-Stokes waves. Therefore, observation and realization of four-wave mixing at desired frequencies requires dispersion-engineered waveguides with specific parameters.

In this chapter, we present a comprehensive theory of four-wave mixing in waveguide geometries, providing a rigorous description of the dynamics of both bound as well as leaky modes within a single theoretical framework. For that, we extend our new theory of the nonlinear pulse propagation to four-wave mixing, requiring to consider the coupling of excitations of several frequencies inside a single fiber. We show that for bound modes, our theory agrees with the scalar and vectorial theories reported in literature [5, 15]. In the case of leaky modes, it results in a modified nonlinear pulse propagation, predicting a more efficient generation of Stokes and anti-Stokes bands than expected from the previous theory for bound modes. Furthermore, we show that the modulation instability can occur for all frequencies in both anomalous and normal dispersion regions.

In order to demonstrate these effects numerically, as a generic example of a hollow-core fiber geometry, we consider a gas-filled hollow-core annulus fiber geometry consisting of a single glass ring embedded in an otherwise low index medium [geometry depicted in the upper right inset of Fig. 4.1(a)]. As we can see in Fig. 4.1 (b) and (c), it supports core leaky modes. Moreover, as shown in Ref. [96], this fiber geometry allows an accurate resemblance of the dispersion parameter of various kinds of hollow-core fibers and in particular, antiresonant fibers, making it a useful model system to study nonlinear pulse propagation in dissipative waveguide geometries.

4.1 BOUND-MODE THEORY

Four-wave mixing in conventional silica fibers that carry bound modes, usually is described within a scalar theory [5]. In this approach, the electric field of the involved waves in four-wave mixing is assumed to be

$$\mathbf{E}_j(\mathbf{r}, t) = A_j(z, t) \mathbf{E}_{j,\parallel}(\mathbf{r}_{\parallel}) e^{i\hat{\beta}_j^{(0)} z}. \quad (4.1)$$

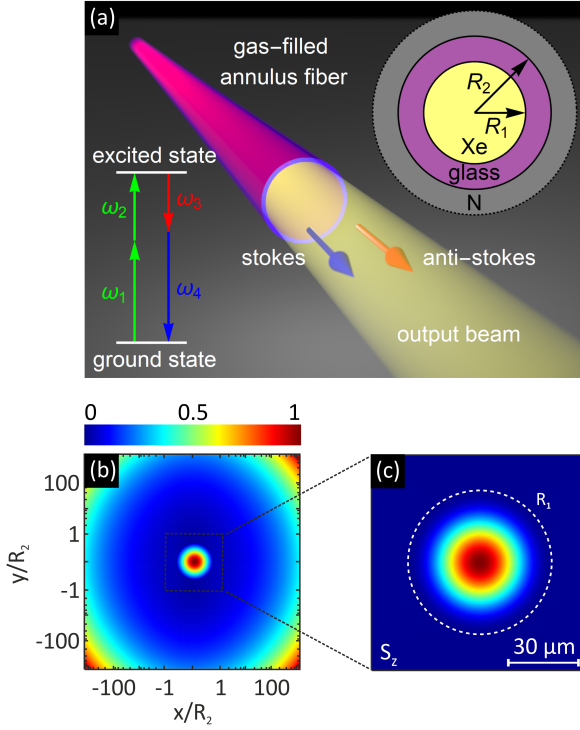


Figure 4.1. (a) Cross section and schematics of an annulus fiber made from silica (SiO_2) and filled by xenon (Xe) in nitrogen (N) surrounding. The low left inset shows energy-level diagram for four-wave mixing occurring due to the annihilation of two photons at frequencies ω_1 and ω_2 with creation of two new photons at frequencies ω_3 and ω_4 . (b) Spatial distribution of the axial component of the real-valued Poynting vector of the fundamental leaky mode of the annulus waveguide geometry shown in (a). Outside the core region, a logarithmic scale is used for the distance to the fiber core. The white dashed line in (c) indicates the inner radius of the fiber. The refractive indices of silica and gases are taken from Refs. [94, 95]. The inner and outer radii of the annulus waveguide are $R_1 = 30 \mu\text{m}$ and $R_2 = 30.476 \mu\text{m}$, respectively. The fundamental leaky mode of the fiber is calculated at the wavelength of $\lambda = 470 \text{ nm}$.

Here, as before, A_j and $\mathbf{E}_{j,\parallel}$ are the amplitude and the transverse part of the j th field of the mode with the propagation constant $\tilde{\beta}_j^{(o)}$. Hence, in the scalar theory, the dynamics of A_j is determined by the following four coupled equations [5]:

$$\frac{dA_1}{dz} = i \left(\gamma_1 |A_1|^2 + 2 \sum_{j \neq 1} \gamma_{1j} |A_j|^2 \right) A_1 + 2i \gamma_{1234} A_2^* A_3 A_4 e^{i \Delta \tilde{\beta}^{(o)} z}, \quad (4.2a)$$

$$\frac{dA_2}{dz} = i \left(\gamma_2 |A_2|^2 + 2 \sum_{j \neq 2} \gamma_{2j} |A_j|^2 \right) A_2 + 2i \gamma_{2134} A_1^* A_3 A_4 e^{i \Delta \tilde{\beta}^{(o)} z}, \quad (4.2b)$$

$$\frac{dA_3}{dz} = i \left(\gamma_3 |A_3|^2 + 2 \sum_{j \neq 3} \gamma_{3j} |A_j|^2 \right) A_3 + 2i \gamma_{3412} A_4^* A_1 A_2 e^{-i \Delta \tilde{\beta}^{(o)} z}, \quad (4.2c)$$

$$\frac{dA_4}{dz} = i \left(\gamma_4 |A_4|^2 + 2 \sum_{j \neq 4} \gamma_{4j} |A_j|^2 \right) A_4 + 2i \gamma_{4312} A_3^* A_1 A_2 e^{-i \Delta \tilde{\beta}^{(o)} z}. \quad (4.2d)$$

Here, A_1 and A_2 are the first and the second pump wave amplitude, respectively, while A_3 and A_4 are the Stokes and the anti-Stokes wave amplitude, respectively. The wave-vector mismatch $\Delta \tilde{\beta}^{(o)}$ between these waves is given by

$$\Delta \tilde{\beta}^{(o)} = \tilde{\beta}_3^{(o)} + \tilde{\beta}_4^{(o)} - \tilde{\beta}_1^{(o)} - \tilde{\beta}_2^{(o)}. \quad (4.3)$$

The nonlinearity parameters $\gamma_j \equiv \gamma_{jjjj}$ [same as Eq. (3.19)], $\gamma_{jl} \equiv \gamma_{jljl}$, and γ_{jlpq} is defined as

$$\gamma_{jlpq} = n_2 k_j \frac{\int_{-\infty}^{+\infty} \left(\mathbf{E}_{j,\parallel}^* \mathbf{E}_{l,\parallel}^* \mathbf{E}_{p,\parallel} \mathbf{E}_{q,\parallel} \right) d\mathbf{r}_{\parallel}}{N_j N_l N_p N_q}, \quad (4.4)$$

with the normalization constant

$$N_j = \left(\int_{-\infty}^{+\infty} |\mathbf{E}_{j,\parallel}|^2 d\mathbf{r}_{\parallel} \right)^{1/2}. \quad (4.5)$$

In Eqs. (4.2a) to (4.2d), γ_j , γ_{jl} , and γ_{jlpq} quantify the self-phase modulation, the cross-phase modulation, and four-wave mixing, respectively. As we can note, Eq. (4.4) is the nondegenerate form of Eq. (3.19) from the previous chapter. It means, that the self-phase modulation and the

cross-phase modulation are particular cases of the more general process of four-wave mixing with different orders of degeneracy.

Eqs. (4.2a) to (4.2d) are valid for so-called quasi-continuous wave regime (nanosecond pulses) in which the group-velocity dispersion can be neglected [5]. In the ultrafast regime, i.e. for a picosecond pulses the left hand side of Eqs. (4.2a) to (4.2d) should be replaced with

$$\frac{dA_j}{dz} \rightarrow \frac{\partial A_j}{\partial z} + \tilde{\beta}_j^{(1)} \frac{\partial A_j}{\partial t} + i \frac{\tilde{\beta}_j^{(2)}}{2} \frac{\partial^2 A_j}{\partial t^2} + \frac{\tilde{\alpha}_j^{(0)}}{2} A_j. \quad (4.6)$$

In principle, based on the full vectorial model for the nonlinear pulse propagation derived in Ref. [15], we can obtain a more accurate, vectorial form of the coupled amplitude equations for four-wave mixing. Indeed, considering the coupling of excitations of four frequencies, one can get a similar coupled equations as in case of the scalar theory. The difference between the scalar and the vectorial formulations are in the nonlinearity parameters. In the latter case, they are given by $\gamma_j = k_j \alpha_{jjjj}$ [same as Eq. (3.23)], $\gamma_{jl} = k_j (\alpha_{jljl} + \alpha_{jjll})$, and $\gamma_{jlpq} = k_j (\alpha_{jlpq} + \alpha_{jqpl})$ with the overlap integral of the form

$$\alpha_{jlpq} = \int_{-\infty}^{+\infty} n^2 n_2 \left\{ 2 \frac{(\mathbf{E}_j^* \cdot \mathbf{E}_q)(\mathbf{E}_l \cdot \mathbf{E}_p^*)}{3N_j N_l N_p N_q} + \frac{(\mathbf{E}_j^* \cdot \mathbf{E}_p^*)(\mathbf{E}_l \cdot \mathbf{E}_q)}{3N_j N_l N_p N_q} \right\} d\mathbf{r}_{\parallel}, \quad (4.7)$$

where the normalization constant N_j of the mode fields is [see also Section 2.4.1]

$$N_j = \left(\int_{-\infty}^{+\infty} S_{j,z} d\mathbf{r}_{\parallel} \right)^{1/2}. \quad (4.8)$$

These scalar and vectorial approaches for four-wave mixing are valid only for bound modes due to the absence of a rigorous normalization [see also Chapter 3]. In the next sections, based on the master nonlinear pulse propagation equation with the correct mode normalization, we provide a general theory for four-wave mixing. We will consider the vectorial formulation, hereinafter referred to as bound-mode theory, as a reference to our theory of four-wave mixing.

4.2 GENERAL COUPLED AMPLITUDE EQUATIONS

In the Chapter 3, we have shown that the evolution of the modal amplitude $a_m(z; t)$ can be described by the following general master equation [A2]:

$$\begin{aligned} \frac{\partial a_m(z; t)}{\partial z} = & i\beta_m(t) * a_m(z; t) - \\ & \frac{2\pi}{c} \frac{\partial}{\partial t} \int \mathbf{e}_m^R(\mathbf{r}_{||}; t) * \mathbf{P}_{\text{NL}}(\mathbf{r}; t) d\mathbf{r}_{||}. \end{aligned} \quad (4.9)$$

For further convenience, we consider its frequency domain form:

$$\begin{aligned} \frac{\partial a_m(z; \omega)}{\partial z} = & i\beta_m(\omega) a_m(z; \omega) + \\ & \frac{2\pi i \omega}{c} \int \mathbf{e}_m^R(\mathbf{r}_{||}; \omega) \cdot \mathbf{P}_{\text{NL}}(\mathbf{r}_{||}, z; \omega) d\mathbf{r}_{||}. \end{aligned} \quad (4.10)$$

Several assumptions are introduced in the following to simplify this master equation. First, we restrict the analysis to the fundamental leaky core mode, which allows us to omit the mode index m in Eq. (4.10). Hence, the electric field $\mathbf{E}(\mathbf{r}; \omega)$ can be written as

$$\mathbf{E}(\mathbf{r}; \omega) = \sum_m a_m(z; \omega) \frac{\mathbf{E}_m(\mathbf{r}_{||}; \omega)}{N_m^{1/2}} \approx a(z; \omega) \mathbf{e}(\mathbf{r}_{||}; \omega). \quad (4.11)$$

The latter approximation is the discrimination of the fundamental mode from higher-order modes. Indeed, for sufficiently long fibers only the fundamental mode can propagate since it usually has the lowest attenuation constant [21, 58].

Next, we assume that optical pulses propagating in a fiber are narrow-band and centered around carrier frequencies ω_j ($j = 1, 2, 3, \dots$). Thus, the electric field $\mathbf{E}(\mathbf{r}; \omega)$ can be approximated as a superposition of the electric fields at these dominant carrier frequencies:

$$\mathbf{E}(\mathbf{r}; \omega) \approx \sum_j a_j(z; \omega) \mathbf{e}(\mathbf{r}_{||}; \omega_j). \quad (4.12)$$

Note that in Eq. (4.12) and following, the frequency dependence of the transverse spatial distribution of the electric field is assumed to be negligible (i.e., all fields are the same), i.e., $\mathbf{e}(\mathbf{r}_{||}; \omega) \approx \mathbf{e}(\mathbf{r}_{||}; \omega_j)$, and $a_j(z; \omega)$ is spectrally separated for the different dominant frequencies.

Thus, Eq. (4.10) after these approximation takes the following form:

$$\frac{\partial a_j(z; \omega)}{\partial z} = i\beta(\omega)a_j(z; \omega) + \frac{2\pi i\omega}{c} \int \mathbf{e}^{\mathbf{R}}(\mathbf{r}_{\parallel}; \omega) \cdot \mathbf{P}_{\text{NL}}(\mathbf{r}_{\parallel}, z; \omega) d\mathbf{r}_{\parallel}. \quad (4.13)$$

Note that the nonlinear part of Eq. (4.13) is not changed so far. Let us at the beginning finish with the linear part of the equation. Hence, we make the typical approximation by expanding $\beta(\omega)$ into a Taylor series around ω_j :

$$\beta(\omega) \equiv \bar{\beta}(\omega) + i\bar{\alpha}(\omega) \approx \sum_{n \geq 0} \left(\frac{\bar{\beta}_j^{(n)}}{n!} + i \frac{\bar{\alpha}_j^{(n)}}{n!} \right) (\omega - \omega_j)^n, \quad (4.14)$$

where

$$\bar{\beta}_j^{(n)} = \left. \frac{\partial^n \bar{\beta}}{\partial \omega^n} \right|_{\omega_j}, \quad (4.15)$$

and

$$\bar{\alpha}_j^{(n)} = \left. \frac{\partial^n \bar{\alpha}}{\partial \omega^n} \right|_{\omega_j}, \quad (4.16)$$

are the n th-order dispersion and loss coefficients at ω_j , respectively. Additionally, we use that for narrowband pulses with a carrier frequency ω_j , the modal amplitude a_j can be split into slowly and rapidly varying parts as

$$a_j(z; t) \equiv A_j(z; t) e^{i\bar{\beta}_j^{(0)} z - i\omega_j t}, \quad (4.17)$$

that has the following frequency domain form:

$$a_j(z; \omega) \equiv A_j(z; \omega - \omega_j) e^{i\bar{\beta}_j^{(0)} z}. \quad (4.18)$$

Thus, taking into account Eq. (4.14) and Eq. (4.18), we obtain the following equation for the slowly varying part (envelope) $A_j(z; \omega - \omega_j)$:

$$\frac{\partial A_j(z; \omega - \omega_j)}{\partial z} = \hat{D}_j(\omega - \omega_j) A_j(z; \omega - \omega_j) + \frac{2\pi i\omega}{c} e^{-i\bar{\beta}_j^{(0)} z} \int \mathbf{e}^{\mathbf{R}}(\mathbf{r}_{\parallel}; \omega) \cdot \mathbf{P}_{\text{NL}}(\mathbf{r}_{\parallel}, z; \omega) d\mathbf{r}_{\parallel}, \quad (4.19)$$

where the dispersion operator \hat{D}_j is defined as

$$\hat{D}_j(\omega - \omega_j) = \sum_{n \geq 0} \left[i \frac{\tilde{\beta}_j^{(n+1)}}{(n+1)!} (\omega - \omega_j)^{n+1} - \frac{\tilde{\alpha}_j^{(n)}}{n!} (\omega - \omega_j)^n \right]. \quad (4.20)$$

Let us now address the nonlinear part of Eq. (4.19). As before, we assume that $\mathbf{e}^R(\mathbf{r}_\parallel; \omega) \approx \mathbf{e}^R(\mathbf{r}_\parallel; \omega_j) \equiv \mathbf{e}_j^R(\mathbf{r}_\parallel)$, which allows us to avoid convolutions when transforming to the time domain. Furthermore, as in the case of the linear part of Eq. (4.19), we consider only the dominant frequencies. Thus, by carrying out the Fourier transform of Eq. (4.19) according to

$$A_j(z; t) = \frac{1}{2\pi} \int_{-\infty}^{+\infty} A_j(z; \omega - \omega_j) e^{-i(\omega - \omega_j)t} d\omega, \quad (4.21)$$

we obtain:

$$\begin{aligned} \frac{\partial A_j(z; t)}{\partial z} &= \hat{D}_j \left(i \frac{\partial}{\partial t} \right) A_j(z; t) - \\ &\quad \frac{2\pi}{c} e^{i\omega_j t - i\tilde{\beta}_j^{(0)} z} \frac{\partial}{\partial t} \int \mathbf{e}_j^R(\mathbf{r}_\parallel) \cdot \mathbf{P}_{\text{NL}}(\mathbf{r}_\parallel, z; t) d\mathbf{r}_\parallel. \end{aligned} \quad (4.22)$$

Next, we assume the nonlinear polarization \mathbf{P}_{NL} of the form Eq. (3.11) with the total electric field

$$\mathbf{E}(\mathbf{r}; t) \approx \sum_{j=1}^4 A_j(z; t) \mathbf{e}_j(\mathbf{r}_\parallel) e^{i\tilde{\beta}_j^{(0)} z - i\omega_j t} + \text{c.c.} \quad (4.23)$$

Taking into account Eq. (3.11) and Eq. (4.23), we can rewrite Eq. (4.22) as

$$\frac{\partial A_j(z; t)}{\partial z} = \hat{D}_j \left(i \frac{\partial}{\partial t} \right) A_j(z; t) + i \left(1 - \frac{1}{i\omega_j} \frac{\partial}{\partial t} \right) I_j(z; t), \quad (4.24)$$

where

$$I_j(z; t) \equiv 2\pi k_j \int \mathbf{e}_j^R(\mathbf{r}_\parallel) \cdot \mathbf{P}_{\text{NL}}(\mathbf{r}_\parallel, z; t) e^{i\omega_j t - i\tilde{\beta}_j^{(0)} z} d\mathbf{r}_\parallel. \quad (4.25)$$

For the sake of convenience, we split the integral I_j into two parts as

$$I_j = \sum_{l,p,q} I_{jlpq} = \sum_{l,p,q} \left[I_{jlpq}^{(1)} + I_{jlpq}^{(2)} \right], \quad (4.26)$$

with

$$I_{jl,pq}^{(1)} = \gamma_{jl,pq}^{(1)} A_l^* A_p A_q e^{i\phi_{pq,lj}}, \quad (4.27)$$

$$I_{jl,pq}^{(2)} = \gamma_{jl,pq}^{(2)} A_l A_p A_q^* e^{i\phi_{lp,qj}}, \quad (4.28)$$

and

$$\gamma_{jl,pq}^{(1)} = k_j \int n_2(\mathbf{e}_j^R \cdot \mathbf{e}_l^*)(\mathbf{e}_p \cdot \mathbf{e}_q) d\mathbf{r}_{||}, \quad (4.29)$$

$$\gamma_{jl,pq}^{(2)} = k_j \int 2n_2(\mathbf{e}_j^R \cdot \mathbf{e}_l)(\mathbf{e}_p \cdot \mathbf{e}_q^*) d\mathbf{r}_{||}. \quad (4.30)$$

Here, the general phase difference $\phi_{jl,pq}$ is defined as

$$\phi_{jl,pq} = \Delta \bar{\beta}_{jl,pq}^{(o)} z - \Delta \omega_{jl,pq} t, \quad (4.31)$$

with

$$\Delta \bar{\beta}_{jl,pq}^{(o)} = \left(\bar{\beta}_j^{(o)} + \bar{\beta}_l^{(o)} \right) - \left(\bar{\beta}_p^{(o)} + \bar{\beta}_q^{(o)} \right), \quad (4.32)$$

and

$$\Delta \omega_{jl,pq} = (\omega_j + \omega_l) - (\omega_p + \omega_q). \quad (4.33)$$

The complete expression for I_j includes a large number of terms involving the products of three amplitudes. Nevertheless, we can distinguish the terms responsible for self-phase modulation, cross-phase modulation, and four-wave mixing. For instance, in the case that $q = p = l = j$, we obtain the following term for self-phase modulation:

$$I_j^{\text{SPM}} = I_{jjjj}^{(1)} + I_{jjjj}^{(2)} = \gamma_j |A_j|^2 A_j, \quad (4.34)$$

where $\gamma_j = \gamma_{jjjj}^{(1)} + \gamma_{jjjj}^{(2)}$ [same as Eq. (3.26)]. Similarly, the sum over the index pairs ($p = j, q = l$), ($p = l, q = j$), and ($p = q = l, l = j$) provides terms for the cross-phase modulation:

$$I_{jl}^{\text{XPM}} = I_{jljl}^{(1)} + I_{jljl}^{(1)} + I_{jljl}^{(2)} + I_{jljl}^{(2)} = \sum_{l \neq j} \gamma_{jl} |A_l|^2 A_j. \quad (4.35)$$

where

$$\gamma_{jl} = k_j \sum_{l \neq j} \int 2n_2 \left[(\mathbf{e}_j^R \cdot \mathbf{e}_l^*) (\mathbf{e}_j \cdot \mathbf{e}_l) + (\mathbf{e}_j^R \cdot \mathbf{e}_l) (\mathbf{e}_j \cdot \mathbf{e}_l^*) + (\mathbf{e}_j^R \cdot \mathbf{e}_j) |\mathbf{e}_l|^2 \right] d\mathbf{r}_{\parallel}. \quad (4.36)$$

By collecting the terms for which $q \neq p \neq l \neq j$, we obtain the four-wave mixing contribution to Eq. (4.25):

$$I_{jlpq}^{\text{FWM}} = I_{jlpq}^{(1)} + I_{jlqp}^{(1)} + I_{jlpq}^{(2)} + I_{jlqp}^{(2)} = \gamma_{jlpq} A_l^* A_p A_q e^{i\Delta\tilde{\beta}_{pq,lj}^{(o)} z}, \quad (4.37)$$

where

$$\gamma_{jlpq} = k_j \int 2n_2 \left[(\mathbf{e}_j^R \cdot \mathbf{e}_l^*) (\mathbf{e}_p \cdot \mathbf{e}_q) + (\mathbf{e}_j^R \cdot \mathbf{e}_q) (\mathbf{e}_p \cdot \mathbf{e}_l^*) + (\mathbf{e}_j^R \cdot \mathbf{e}_p) (\mathbf{e}_q \cdot \mathbf{e}_l^*) \right] d\mathbf{r}_{\parallel}. \quad (4.38)$$

Note that in Eq. (4.37) and Eq. (4.38), we permuted the second and the fourth indices of $I_{abcd}^{(2)}$ and $\gamma_{abcd}^{(2)}$. Furthermore, the particular case, in which $q \neq p \neq l = j$ or ($q = p \neq l \neq j$), is known as three-wave mixing or degenerate four-wave mixing.

In general, Eq. (4.25) contains many other phase terms responsible for phenomena such as frequency tripling ($\omega_q = \omega_j + \omega_l + \omega_p$) or other frequency conversion processes (e.g., $\omega_q = 2\omega_j + \omega_p$). Here, we neglect such contributions, since from the quantum-mechanical point of view, the probability of these processes is rather low [5]. Additionally, we neglect the time derivative term on the right hand side of Eq. (4.24) that accounts for the dispersion of the nonlinearity, leading to nonlinear effects such as self-steepening and optical shock formation, which only become important for femtosecond pulses [5]. Therefore, we keep only all dominant terms that are responsible for processes such as self-phase modulation, cross-phase modulation, and four-wave mixing. Under these assumptions, Eq. (4.24) applied to each field at frequencies ω_j

($j = 1-4$) leads to the following set of four coupled amplitude equations:

$$\frac{\partial A_1}{\partial z} = (\hat{D}_1 + \hat{N}_1)A_1 + i\gamma_{1234}A_2^*A_3A_4e^{i\Delta\tilde{\beta}^{(o)}z}, \quad (4.39a)$$

$$\frac{\partial A_2}{\partial z} = (\hat{D}_2 + \hat{N}_2)A_2 + i\gamma_{2134}A_1^*A_3A_4e^{i\Delta\tilde{\beta}^{(o)}z}, \quad (4.39b)$$

$$\frac{\partial A_3}{\partial z} = (\hat{D}_3 + \hat{N}_3)A_3 + i\gamma_{3412}A_4^*A_1A_2e^{-i\Delta\tilde{\beta}^{(o)}z}, \quad (4.39c)$$

$$\frac{\partial A_4}{\partial z} = (\hat{D}_4 + \hat{N}_4)A_4 + i\gamma_{4312}A_3^*A_1A_2e^{-i\Delta\tilde{\beta}^{(o)}z}, \quad (4.39d)$$

with the nonlinear operator

$$\hat{N}_j \equiv i\left(\gamma_j|A_j|^2 + \sum_{l \neq j} \gamma_{jl}|A_l|^2\right), \quad (4.40)$$

and the linear phase-mismatch

$$\Delta\tilde{\beta}^{(o)} \equiv \Delta\tilde{\beta}_{34,21}^{(o)} = \Delta\tilde{\beta}_{34,12}^{(o)} = -\Delta\tilde{\beta}_{12,43}^{(o)} = -\Delta\tilde{\beta}_{12,34}^{(o)}. \quad (4.41)$$

Thus, the system of Eqs. (4.39a) to (4.39d) describes four-wave mixing for bound and leaky modes. The efficiency of four-wave mixing depends on the wave-vector mismatch $\Delta\tilde{\beta}^{(o)}$ and becomes maximum when it vanishes, i.e., $\Delta\tilde{\beta}^{(o)} = 0$.

It should be noted that Eqs. (4.39a) to (4.39d) look similar to the scalar and vectorial formulations [see Section 4.1] [5, 15]. However, the main difference is in the nonlinearity parameters. While in Eqs. (4.39a) to (4.39d), the reciprocal conjugation is the identical operation to the complex conjugation for bound modes, it yields different results for leaky modes. Therefore, all nonlinearity coefficients in Eqs. (4.39a) to (4.39d) deviate from those of the conventional bound-mode theory when considering leaky modes. Particularly, as we have shown in Chapter 3, they exhibit a non-vanishing imaginary part that is either positive, corresponding to nonlinear loss [16, 32, 33], or negative acting as nonlinear gain for overall attenuating fields [A2]. In the next sections, we numerically analyze the impact of our new formulation on four-wave mixing of leaky modes by comparing it with results that are based on applying the bound-mode theory to leaky modes. In order to do that, we basically ignore any issues with the normalization of bound modes

using the conventional theory and assume that the real part of the nonlinearity coefficients has been calculated correctly, while we neglect its imaginary part.

4.3 MODULATION INSTABILITY IN HOLLOW-CORE FIBERS

In general, the system of Eqs. (4.39a) to (4.39d) describes narrowband pulses that are spectrally separated. However, for small frequency spacings (< 1 THz), it is more convenient to use a single nonlinear Schrodinger equation with a certain initial condition [5]. In that case, an interaction between the nonlinear and dispersive effects can lead to the generation of new frequencies from noise, which is also known as modulation instability [5]. Typically, the nonlinearity parameter γ is assumed to be a real quantity in the stability analysis of the modulations. However, as mentioned in the introduction, the nonlinearity parameter γ has a negative imaginary part for hollow-core fibers supporting leaky modes that can act as a nonlinear gain, partially diminishing the impact of modal attenuation during propagation [A2]. Hence, we observe here an interplay between nonlinear gain and modal loss besides self-phase modulation and group velocity dispersion. In this section, we derive steady-state solutions in this regime and analyze their stability against small perturbations.

In the following, for the sake of simplicity, we consider the standard nonlinear Schrodinger equation with a complex nonlinearity parameter and linear loss:

$$i \frac{\partial A}{\partial z} - \frac{\tilde{\beta}^{(2)}}{2} \frac{\partial^2 A}{\partial \tau^2} + (\gamma_r + i\gamma_i)|A|^2 A + i\tilde{\alpha}^{(o)} A = 0. \quad (4.42)$$

Here, γ_r (> 0 self-focusing, < 0 self-defocusing) and γ_i (> 0 nonlinear loss, < 0 nonlinear gain) are the real and imaginary parts of the nonlinearity parameter γ , respectively. Below, we consider the self-focusing case.

Considering Eq. (4.42) as a dynamical system, yields the following steady-state solution [O1, 97]:

$$A = A_o e^{i\gamma_r |A_o|^2 z}, \quad (4.43)$$

where

$$A_o = \left(-\frac{\tilde{\alpha}^{(o)}}{\gamma_i} \right)^{1/2}. \quad (4.44)$$

This basically means that we require a suitable balance between linear attenuation and nonlinear gain.

In order to investigate modulation instability, we add a small perturbation to the steady-state solution [5]:

$$\tilde{A} = [A_o + a(z, \tau)] e^{i\gamma_r |A_o|^2 z} = A + a e^{i\gamma_r |A_o|^2 z}, \quad (4.45)$$

where $a(z, \tau)$ is the small perturbation.

Substituting Eq. (4.45) in Eq. (4.42) and linearizing $a(z, \tau)$, we obtain after some algebra:

$$i \frac{\partial a}{\partial z} - \frac{\tilde{\beta}^{(2)}}{2} \frac{\partial^2 a}{\partial \tau^2} + (\gamma_r + i\gamma_i) |A_o|^2 (a + a^*) = 0. \quad (4.46)$$

A general solution of Eq. (4.46) can be written as

$$a(z, \tau) = u(z) e^{i\Omega\tau} + v^*(z) e^{-i\Omega\tau}, \quad (4.47)$$

where u and v are the coefficients determined by solving Eq. (4.46), and Ω is the frequency of the modulation.

By introducing $b = u + v$ and $c = u - v$ and by inserting Eq. (4.47) into Eq. (4.46), we obtain the following system of homogeneous equations:

$$\frac{\partial}{\partial z} \begin{pmatrix} b \\ c \end{pmatrix} = \underbrace{\begin{pmatrix} -2\gamma_i |A_o|^2 & i \frac{\tilde{\beta}^{(2)}}{2} \Omega^2 \\ i \frac{\tilde{\beta}^{(2)}}{2} \Omega^2 + 2i\gamma_r |A_o|^2 & 0 \end{pmatrix}}_M \begin{pmatrix} b \\ c \end{pmatrix}. \quad (4.48)$$

Searching for the eigenvalues Γ of the matrix M , we obtain a characteristic equation of the form

$$\Gamma^2 + 2\gamma_i |A_o|^2 \Gamma + \frac{\tilde{\beta}^{(2)}}{2} \Omega^2 \left(\frac{\tilde{\beta}^{(2)}}{2} \Omega^2 + 2\gamma_r |A_o|^2 \right) = 0, \quad (4.49)$$

which has solutions

$$\Gamma_{\pm} = -\gamma_i |A_o|^2 \pm \left[\left(\gamma_i |A_o|^2 \right)^2 - \left(\frac{\tilde{\beta}^{(2)}}{2} \Omega \right)^2 \left(\Omega^2 + \text{sgn}(\tilde{\beta}^{(2)}) \Omega_c^2 \right) \right]^{1/2}, \quad (4.50)$$

where $\text{sgn}(\tilde{\beta}^{(2)}) = \pm 1$ depends on the sign of $\tilde{\beta}^{(2)}$ and

$$\Omega_c^2 = \frac{4\gamma_r |A_0|^2}{|\tilde{\beta}^{(2)}|}. \quad (4.51)$$

This yields

$$b(z) = b_+ e^{\Gamma+z} + b_- e^{\Gamma-z}, \quad (4.52)$$

$$c(z) = c_+ e^{\Gamma+z} + c_- e^{\Gamma-z}, \quad (4.53)$$

where b_{\pm} and c_{\pm} depend on the initial conditions of the perturbation a . Note that Γ can be related to a wavenumber K of the perturbation as $\Gamma = iK$. In fact, perturbations can grow exponentially along the fiber in the regime with $\gamma_i < 0$, since the first line on the right-hand side of Eq. (4.50) always yields a nonvanishing positive real part for any real Ω . Interestingly, this does not depend on the sign of $\tilde{\beta}^{(2)}$ – in contrast to the modulation instability described in the literature, which occurs only in the anomalous dispersion regime ($\tilde{\beta}^{(2)} < 0$) at certain frequencies [5].

Furthermore, we also note that the first line on the right-hand side of Eq. (4.50) does not depend on the frequency. This already indicates that the modulation instability can occur at any wavelength. For further analysis of the results, we introduce the gain spectrum defined as $g(\Omega) = 2 \text{Re}(\Gamma)$. As we can deduce from Eq. (4.50), the gain is minimal if the expression under the square root is negative. This minimal or "background" gain is given by $g_{\min} = -2\gamma_i |A_0|^2 = 2\tilde{\alpha}^{(0)}$ for frequencies Ω with

$$\Omega^2 \geq \Omega_{\pm}^2 \equiv \frac{1}{2} \Omega_c^2 \left\{ \left[1 + \left(\frac{\gamma_i}{\gamma_r} \right)^2 \right]^{1/2} - \mp 1 \right\}, \quad (4.54)$$

where Ω_+ and Ω_- correspond to the normal and the anomalous dispersion, respectively.

As we can see in Fig. 4.2, inside the frequency window $\Omega^2 < \Omega_{\pm}^2$, the gain spectrum can always exceed g_{\min} . It has two maxima at $\Omega = \pm \Omega_c / 2^{1/2}$ in the anomalous dispersion regime (red dashed line) while in the case of normal dispersion (green solid line) $g(\Omega)$ is maximum at $\Omega = 0$.

Here, we note that the steady-state solution of Eq. (4.42) and accordingly the dispersion relation Eq. (4.50) are determined uniquely by the

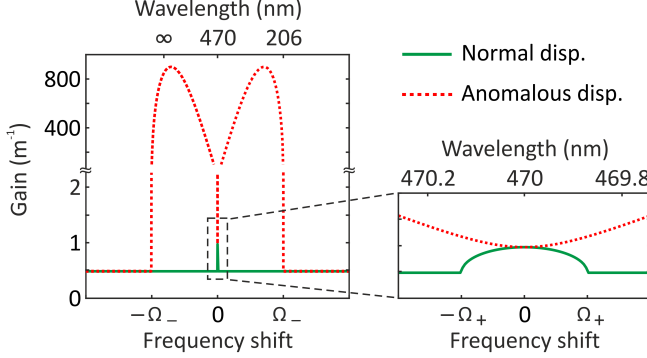


Figure 4.2. Gain spectra of modulation instability at a pump wavelength of $\lambda = 470$ nm for the annulus fiber with $\gamma = (8.47 \times 10^{-6} - 4.58 \times 10^{-9}i) \text{ m}^{-1}\text{W}^{-1}$, $\alpha = 0.24 \text{ m}^{-1}$, and $|\tilde{\beta}^{(2)}| = 6.84 \times 10^{-2} \text{ ps}^2\text{km}^{-1}$. The red dashed line indicates the gain spectrum of modulation instability calculated in the anomalous dispersion regime with $\text{sgn}(\tilde{\beta}^{(2)}) = -1$, while the solid green line is obtained for $\text{sgn}(\tilde{\beta}^{(2)}) = 1$, corresponding to the normal dispersion regime. Note that in both cases, there is a nonzero gain for all frequencies.

fiber parameters. Waves with such properties are sometimes called autowaves [98]. Particularly, localized waves in gain-loss-balanced nonlinear systems are referred to as autosolitons or dissipative solitons [99].

4.4 OPTICAL SYSTEM AND SIMULATION DETAILS

In this section, we provide geometrical and optical parameters of a test system as well as details of the numerical simulations of the coupled nonlinear pulse propagation equations. At first, we discuss optical properties of the chosen waveguide geometry such as the linear dispersion and the nonlinear characteristics. Furthermore, we estimate the position of the Stokes and the anti-Stokes bands that are required in further numerical simulations. In the second subsection, we mostly concentrate on the parameters of the numerical simulations by considering e.g., the time-frequency discretization, and the choice of longitudinal computation steps.

4.4.1 *The optical system parameters*

As example of an optical system for our numerical investigation, we consider an annulus fiber made from silica (SiO_2) and filled by xenon (Xe) with a nitrogen (N) surrounding [see Fig. 4.1 (a)]. The inner and outer radii of the annulus are $R_1 = 30 \mu\text{m}$ and $R_2 = 30.476 \mu\text{m}$, respectively. The optical parameters of this waveguide such as the linear and nonlinear refractive indices are taken from Refs. [94, 95, 100, 101]. Here, we assume that the pressure inside (Xe) and outside (N) the fiber are 1 bar and 4 bar, respectively. Thus, with these geometrical and optical parameters of the annulus fiber, we are able to design a dispersion curve such that it yields a strong impact of our theory.

The modal properties of the fiber are found by solving Maxwell's equations. Following the procedures described in the literature [28, 41], we can derive an eigenvalue equation for the propagation constant β . Panels (a) and (b) in Fig. 4.3 display the real and imaginary parts of the effective refractive index $n_{\text{eff}} = \beta/k$ of the fundamental leaky mode of the fiber as a function of wavelength. Since the silica layer can be considered as a Fabry-Perot-type resonator, it has resonances at the wavelengths [102]

$$\lambda = \frac{2(R_2 - R_1)}{m} \left[n_{\text{SiO}_2}^2(\lambda) - n_{\text{Xe}}^2(\lambda) \right]^{1/2}, \quad (4.55)$$

where $m = 1, 2, \dots$ with the modal loss [$\propto \text{Im}(n_{\text{eff}})$] having their maxima at these resonances. In the wavelength range, considered in Fig. 4.3, we can see the second ($m = 2$) resonance at $\lambda = 507 \text{ nm}$.

Next, we use the solutions of the eigenvalue problem to calculate the nonlinear parameters. For instance, panels (c) and (d) in Fig. 4.3 display the real and imaginary parts of the nonlinearity parameter γ of the fundamental leaky mode of the fiber as a function of wavelength. In these panels, the red solid line indicates the results obtained by using the resonant-state expansion, while the blue dots are based on the results of bound-mode theory. Details about the difference between resonant-state expansion and bound-mode theory can be found at the end of Section 4.2. We note that in both cases the contribution of the surrounding gas, i.e., nitrogen, to the nonlinear parameters is neglected, since $\chi_{e,\text{SiO}_2}^{(3)} \gg \chi_{e,\text{Xe}}^{(3)} \gg \chi_{e,\text{N}}^{(3)}$ [101]. Furthermore, we can consider the smallest region with spatial inhomogeneities, i.e., $R = R_2$ as the radius of normalization in Eq. (2.59). In the case of bound-mode theory, fiber modes are normalized with respect to the axial component of the time-

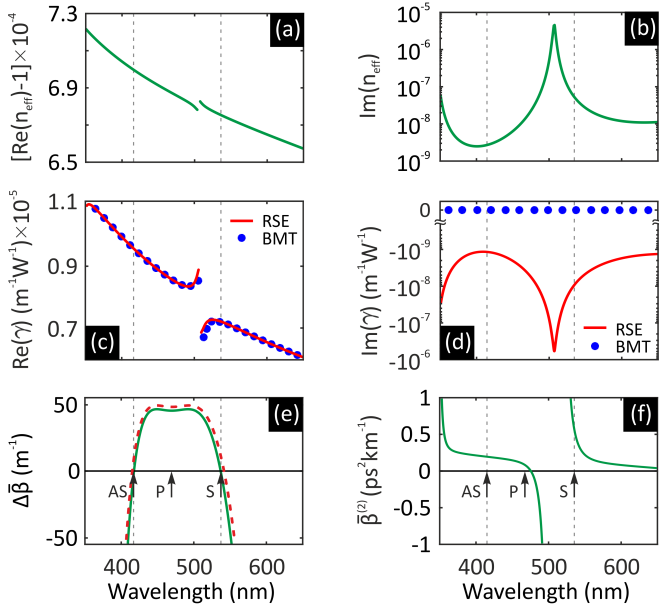


Figure 4.3. Spectral distributions of the various relevant parameters. (a) Real and (b) imaginary parts of the effective refractive index of the fundamental leaky mode of the annulus fiber shown in Fig. 4.1. Comparisons of results obtained by the resonant-state expansion and the bound-mode theory for the real and imaginary parts of the nonlinearity parameter of the fundamental leaky mode of the same fiber are given in panels (c) and (d), respectively. (e) Phase mismatch for degenerate four-wave mixing at a pump wavelength of 470 nm and an initial power of 3.1 MW (green solid line) and 3.2 MW (red dashed line), respectively. The central arrow indicates the position of pump (P) wave, while the side arrows indicate the estimated positions of the Stokes (S) and the anti-Stokes (AS) bands that occur at the wavelength with vanishing phase mismatch. (f) Second-order dispersion coefficient. All three waves are in the normal dispersion region. The gray vertical dashed lines in all panels indicate the spectral positions of the Stokes and the anti-Stokes waves.

averaged Poynting vector with a radius of normalization of $R = \infty$. However, infinite radius of normalization applied to leaky modes yields a vanishing value for the nonlinearity parameter γ , since the fields of leaky modes diverge [see Fig. 4.1 (b)]. Therefore, we choose the radius of normalization such that the deviation of the real part of γ between the resonant-state expansion and the bound-mode theory is minimized. As we can see in Fig. 4.3 (c), the real part of the nonlinearity parameter γ is similar in both approaches. However, the bound-mode theory solely provides a purely real γ .

The estimated positions of the Stokes and anti-Stokes waves for particular pump wave parameters (wavelength and power) are defined by the phase-matching condition. In order to have the most efficient side-band generation, it is necessary to compensate the linear wave-vector mismatch $\Delta\tilde{\beta}^{(0)}$ between the pump and side bands with the nonlinear phase shifts caused by self-phase and cross-phase modulations. For the sake of simplicity we consider degenerate four-wave mixing, for which $\omega_1 = \omega_2$. In this case, we can write the phase-matching condition as follows [5]:

$$\Delta\tilde{\beta} = \left(\tilde{\beta}^{(2)}\Omega_s^2 + \frac{\tilde{\beta}^{(4)}}{12}\Omega_s^4 \right) + 2\gamma_r P_1 \approx 0. \quad (4.56)$$

Here, $\Omega_s = \omega_1 - \omega_3 = \omega_4 - \omega_1$ is the frequency shift with respect to the pump frequency ω_1 , $\tilde{\beta}^{(2)}$ and $\tilde{\beta}^{(4)}$ are the dispersion parameters at ω_1 , and γ_r is the real part of the nonlinearity parameter γ at the pump frequency.

In order to exclude a strong impact of modulation instability and consider rather typical four-wave mixing, we choose the pump wave parameters such that all the pump wave and Stokes side-bands are in the normal dispersion regime. In this case, the phase-matching condition can be satisfied if $\tilde{\beta}^{(4)} < 0$. For example, as shown in Fig. 4.3 (d), for the pump wave with an initial power of $P_1 = 3.1$ MW and a wavelength of $\lambda_1 = 470$ nm, at which $\tilde{\beta}^{(2)} = 6.84 \times 10^{-2}$ ps²km⁻¹, $\tilde{\beta}^{(4)} = -1.14 \times 10^{-5}$ ps⁴km⁻¹, and $\gamma_r = 8.47 \times 10^{-6}$ m⁻¹W⁻¹, the phase mismatch vanishes at a wavelengths of $\lambda_3 = 540.6$ nm (Stokes) and $\lambda_4 = 415.8$ nm (anti-Stokes). In Fig. 4.3 (e), we see that all three (i.e., the pump, Stokes, and anti-Stokes) waves are in the normal dispersion region. The positions of the side bands can be easily tuned by varying the pump wave parameters.

4.4.2 Nonlinearity parameters

The system of Eqs. (4.39a) to (4.39d) include the nonlinearity parameters γ_{jl} and γ_{jlpq} in addition to the Kerr nonlinearity parameter γ_j . The latter is shown in panels (c) and (d) of Fig. 4.3. In this section, we discuss the nonlinearity parameters γ_{jl} and γ_{jlpq} that quantifies cross-phase modulation and four-wave mixing, respectively. Furthermore, we provide the complete table of nonlinear parameters of the optical system.

In the bound mode theory [see Eq. (4.7)], the nonlinearity parameters γ_{jl} , as we can see in the bottom of Tables 4.1 and 4.3, are real numbers. The same parameters that are calculated by using our formulation [see Eq. (4.36)] are complex numbers [top part of Tables 4.1 and 4.3].

The most interesting, as we can see in Tables 4.2 and 4.4, nondegenerate nonlinearity parameters γ_{jlpq} are in general complex numbers not only in our theory but also in the bound mode theory. Furthermore, in our approach, the imaginary part of γ_{jlpq} is negative for all cases that are considered here. However, it can have an opposite sign in the bound mode theory. Thus, we can conclude that no matter which method is used, nondegenerated nonlinearity parameter γ_{jlpq} is in general complex number for both bound and leaky modes.

4.4.3 Simulation details

So far, we have drawn our attention to determine the parameters of the fiber that enter Eqs. (4.39a) to (4.39d), while in the following, we discuss the details of the numerical simulations. As an initial condition for the amplitude of the pump pulse, we consider a hyperbolic secant profile

$$A_1(z = 0, t) = P_1^{1/2} \operatorname{sech}\left(\frac{t}{T_0}\right), \quad (4.57)$$

with the initial width $T_0 = 100$ ps. For such a relatively long pulse, we can neglect higher order nonlinear effects such as self-steepening and Raman scattering [5]. Still, these nonlinear effects could be considered in our model. However, as we have mentioned in Section 4.2, they become significant only for pico- or even femtosecond pulses. Furthermore, in this case, the higher-order Taylor expansion terms in Eq. (4.14) are generally negligible [5]. Hence, the real $\beta(\lambda)$ and the imaginary

APPROACH		PUMP	STOKES	ANTI-STOKES
γ_{jl}	l	$\lambda_1 = 470 \text{ nm}$	$\lambda_3 = 540.6 \text{ nm}$	$\lambda_4 = 415.8 \text{ nm}$
RSE	1	8.472×10^{-6} $-4.581 \times 10^{-9}i$	1.449×10^{-5} $-1.536 \times 10^{-8}i$	1.904×10^{-5} $-2.191 \times 10^{-9}i$
	2	1.694×10^{-5} $-9.162 \times 10^{-9}i$	1.449×10^{-5} $-1.536 \times 10^{-8}i$	1.904×10^{-5} $-2.191 \times 10^{-9}i$
	3	1.667×10^{-5} $-8.795 \times 10^{-9}i$	7.129×10^{-6} $-7.384 \times 10^{-9}i$	1.873×10^{-5} $-2.103 \times 10^{-9}i$
	4	1.684×10^{-5} $-9.025 \times 10^{-9}i$	1.440×10^{-5} $-1.514 \times 10^{-8}i$	9.461×10^{-5} $-1.079 \times 10^{-9}i$
BMT	1	8.465×10^{-6}	1.447×10^{-5}	1.903×10^{-5}
	2	1.693×10^{-5}	1.447×10^{-5}	1.903×10^{-5}
	3	1.665×10^{-5}	7.118×10^{-6}	1.871×10^{-5}
	4	1.683×10^{-5}	1.439×10^{-5}	9.460×10^{-5}

Table 4.1. The partially degenerate nonlinearity parameters γ_{jl} [in $\text{m}^{-1}\text{W}^{-1}$] calculated within the bound mode (BMT) and our (RSE) theories at the pump and side-bands spectral positions. The spectral positions (wavelengths) of the side-bands correspond to the initial pulse power of $P_1 = 3.1 \text{ MW}$.

APPROACH		PUMP	STOKES	ANTI-STOKES
γ_{jlpq}		$\lambda_1 = 470 \text{ nm}$	$\lambda_3 = 540.6 \text{ nm}$	$\lambda_4 = 415.8 \text{ nm}$
RSE		1.675×10^{-5} $-9.265 \times 10^{-10}i$	1.456×10^{-5} $-8.605 \times 10^{-9}i$	1.894×10^{-5} $-1.119 \times 10^{-8}i$
		1.674×10^{-5} $-1.648 \times 10^{-8}i$	1.455×10^{-5} $1.433 \times 10^{-8}i$	1.892×10^{-5} $-1.572 \times 10^{-8}i$
BMT		1.675×10^{-5}	1.456×10^{-5}	1.894×10^{-5}
		1.674×10^{-5}	1.455×10^{-5}	1.892×10^{-5}

Table 4.2. The nondegenerate nonlinearity parameters γ_{jlpq} [in $\text{m}^{-1}\text{W}^{-1}$] calculated within the bound mode (BMT) and our (RSE) theories at the pump and side-bands spectral positions. The spectral positions (wavelengths) of the side-bands correspond to the initial pulse power of $P_1 = 3.1 \text{ MW}$.

APPROACH		PUMP	STOKES	ANTI-STOKES
γ_{jl}	l	$\lambda_1 = 470 \text{ nm}$	$\lambda_3 = 541.1 \text{ nm}$	$\lambda_4 = 415.5 \text{ nm}$
RSE	1	8.472×10^{-6}	1.448×10^{-5}	1.905×10^{-5}
		$-4.581 \times 10^{-9}i$	$-1.497 \times 10^{-8}i$	$-2.187 \times 10^{-9}i$
	2	1.694×10^{-5}	1.448×10^{-5}	1.905×10^{-5}
		$-9.162 \times 10^{-9}i$	$-1.497 \times 10^{-8}i$	$-2.187 \times 10^{-9}i$
	3	1.667×10^{-5}	7.125×10^{-6}	1.874×10^{-5}
		$-8.798 \times 10^{-9}i$	$-7.200 \times 10^{-9}i$	$-2.101 \times 10^{-9}i$
	4	1.684×10^{-5}	1.439×10^{-5}	9.468×10^{-5}
		$-9.025 \times 10^{-9}i$	$-1.476 \times 10^{-8}i$	$-1.077 \times 10^{-9}i$
BMT	1	8.465×10^{-6}	1.446×10^{-5}	1.904×10^{-5}
	2	1.693×10^{-5}	1.446×10^{-5}	1.904×10^{-5}
	3	1.665×10^{-5}	7.118×10^{-6}	1.873×10^{-5}
	4	1.683×10^{-5}	1.438×10^{-5}	9.467×10^{-5}

Table 4.3. The partially degenerate nonlinearity parameters γ_{jl} [in $\text{m}^{-1}\text{W}^{-1}$] calculated within the bound mode (BMT) and our (RSE) theories at the pump and side-bands spectral positions. The spectral positions (wavelengths) of the side-bands correspond to the initial pulse power of $P_1 = 3.2 \text{ MW}$.

APPROACH		PUMP	STOKES	ANTI-STOKES
γ_{jlpq}		$\lambda_1 = 470 \text{ nm}$	$\lambda_3 = 541.1 \text{ nm}$	$\lambda_4 = 415.5 \text{ nm}$
RSE		1.675×10^{-5}	1.455×10^{-5}	1.895×10^{-5}
		$-1.145 \times 10^{-9}i$	$-8.405 \times 10^{-9}i$	$-1.095 \times 10^{-8}i$
BMT		1.674×10^{-5}	1.454×10^{-5}	1.894×10^{-5}
		$-1.522 \times 10^{-8}i$	$1.322 \times 10^{-8}i$	$-1.622 \times 10^{-8}i$

Table 4.4. The nondegenerate nonlinearity parameters γ_{jlpq} [in $\text{m}^{-1}\text{W}^{-1}$] calculated within the bound mode (BMT) and our (RSE) theories at the pump and side-bands spectral positions. The spectral positions (wavelengths) of the side-bands correspond to the initial pulse power of $P_1 = 3.2 \text{ MW}$.

$\tilde{\alpha}(\lambda)$ parts of the propagation constant $\beta(\lambda)$ around the corresponding waves are approximated by Taylor series expansions up to $\tilde{\beta}^{(4)}$ and $\tilde{\alpha}^{(2)}$ as the fourth and second order, respectively. As we can see in Fig. 4.4,

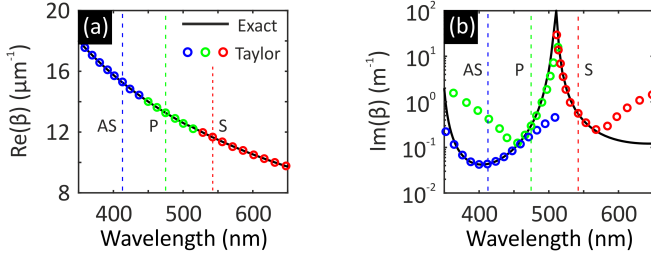


Figure 4.4. The Taylor series expansion of (a) the real $\tilde{\beta}(\lambda)$ and (b) the imaginary $\tilde{\alpha}(\lambda)$ parts of the propagation constant $\beta(\lambda)$ of the fundamental leaky mode of the annulus fiber [see Fig. 4.1] around the pump, the Stokes, and the anti-Stokes positions. They are approximated by truncating the corresponding series at $\tilde{\beta}^{(4)}$ and $\tilde{\alpha}^{(2)}$ as the fourth and second order, respectively. The spectral positions of the pump (P, green colour), the Stokes (S, red colour), and the anti-Stokes (AS, blue colour) waves are $\lambda_1 = 470$ nm, $\lambda_3 = 540.6$ nm, and $\lambda_4 = 415.8$ nm, respectively, that correspond to the initial power of $P_1 = 3.1$ MW.

the fourth order approximation for the real part of $\beta(\lambda)$, i.e., for the dispersion yields near identical results to the exact curve. Moreover, the expansion around each wavelength can accurately cover the entire wavelength window. However, the imaginary part of $\beta(\lambda)$ that corresponds to the modal loss can reproduce the exact curve in a smaller wavelength range. Unfortunately, due to the exponential dependence of the loss on wavelength, adding other higher-order terms of the expansion is not so efficient. Nevertheless, the approximation can be used since the pump, the Stokes, and the anti-Stokes waves are widely separated and narrow-band. Moreover, in the literature, mostly, the modal losses are assumed to be the same (constant) for all wavelengths [5]. Furthermore, in the numerical simulations, we assume that the pump, Stokes, and anti-Stokes wavelengths have the same group velocities $v_g \equiv 1/\beta^{(1)}$. Indeed, as one can see in Fig. 4.5, they have nearly the same group velocities and the relative difference of v_g between them is less than $\Delta v_g/v_g < 10^{-5}$.

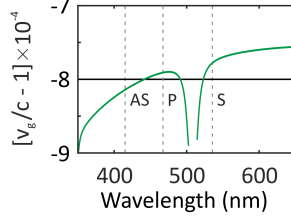


Figure 4.5. Spectral distribution of the group velocity $v_g \equiv 1/\beta^{(1)}$ (respect to the speed of light c) of the fundamental leaky mode of the annulus fiber shown in Fig. 4.1. The gray vertical dashed lines indicate the spectral positions of the pump (P), the Stokes (S) and the anti-Stokes (AS) waves at $\lambda_1 = 470$ nm, $\lambda_3 = 540.6$ nm, and $\lambda_4 = 415.8$ nm, respectively. The side bands positions correspond to the initial power of $P_1 = 3.1$ MW.

The initial amplitudes for the Stokes A_3 and anti-Stokes A_4 waves are given by

$$A_{3,4}(z = 0, t) = P_{3,4}^{1/2} \operatorname{sech}\left(\frac{t}{T_0}\right) e^{\mp i\Omega_s t}, \quad (4.58)$$

where $P_{3,4} \ll P_1$ and the "-" sign is for A_3 . We choose $P_{3,4}$ such that a seed for the Stokes and anti-Stokes waves at the corresponding frequencies is at the level of the spectral background (noise) of the pump field [see Fig. 4.6].

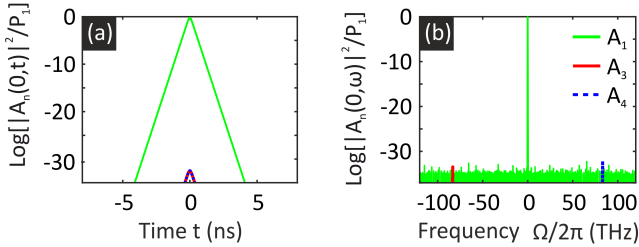


Figure 4.6. Initial profile of the pump Eq. (4.57), the Stokes, and the anti-Stokes amplitudes Eq. (4.58) in (a) time and (b) frequency domain for $P_1 = 3.1$ MW, $\Omega_s = 522.9$ THz, $T_0 = 100$ ps, and $P_3 = P_4 = 10^{-26}$ W.

The numerical solution of Eqs. (4.39a) to (4.39d) is carried out by using an improved version of the well-known split-step-Fourier method [see Section 3.5] [5, 80, 81]. In our numerical simulations, we use $N = 2^{22}$ points to discretize a time window of $T_{\text{Span}} = 100 T_{\text{FWHM}}$. These parameters provide the wavelength window of $\lambda_{\text{Span}} = cN/T_{\text{Span}} \sim 320 - 770$ nm according to the sampling theorem, which entirely covers the spectral range of our interest. The longitudinal step size used in numerical simulations is $\Delta z = 40 \mu\text{m}$.

4.5 RESULTS AND DISCUSSION

In this section, we investigate the pulse dynamics for two cases. In the first case, we consider the so-called continuous-wave regime that allows to consider only the nonlinear part of Eqs. (4.39a) to (4.39d), while in the second case, we solve the full system of equations including the dispersion and nonlinear effects.

4.5.1 Quasicontinuous-wave regime

Let us start our analysis by considering the simplified case, i.e., namely continuous-wave or quasicontinuous-wave regime. This regime supposes the propagation of pulses with relatively wide width that is around $T_0 \sim 1$ ns. Hence, dispersion effects can be neglected and we solve equations Eqs. (4.39a) to (4.39d) without dispersion operator \hat{D}_j . In our simulations, we consider the pump pulse at wavelength $\lambda_1 = 470$ nm with power of $P_1 = 3.1$ MW and $P_1 = 3.2$ MW. As an initial power for the side bands, we use $P_3 = P_4 = 10^{-26}$ W and the wave-vector mismatch is assumed to be $\Delta\bar{\beta} = -2\gamma_r P_1$.

The simulation results are displayed in Fig. 4.7. It shows the total power of the pump (P_1), Stokes (P_3) and anti-Stokes (P_4) waves normalized to the initial power of the pump wave as a function of propagation distance z . The red solid lines indicate the power calculated by using our formulation (RSE) while the blue dashed lines express the results based on the bound-mode theory (BMT). In the left column [panels (a), (c) and (e)], we display the results for the initial pump power of $P_1 = 3.1$ MW. As we can see, the efficient generation of the Stokes and the anti-Stokes bands occurs roughly after propagating along $z = 80$ cm length of the fiber. Subsequently, we observe a continuous exchange of power between the pump and the side-bands. The period of the ex-

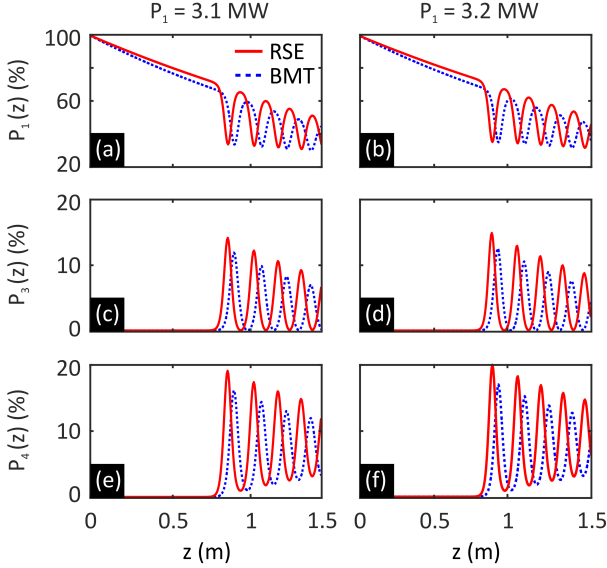


Figure 4.7. Four-wave mixing in the quasicontinuous-wave regime. Normalized pump [panels (a) and (b)], the Stokes [panels (c) and (d)] and the anti-Stokes [panels (e) and (f)] power as a function of propagation distance obtained by using our theory based on the resonant-state expansion (red solid line) and the bound-mode theory (blue dashed line) for initial pump powers of 3.1 MW (left column) and 3.2 MW (right column).

change, i.e., distance between two consequent maxima, is not constant. During the propagation, it becomes shorter differently for different theories. Furthermore, in our case, the Stokes and anti-Stokes bands occur a bit (roughly 4 cm) earlier than in the bound-mode theory. Due to these facts, there is a shift between the curves that correspond to different theories. For instance, they become nearly out of "phase" at $z = 1.44$ m, i.e., the Stokes and anti-Stokes bands have a local maximum power in our theory, while they have a local minimum power in the bound-mode theory. Additionally, we can note that in our formulation, the Stokes and anti-Stokes bands exhibit a higher maximum power. For instance, in our case the maximum efficiency of the Stokes and the anti-Stokes bands generation is 14.9 % and 19.4 %, respectively, while it is 12.3 % and 16.8 %, respectively, in the bound-mode theory. However,

it reduces at long distances, which is due to the pump depletion and modal losses.

We obtain very similar results for the initial pump power of $P_1 = 3.2$ MW (the right column of Fig. 4.7). Increasing the initial pump power leads to generation of Stokes and anti-Stokes bands with a higher power. Furthermore, the side-band generation arises a bit earlier in both formulations. For example, for $P_1 = 3.2$ MW, it is roughly 2 cm shorter than the previous case.

4.5.2 *Ultrafast regime*

Let us now simulate Eqs. (4.39a) to (4.39d) in the ultrafast regime that requires the inclusion of dispersion effects. In this case, we start our analysis of the pulse dynamics by investigating the total power spectral density $S(\lambda)$. Panel (a) in Fig. 4.8 depicts $S(\lambda)$ dynamics based on our formulation for the initial pump power of $P_1 = 3.1$ MW, while the results in panel (b) are based on the bound-mode theory. Note that the final equations become similar for both cases. The main difference is in the definition of the nonlinearity parameters. In the first case, the nonlinearity parameter γ has a negative imaginary part in contrast to the latter [see Fig. 4.3 (d)]. In addition, reciprocal conjugation is replaced by complex conjugation in the bound-mode theory. More details about the difference between two models can be found at the end of Section 4.2. By comparing panels (a) and (b) of Fig. 4.8, we clearly see that our formulation yields substantially more pronounced side bands. This is a substantial effect, considering that $\text{Im}(\gamma)/\text{Re}(\gamma)$ is rather small. Due to the higher modal loss at the Stokes position ($\lambda_3 = 540.6$ nm) compared to the anti-Stokes one ($\lambda_4 = 415.8$ nm), the power spectral density of the Stokes wave is rather small [see Fig. 4.3 (b)]. Please note that we use a broken power axis to show the side bands clearly.

Let us now repeat our simulations for a higher initial pump power of $P_1 = 3.2$ MW for the same pump wavelength. In this case, the positions of the side bands are slightly shifted according to the phase-matching condition [see Fig. 4.3 (e)]. However, they are still in the normal dispersion regime and all other parameters are close to those of the previous case. As we can see in panels (c) and (d) of Fig. 4.8, the Stokes and anti-Stokes bands are generated with a higher power spectral density. Specifically, the increment in $S(\lambda)$ is larger for the bound-mode theory [e.g., compare the anti-Stokes band in panels (b) and (d)] than in our formulation based on the resonant-state expansion [e.g., compare

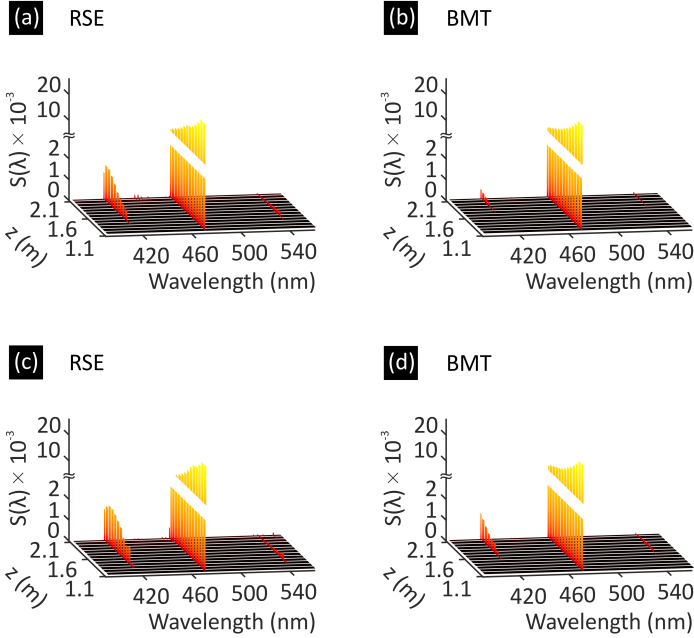


Figure 4.8. Four-wave mixing in the ultrafast regime. Spatial-spectral evolution of the total power-spectral-density $S(\lambda)$ obtained by using our theory based on the resonant-state expansion and the bound-mode theory for an initial pump power of 3.1 MW [panels (a) and (b)] and 3.2 MW [panels (c) and (d)], respectively.

the anti-Stokes band in panels (a) and (c)]. The reason for the latter is that the impact of the nonlinear gain contribution [i.e., terms proportional to $\text{Im}(\gamma)|A_1|^2$] to the side-band generation is decreasing due to the strong pump power ($P_1 \propto |A_1|^2$) depletion when using the resonant-state expansion. Moreover, the spectral broadening of the pump and side bands and their interaction generates various new frequencies, giving rise to supercontinuum generation at larger propagation distances. Therefore, in Fig. 4.8, we have truncated the nonlinear pulse dynamics around $z = 2.1$ m.

Now, let us consider the efficiency of the side-band generation. For that, we calculate the total power of each waves by integrating the cor-

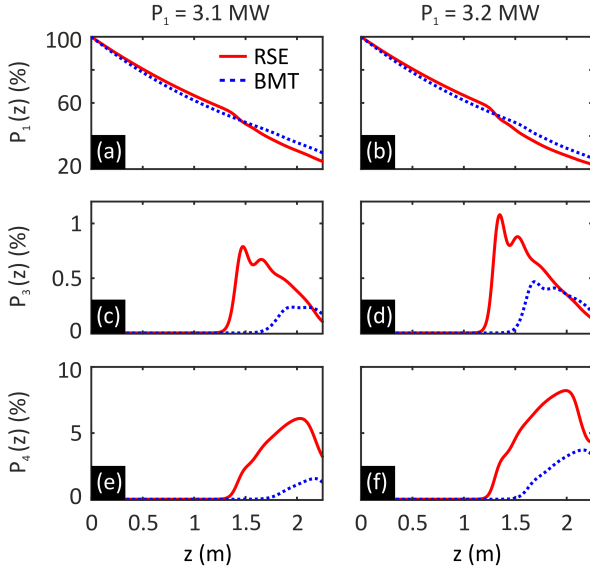


Figure 4.9. Four-wave mixing in the ultrafast regime. Normalized pump [panels (a) and (b)], the Stokes [panels (c) and (d)] and the anti-Stokes [panels (e) and (f)] power as a function of propagation distance obtained by using our theory based on the resonant-state expansion (red solid line) and the bound-mode theory (blue dashed line) for initial pump powers of 3.1 MW (left column) and 3.2 MW (right column).

responding total power spectral density $S(\lambda)$ over wavelength for each step of propagation. In Fig. 4.9, we plot the total power of the pump (P_1), Stokes (P_3) and anti-Stokes (P_4) waves normalized to the initial total power of the pump wave as a function of propagation distance z . The red solid lines indicate the power calculated by using our formulation, while the blue dashed lines express the results based on the bound-mode theory. In the left column [panels (a), (c) and (e)], we display the results for the initial pump power of $P_1 = 3.1$ MW. First, we clearly recognize that in our formulation, the Stokes and anti-Stokes bands exhibit at least two times more maximum power. Second, the most interesting point is that in our case, the Stokes and anti-Stokes bands occur roughly 50 cm earlier than in the bound-mode theory. An efficient power transfer from the pump to the side bands is observed

around $z = 1.5$ m, where the pump power sharply starts to decrease. Furthermore, we can see an oscillatory behavior of their total power over distance, which is clearly pronounced in the case of the Stokes band and relates an exchange of power between the two excitations.

The situation for the initial pump power of $P_1 = 3.2$ MW (the right column) is very similar to the previous case. As a main difference, we note the following: Increasing the initial pump power leads to a generation of Stokes and anti-Stokes bands with higher power within the phase-matching condition. Besides, the onset of the side-band generation arises earlier in both formulations. For example, for $P_1 = 3.2$ MW, the onset is roughly 20 cm earlier than in the previous case. Finally, the side bands decay at long distances, which might be due to the pump depletion and modal losses.

In conclusion, we have presented here a new and general theoretical formulation for a rigorous description of four-wave mixing in waveguide geometries. The formulation is based on the so-called resonant-state expansion with analytic mode normalization, which allows to consider both bound and leaky modes within a single framework. For a proof-of-concept analysis and as an example system, we have applied our theory to a gas-filled hollow-core annulus fiber. The numerical results reveal that our new formulation predicts a more efficient generation of the Stokes and anti-Stokes bands with an earlier onset for the leaky mode system in comparison with the bound-mode theory. Our findings originate from an accurate description of the nonlinear properties and in particular of the nonlinearity parameter of the considered waveguide.

~

DIPOLE EMISSION IN HOLLOW-CORE FIBERS

In nano-optics, dipole emitters coupled to optical resonators and waveguides have important applications in different areas such as spectroscopy [103, 104], sensing [105], plasmonics [106, 107], single-photon sources [108, 109], and nanolasers [110]. In these applications, wide tuning capabilities of hollow-core fibers can be useful for enhancing the emission power of the dipole. For instance, the holes of the fiber can be filled with different chemical and biological materials, which makes hollow-core fibers a great platform for sensing applications. Therefore, in this chapter, we apply the resonant-state expansion to model the dipole emission in hollow-core fibers. At first, we derive the total electromagnetic fields of an oscillating dipole in a waveguide by using the Green's dyadic and the reciprocity principle. After this, we investigate the change of the spontaneous emission rate of a dipole in hollow-core fibers.

It is placing an emitter in an optical resonator or waveguide that leads to a change of its spontaneous emission rate due to an interaction with the electromagnetic resonances of the optical system. This phenomenon is known as the Purcell effect [111]. It is characterized by the self-titled factor that is defined as the ratio of the spontaneous emission rate of a dipole in an electromagnetic environment to the free space one and can be approximated as [111]:

$$F_P = \frac{6\pi c^3 Q_m}{n_{\text{sur}}^3 \omega^3 V_m}. \quad (5.1)$$

Here, Q_m is the quality factor of the resonator mode, V_m is the mode volume and n_{sur} is the refractive index of the material surrounding the dipole that oscillates with frequency ω . In Eq. (5.1), the mode volume V_m can be written as [50, 52]

$$V_m = \frac{\int_V \varepsilon(\mathbf{r}) \mathbf{E}_m^2(\mathbf{r}) d\mathbf{r}}{[\mathbf{p}_o \cdot \mathbf{E}_m(\mathbf{r}_d)]^2}, \quad (5.2)$$

where \mathbf{p}_o and \mathbf{r}_d are the position and the polarization vector of the dipole, respectively. The integral in the numerator of Eq. (5.2) is the normalization constant of the electric field \mathbf{E} of the mode. As we have

discussed in Section 2.3, this normalization diverges in the case of the open resonators because of the energy leakage. Thus, the mode volume and hence the Purcell factor are not correctly defined for open systems. However, the authors in Ref. [50] have solved this issue and presented an exact analytic theory of the Purcell effect that can be applied for open three-dimensional (3D) resonators. Using the Green's dyadic $\mathbf{G}_k(\mathbf{r}, \mathbf{r}')$ Eq. (2.42) and the correct mode normalization constant N_m Eq. (2.46), the Purcell factor in the weak coupling can be written as [50]

$$F_P = \frac{3\pi c^3}{\omega} \sum_m \text{Im} \frac{[\mathbf{p}_o \cdot \mathbf{E}_m(\mathbf{r}_d)]^2}{N_m \omega_m (\omega_m - \omega)}, \quad (5.3)$$

where ω_m are the eigenfrequencies of the modes.

The change of the dipole emission in conventional step-profile optical fibers, i.e., in two-dimensional (2D) systems (i.e., 3D systems translational invariant in one direction) with bound modes has been modelled within different approximations in literature [28, 112–114], as well as the fluorescence of isotropic and homogeneously distributed emitters in microstructured fibers in the single mode approximation [115–117]. It has been theoretically and experimentally shown that the spontaneous emission rate and the radiation pattern of emitters change near an interface between two different materials [113, 114, 118, 119].

To the best of our knowledge, the modelling of the dipole emission in hollow-core optical fibers with leaky modes is missing so far. In the following sections, we try to tackle this issue within our theory. For that, first of all, we derive the fields generated by an oscillating point dipole by using the Green's dyadic of Section 2.2.2 for waveguide geometries. Next, we show that the fields can be obtained directly from the reciprocity principle.

5.1 DIPOLE FIELDS IN FIBERS

The Purcell factor can also be defined as the ratio of the power P radiated by a dipole in the resonator to the power $P_o = \omega^4 |\mathbf{p}_o|^2 / (3c^3)$ radiated in an homogeneous medium, i.e., $F_P = P/P_o$ [120]. Therefore, in this section, we derive the total electromagnetic field of a dipole located in optical waveguides including hollow-core fibers. As we have shown in Chapter 2, the fields generated by an arbitrary source in a waveguide can be obtained by using the Green's dyadic that is decomposed into the waveguide's resonant states. Hence, in the following subsection, we derive the electromagnetic fields of a dipole based on this approach.

5.1.1 Dipole fields from the Green's dyadic

The Green's dyadic in real space is given by [see Section 2.2.2]

$$\mathbf{G}(\mathbf{r}, \mathbf{r}'; \omega) = \sum_m \frac{\mathbf{F}_m(\mathbf{r}_{||}; \omega) \otimes \mathbf{F}_m^{\mathbf{R}}(\mathbf{r}'_{||}; \omega)}{2iN_m} e^{i\beta_m|z-z'|}. \quad (5.4)$$

Based on this, we can calculate the field \mathbf{F} generated by an arbitrary source \mathbf{J} in the waveguide as

$$\mathbf{F}(\mathbf{r}; \omega) = \sum_m \frac{\mathbf{F}_m(\mathbf{r}_{||}; \omega)}{2iN_m} \int \mathbf{F}_m^{\mathbf{R}}(\mathbf{r}'_{||}; \omega) \cdot \mathbf{J}(\mathbf{r}'; \omega) e^{i\beta_m|z-z'|} d\mathbf{r}'. \quad (5.5)$$

In Eq. (5.5), as a source we consider an oscillating point dipole with dipole moment \mathbf{p}_o and frequency ω_o , located at $\mathbf{r}_o = (x_o, y_o, z_o)$. The corresponding electric current density of the dipole is:

$$\mathbf{J}_{\mathbf{E}}(\mathbf{r}; t) = -\frac{4\pi i}{c} \mathbf{j}(\mathbf{r}) e^{-i\omega_o t}, \quad (5.6)$$

where $\mathbf{j}(\mathbf{r}) = \mathbf{j}_o \delta(\mathbf{r} - \mathbf{r}_o)$, and $\mathbf{j}_o = \mathbf{p}_o \omega_o$. The transformation into the frequency domain provides

$$\mathbf{J}_{\mathbf{E}}(\mathbf{r}; \omega) = -\frac{8\pi^2 i}{c} \mathbf{j}_o \delta(\mathbf{r} - \mathbf{r}_o) \delta(\omega - \omega_o). \quad (5.7)$$

Thus, the field \mathbf{F} generated by this point source can be written as

$$\mathbf{F}(\mathbf{r}; \omega) = \sum_m a_m(z, \omega) \mathbf{F}_m(\mathbf{r}_{||}; \omega), \quad (5.8)$$

where a_m is the mode amplitude given by

$$a_m(z, \omega) = -\frac{4\pi^2}{cN_m} \left[\mathbf{E}_m^{\mathbf{R}}(x_o, y_o; \omega) \cdot \mathbf{j}_o \right] e^{i\beta_m|z-z_o|} \delta(\omega - \omega_o). \quad (5.9)$$

Finally, the Fourier transformation into the time-domain provides:

$$\begin{aligned} \mathbf{F}(\mathbf{r}; t) = & -\sum_m \frac{4\pi^2 \omega_o}{cN_m} \left[\mathbf{E}_m^{\mathbf{R}}(x_o, y_o; \omega_o) \cdot \mathbf{p}_o \right] \\ & \times \mathbf{F}_m(\mathbf{r}_{||}; \omega_o) e^{i\beta_m|z-z_o|} e^{-i\omega_o t}. \end{aligned} \quad (5.10)$$

Note that here \mathbf{F} stands for the electric \mathbf{E} and the magnetic \mathbf{H} fields.

5.1.2 Dipole fields from the reciprocity principle

In this section, the reciprocity principle is used to derive the electromagnetic fields of sources in optical waveguides including hollow-core fibers that are dominated by leaky modes. Note that this derivation is an alternative to the previous one, which is based on the Green's dyadic.

Let us start by considering the following equations:

$$\hat{\mathbb{M}}(\mathbf{r}_{\parallel}, \beta; \omega) \hat{\mathbf{F}}(\mathbf{r}_{\parallel}, \beta; \omega) = \hat{\mathbf{J}}(\mathbf{r}_{\parallel}, \beta; \omega), \quad (5.11)$$

$$\hat{\mathbb{M}}(\mathbf{r}_{\parallel}, -\beta_m; \omega) \hat{\mathbf{F}}_m^{\mathbf{R}}(\mathbf{r}_{\parallel}; \omega) = 0. \quad (5.12)$$

First, we multiply Eq. (5.11) with $\hat{\mathbf{F}}_m^{\mathbf{R}}$ and Eq. (5.12) with $\hat{\mathbf{F}}$ from the left side and then subtract the second expression from the first one. By using Eq. (2.30), the resulting expression can be simplified to the form

$$\left[\nabla_{\parallel} + i(\beta - \beta_m) \hat{\mathbf{e}}_z \right] \cdot \left[\hat{\mathbf{E}}(\mathbf{r}_{\parallel}, \beta; \omega) \times \hat{\mathbf{H}}_m^{\mathbf{R}}(\mathbf{r}_{\parallel}; \omega) - \hat{\mathbf{E}}_m^{\mathbf{R}}(\mathbf{r}_{\parallel}; \omega) \times \hat{\mathbf{H}}(\mathbf{r}_{\parallel}, \beta; \omega) \right] = i \hat{\mathbf{E}}_m^{\mathbf{R}}(\mathbf{r}_{\parallel}; \omega) \cdot \hat{\mathbf{J}}_{\mathbf{E}}(\mathbf{r}_{\parallel}, \beta; \omega), \quad (5.13)$$

where $\hat{\mathbf{e}}_z$ denotes the unit vector in the z direction.

Next, we make the ansatz that the fields $\hat{\mathbf{E}}$ and $\hat{\mathbf{H}}$ can be expressed as a superposition of resonant states $\hat{\mathbf{E}}_n$ and $\hat{\mathbf{H}}_n$, respectively, and assume that the source term $\hat{\mathbf{J}}_{\mathbf{E}}$ vanishes at the resonances:

$$\hat{\mathbf{E}}(\mathbf{r}_{\parallel}, \beta; \omega) = \sum_n \hat{a}_n(\beta; \omega) \hat{\mathbf{E}}_n(\mathbf{r}_{\parallel}; \omega), \quad (5.14)$$

$$\hat{\mathbf{H}}(\mathbf{r}_{\parallel}, \beta; \omega) = \sum_n \hat{a}_n(\beta; \omega) \hat{\mathbf{H}}_n(\mathbf{r}_{\parallel}; \omega), \quad (5.15)$$

$$\hat{\mathbf{J}}_{\mathbf{E}}(\mathbf{r}_{\parallel}, \beta; \omega) = \prod_n (\beta - \beta_n) \hat{\xi}_n(\mathbf{r}_{\parallel}; \omega). \quad (5.16)$$

Here, \hat{a}_n is the amplitude of the resonant state and ξ is an arbitrary function. Hereinafter, for the sake of brevity, we omit the \mathbf{r}_{\parallel} and ω dependencies in the equations. Substituting Eqs. (5.14) to (5.16) into Eq. (5.13) and integrating over the spatial inhomogeneities, we obtain:

$$\sum_n \int \hat{a}_n \left[\nabla_{\parallel} + i(\beta - \beta_m) \hat{\mathbf{e}}_z \right] \cdot \left(\hat{\mathbf{E}}_n \times \hat{\mathbf{H}}_m^{\mathbf{R}} - \hat{\mathbf{E}}_m^{\mathbf{R}} \times \hat{\mathbf{H}}_n \right) d\mathbf{r}_{\parallel} = i(\beta - \beta_m) \int \hat{\mathbf{E}}_m^{\mathbf{R}} \cdot \prod_{n \neq m} (\beta - \beta_n) \hat{\xi}_n d\mathbf{r}_{\parallel}. \quad (5.17)$$

In the limit $\beta \rightarrow \beta_n$ ($\beta_n \neq \beta_m$), Eq. (5.17) yields the following orthogonality relation for the resonant states:

$$\lim_{\beta \rightarrow \beta_n} \int \sum_n \hat{a}_n \left[\frac{\nabla_{\parallel}}{i(\beta - \beta_m)} + \hat{\mathbf{e}}_z \right] \cdot \left(\hat{\mathbf{E}}_n \times \hat{\mathbf{H}}_m^{\text{R}} - \hat{\mathbf{E}}_m^{\text{R}} \times \hat{\mathbf{H}}_n \right) d\mathbf{r}_{\parallel} = 0. \quad (5.18)$$

In the limit $\beta \rightarrow \beta_m$, the integral on the right hand side of Eq. (5.17) is defined as the normalization coefficient N_m [see also Section 2.4] [A1]. Hence, we can combine the orthogonality and normalization conditions as following:

$$\lim_{\beta \rightarrow \beta_n} \int \sum_n \hat{a}_n \left[\frac{\nabla_{\parallel}}{i(\beta - \beta_m)} + \hat{\mathbf{e}}_z \right] \cdot \left(\hat{\mathbf{E}}_n \times \hat{\mathbf{H}}_m^{\text{R}} - \hat{\mathbf{E}}_m^{\text{R}} \times \hat{\mathbf{H}}_n \right) d\mathbf{r}_{\parallel} = -2N_m \delta_{mn}. \quad (5.19)$$

Now, let us define the mode amplitudes $\hat{a}_m(\beta)$. The assumption that $\hat{\mathbf{J}}(\beta) \rightarrow 0$, and, accordingly, $\hat{\mathbf{F}}(\beta) \rightarrow \hat{\mathbf{F}}_m$ in the limit $\beta \rightarrow \beta_m$ results in $\hat{a}_m(\beta) \rightarrow \hat{a}_m(\beta_m) = 1$, i.e.,

$$\hat{a}_m(\beta_m) = -\frac{1}{2N_m} \int \hat{\mathbf{E}}_m^{\text{R}} \cdot \prod_{n \neq m} (\beta_m - \beta_n) \hat{\sigma}_n d\mathbf{r}_{\parallel} = 1. \quad (5.20)$$

Introducing an analytical continuation $\hat{a}_m(\beta)$ of $\hat{a}_m(\beta_m)$ in the complex β plane around the $\beta = \beta_m$ point, we can write

$$\hat{a}_m(\beta) = -\frac{1}{2N_m} \int \hat{\mathbf{E}}_m^{\text{R}} \cdot \prod_{n \neq m} (\beta - \beta_n) \hat{\sigma}_n d\mathbf{r}_{\parallel}. \quad (5.21)$$

Using Eq. (5.16), the right hand side of Eq. (5.21) can be written as

$$\hat{a}_m(\beta) = -\frac{1}{2N_m} \int \frac{\hat{\mathbf{E}}_m^{\text{R}} \cdot \hat{\mathbf{J}}_{\text{E}}}{\beta - \beta_m} d\mathbf{r}_{\parallel}. \quad (5.22)$$

Now, we can Fourier transform back into the z space:

$$a_m(z) = -\iint \frac{\hat{\mathbf{E}}_m^{\text{R}} \cdot \hat{\mathbf{J}}_{\text{E}}}{2N_m(\beta - \beta_m)} e^{i\beta z} d\mathbf{r}_{\parallel} d\beta. \quad (5.23)$$

Representing $\hat{\mathbf{J}}_{\text{E}}$ in Eq. (5.23) as

$$\hat{\mathbf{J}}_{\text{E}} = \frac{1}{2\pi} \int \mathbf{J}_{\text{E}} e^{-i\beta z} dz, \quad (5.24)$$

we obtain:

$$\begin{aligned}
 a_m(z) &= -\frac{1}{2\pi} \iiint \hat{\mathbf{E}}_m^{\mathbf{R}} \cdot \mathbf{J}_E \frac{e^{i\beta(z-z')}}{2N_m(\beta - \beta_m)} dz' d\beta d\mathbf{r}' = \\
 &\frac{1}{2iN_m} \int \mathbf{E}_m^{\mathbf{R}} \cdot \mathbf{J}_E e^{i\beta_m|z-z'|} d\mathbf{r}'. \quad (5.25)
 \end{aligned}$$

Note that the Fourier transform in Eq. (5.25) is evaluated in the same manner as in the case of the Green's dyadic [see Section 2.2.2]. Finally, multiplying Eq. (5.25) with \mathbf{F}_m and summing over m , we obtain an expression the total field, which is the same as Eq. (5.5):

$$\mathbf{F}(\mathbf{r}; \omega) = \sum_m \frac{\hat{\mathbf{F}}_m(\mathbf{r}_{||}; \omega)}{2iN_m} \int \mathbf{F}_m^{\mathbf{R}}(\mathbf{r}'_{||}; \omega) \cdot \mathbf{J}(\mathbf{r}'_{||}; \omega) e^{i\beta_m|z-z'|} d\mathbf{r}'. \quad (5.26)$$

In Eq. (5.26), we have replaced $\mathbf{E}_m^{\mathbf{R}}$ and \mathbf{J}_E with $\mathbf{F}_m^{\mathbf{R}}$ and \mathbf{J} , respectively. This does not change the final results since $\mathbf{J}_H \equiv \mathbf{0}$ in \mathbf{J} .

5.2 PURCELL FACTOR

The change of the dipole emission rate γ in an optical fiber relative to the free space one γ_o , i.e., the Purcell factor F_P [111] can be defined as [120]

$$F_P = \frac{\gamma}{\gamma_o}, \quad (5.27)$$

where

$$\gamma_o = \frac{2n_{\text{sur}}k_o^3|\mathbf{p}_o|^2}{3\hbar}. \quad (5.28)$$

Here, n_{sur} is the refractive index of surrounding homogeneous medium. The decay rate of a dipole in fiber can be expressed in terms of the Green's dyadic as [50, 120]

$$\gamma = -\frac{4\pi k_o|\mathbf{p}_o|^2}{\hbar} \left\{ \mathbf{n}_p \cdot \text{Im}[\mathbf{G}(\mathbf{r}, \mathbf{r}; \omega)] \cdot \mathbf{n}_p \right\}, \quad (5.29)$$

where \mathbf{n}_p is a unit vector in the direction of \mathbf{p}_o .

Thus, substituting Eq. (5.4) into Eq. (5.29), we obtain

$$F_P = \frac{3\pi}{n_{\text{sur}}k_o^2} \sum_m \text{Re} \left[\left(\mathbf{n}_p \cdot \mathbf{e}_m \right) \left(\mathbf{n}_p \cdot \mathbf{e}_m^{\mathbf{R}} \right) \right], \quad (5.30)$$

with $\mathbf{e}_m = \mathbf{E}_m/N_m^{1/2}$ being the normalized electric field of the fiber mode.

5.3 DIPOLE EMISSION IN HOLLOW-CORE FIBERS

In this section, we apply our approach to a dipole located in two different hollow-core optical fibers. The first geometry is a simple capillary fiber made of silica and filled with water. The second geometry is the so-called hollow-core wagon-wheel fiber [63, 116] that has three noncircular holes and one of them is filled with water. The schematic of the fibers as well as their geometrical and optical parameters are shown in panels (a) and (b) of Fig. 5.1. Additionally, panels (c) and (d) in Fig. 5.1 display the fundamental leaky modes of the fibers at the wavelength $\lambda_o = 590$ nm.

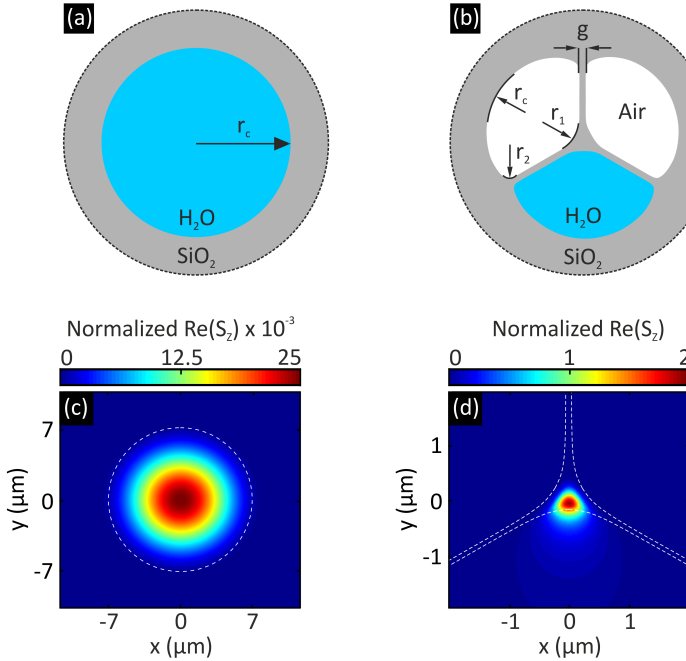


Figure 5.1. Schematic of the modelling hollow-core (a) step-profile and (b) wagon wheel fibers as well as their fundamental HE_{11} leaky modes [panels (c) and (d), respectively] at $\lambda_o = 590$ nm. The geometrical and optical parameters of the fibers are the following: $r_c = 7 \mu\text{m}$, $r_1 = 0.85 \mu\text{m}$, $r_2 = 1.5 \mu\text{m}$, $g = 0.1 \mu\text{m}$. The refractive index of air, H_2O and SiO_2 are $n = 1$, $n = 1.33$ and $n = 1.46$, respectively.

Here, one can note that the electromagnetic fields of the fundamental mode of the second geometry is highly confined and exhibits very high nonlinear properties [63]. Furthermore, one should note that these hollow-core fibers exhibit an infinite number of leaky modes [41, 58].

Let us now consider the hollow-core step-profile fiber that is shown in Fig. 5.1 (a). We assume that at the center of the fiber, we have an electric dipole that oscillates along the horizontal direction (i.e., in the direction of the x -axis) at the wavelength $\lambda_o = 590$ nm. Due to the symmetry of the system, among all transverse TE_{0n}/TM_{0n} and hybrid HE_{mn}/EH_{mn} modes, only the hybrid HE_{1n}/EH_{1n} modes with azimuthal number $m = 1$ can be excited. Here, we consider the first $N = 2500$ modes (among which 1248 and 1252 are EH_{1n} and HE_{1n} modes, respectively, see Fig. 5.4) that are sorted in ascending order according to the imaginary part of their propagation constant, i.e., their modal loss. Panel (a) in Fig. 5.2 shows the Purcell factor of each excited mode. As we can see, the modes with low loss are excited quite efficiently, while the Purcell factor of the higher order modes has an oscillatory behavior around zero. With increasing mode order, the amplitude of this oscillation diverges. At first glance, it seems that the oscillation becomes harmonic for the higher-order modes and hence, that when evaluating the sum over all contributions, the negative and positive Purcell factors of individual modes cancel each other. However, if we plot the convergence of the Purcell factor over the number of modes, which is shown in Fig. 5.2 (b), one can see that due to this oscillation the Purcell factor obtained with this method is not defined uniquely. For comparison, a full wave COMSOL Multiphysics simulations was performed, which provides a Purcell factor of $F_P = 1.12$ [green dashed line in Fig. 5.2 (b)].

Let us now take a look at the emission patterns. It is known that a dipole radiates perpendicularly to its oscillation direction [34]. Hence, since in our case, the dipole is oriented in the horizontal direction, we expect it to radiate vertically. The bottom panels (c) and (d) in Fig. 5.2 display the electric field of the dipole approximated by using $N = 60$ and $N = 400$ modes, respectively. In the first case ($N = 60$), as we can see, the radiation pattern shows the expected qualitative behavior. However, in the second case ($N = 400$), for which the Purcell factor from our approach and the full wave simulations are identical [see Fig. 5.2 (b)], the dipole does not radiates in vertical direction.

Pair of panels [(e), (f)] and [(g), (h)] in Fig. 5.2 depict the electric field of the dipole approximated by $N = 60$ and $N = 400$ modes, in the xy and yz planes, respectively. As we can see in panels (e) and (f), the

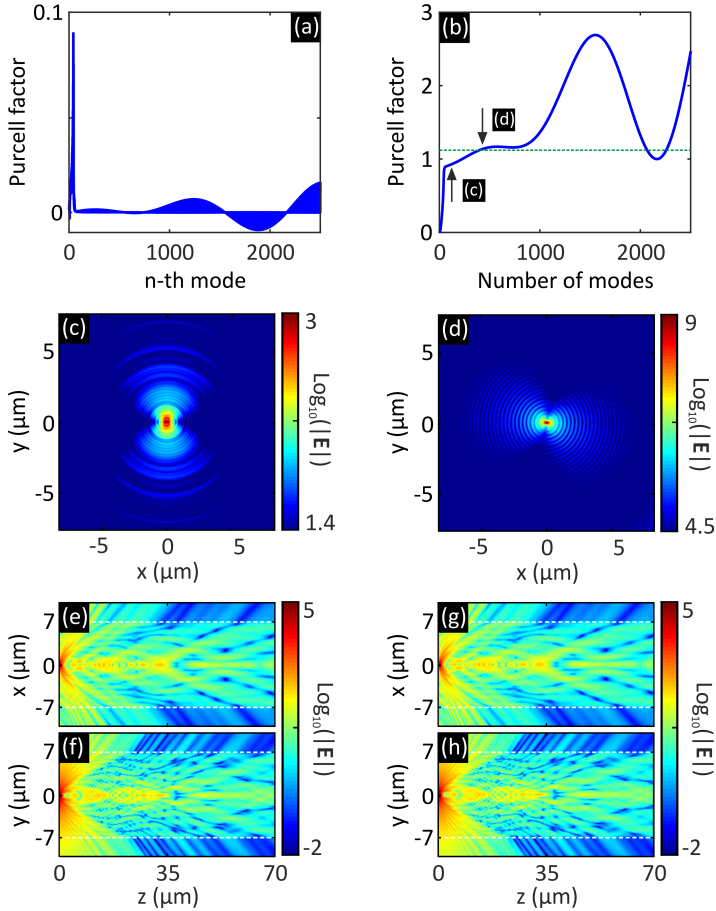


Figure 5.2. The Purcell factor of an horizontally oriented dipole (oscillating at $\lambda_o = 590$ nm) located at the center of the hollow-core step-profile fiber that is shown in Fig. 5.1 (a). Panel (a) displays the individual Purcell factor of each mode (HE_{1n}/EH_{1n}) while panel (b) shows the total Purcell factor as a function of the number of modes, i.e., the convergence. The green dashed line corresponds to the Purcell factor obtained from a full wave COMSOL Multiphysics simulation. The bottom panels (c) and (d) display the electric field of the dipole (at $z = 0$) approximated by $N = 60$ and $N = 400$ modes of the fiber, respectively. The corresponding points are indicated by black arrows in panel (b). Pair of panels [(e), (f)] and [(g), (h)] display the electric field of the dipole shown in panels (c) and (d) in the xz (at $y = 0$) and yz (at $x = 0$) planes, respectively. White dashed lines indicate the core-cladding interface. Note that in this system, only HE_{1n}/EH_{1n} modes are excited.

emission patterns in the xz and yz planes are different since the dipole radiates in the y direction. By comparing them with the emission patterns in the xy and yz planes for $N = 400$ [(g), (h)] modes, we see that they are almost identical. It is due to the fact that the higher-order modes have very high modal losses. For example, the propagation constant of HE_{130} and EH_{130} modes ($n = 30$) are $\beta = (0.554 + 6.519i) \mu\text{m}^{-1}$ and $\beta = (0.355 + 9.690i) \mu\text{m}^{-1}$, respectively. Hence, the fields of these and the following higher-order modes decrease more than 1000 times in a few nanometers of propagation along the z direction. Additionally, in Fig. 5.2 (e–h), we can clearly see the refraction of dipole radiation at the core-cladding interfaces (white dashed lines) into the cladding region.

As it is known from the literature, we can distinguish two types of hybrid modes, i.e., HE_{mn} and EH_{mn} modes [28, 41]. For these modes all six components of the electromagnetic fields are nonzero and the main difference between them is the following: In HE_{mn} modes, the longitudinal component of the electric field E_z dominates over the longitudinal component of the magnetic field H_z , while in EH_{mn} modes, this is vice versa. Therefore, in order to analyze the above issue, let us first consider the excited hybrid HE_{1n} and EH_{1n} modes individually.

Panels (a) and (b) in Fig. 5.3 display the Purcell factor of the n -th mode in the set of hybrid HE_{1n} modes and the convergence of the Purcell factor over the number of modes, respectively. As we can see, the amplitude of the oscillation is quite small and decreases with increasing n . However, the same analysis for EH_{1n} modes shows an opposite behavior, i.e., the amplitude of the oscillation becomes bigger for the higher-order modes. Thus, we see that the Purcell factor of HE_{1n} modes calculated by using Eq. (5.30) converges, but slowly, while for EH_{1n} modes our approach provides relatively good results if only the lower-order modes are considered.

Let us continue our analysis by considering the positions of the hybrid HE_{1n} and EH_{1n} modes in the complex effective refractive index $n_{\text{eff}} = \beta/k_0$ plane. As we know, they correspond to the poles of the Green's dyadic Eq. (2.36). In Fig. 5.4, the red crosses and the blue filled circles denote the HE_{1n} and EH_{1n} modes, respectively. The first quadrant (positive real and imaginary values) contains the poles with n_{eff} , while the third one (negative real and imaginary values) contains the poles with $-n_{\text{eff}}$ that exist due to the reciprocity [see also Fig. 2.1]. As we can see, the lower-order modes are located near the real axis, while the higher-order modes are close to the imaginary axis. Interestingly, the

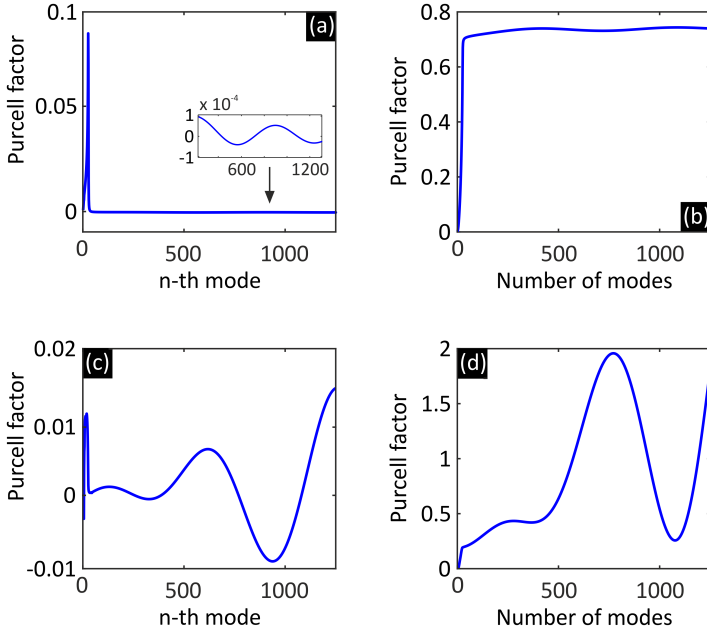


Figure 5.3. The Purcell factor of the horizontally oriented dipole (oscillating at $\lambda_0 = 590$ nm) located at the center of the hollow-core step-profile fiber that is shown in Fig. 5.1 (a). Panels (a) and (c) display the individual Purcell factor of each HE_{1n} and EH_{1n} mode, respectively, while panels (b) and (d) display the total Purcell factor as a function of the number of HE_{1n} and EH_{1n} modes, respectively.

higher-order hybrid HE_{1n} modes slowly move away from the imaginary axis with increasing mode number.

In contrast to 3D systems, the Green's dyadic Eq. (2.36) of 2D systems has a cut in the complex n_{eff} plane along the negative imaginary half axis [38, 39]. In Fig. 5.4, the position of the cut is indicated by the green solid line. This cut contribution occurs due to the first kind of Hankel function, which describes the mode fields in the exterior and it is not uniquely defined [62]. The latter can be easily identified by considering the boundary condition Eq. (2.15), which essentially describes the asymptotic behavior of the electromagnetic fields at $\rho \rightarrow \infty$. As we can

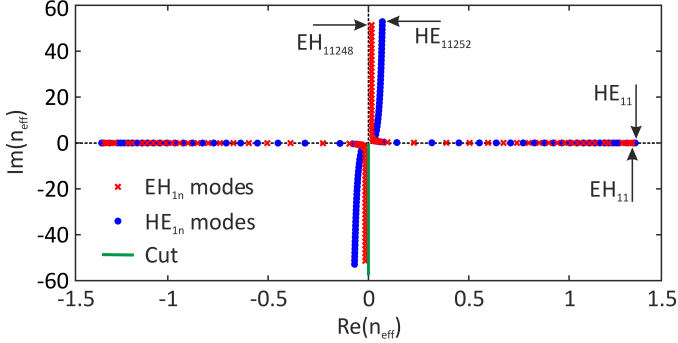


Figure 5.4. Poles of the Green's dyadic in the complex $n_{\text{eff}} = \beta/k_0$ plane that correspond to the HE_{1n} and EH_{1n} modes of the hollow-core step-profile fiber shown in Fig. 5.1 (a). The higher-order EH_{1n} modes are located very close to the cut of the Green's dyadic, while the HE_{1n} modes move away from the cut.

see in Eq. (2.15), it has a square-root in the denominator that has a cut in the complex plane. The presence of these cut contributions explains the issues related the divergence of the Purcell factor for the higher-order modes.

The cut contribution can be neglected if the poles and accordingly the waveguide modes are far from the cut. Therefore, we have obtained self-consistent results for the Purcell factor in case of HE_{1n} as well as lower-order EH_{1n} modes of hollow-core step-profile fiber that are far from the cut [see Fig. 5.4]. However, when the poles are close to the cut as in case of the higher-order EH_{1n} modes, the cut contribution in the Green's dyadic Eq. (2.19) has to be taken into account.

For the sake of completeness, let us briefly consider the second, so-called wagon-wheel fiber geometry. In contrast to the previous geometry, the symmetry of the system is broken due to the water-filled hole. In this case, we use COMSOL Multiphysics for calculating the fiber modes. In our COMSOL simulations, domain radius and the perfectly matched layer (PML) thickness are $12 \mu\text{m}$ and $2 \mu\text{m}$, respectively. For meshing, we have used the free triangular mesh with a minimum element size of $\lambda/(8n)$, where λ and n are the wavelength of interest and the refractive index of the medium, respectively. Furthermore, in COMSOL, it is hard to select only those modes that are excited by the dipole. Therefore, we consider only the first $N = 150$ modes with the lowest loss.

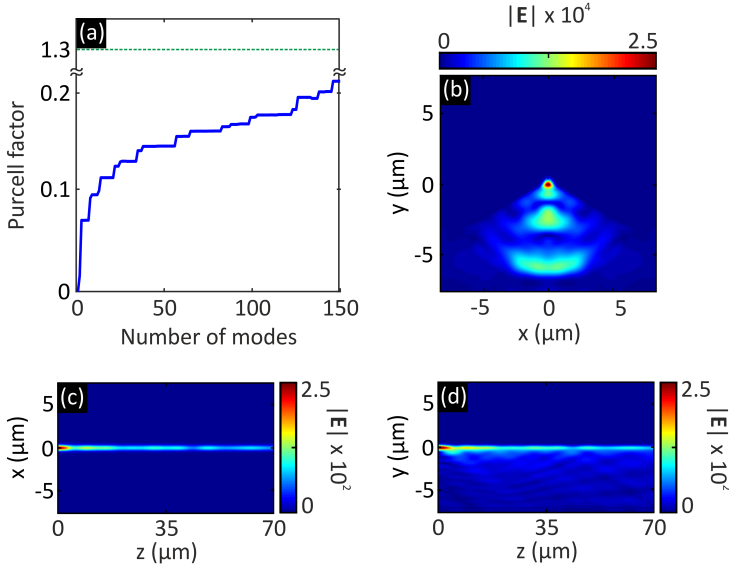


Figure 5.5. The Purcell factor of a horizontally oriented dipole (oscillating at $\lambda_o = 590$ nm) located at the center of the hollow-core wagon wheel fiber that is shown in Fig. 5.1 (b). Panel (a) displays the Purcell factor obtained with our modal approach (blue line) as a function of the number of modes. The green dashed line corresponds to the Purcell factor obtained from full-wave simulations. Panel (b) displays the electric field of the dipole (at $z = 0$) approximated by $N = 150$ modes of the fiber. The bottom panels (c) and (d) display the electric field of the dipole shown in panel (b), in the xz (at $y = 0$) and yz (at $x = 0$) planes, respectively. Note that in this case, we have used the first $N = 150$ modes with the lowest modal loss.

The simulation results are shown in Fig. 5.5. In panel (a), the blue line displays the resulting Purcell factor as a function of the number of modes. For comparison, the green dashed line indicates the Purcell factor that was obtained by full wave calculations (performed with COMSOL Multiphysics as well). As we can see, the Purcell factor of the modal approach converges quite slowly. Furthermore, not all modes are excited, which is why dependence in Fig. 5.5 (a) is not so smooth. The electric field of the dipole in the xy plane (at $z = 0$) approximated by $N = 150$ modes is shown in panel (b). Due to the asymmetry of the system, radiation occurs only in one direction. Finally, the radia-

tion patterns in the xz (at $y = 0$) and yz planes (at $x = 0$) are shown in Fig. 5.5 (c) and Fig. 5.5 (d), respectively. As we can see, the radiation is mostly confined in a small core region, i.e., between three holes. However, it partially refracts into the water-filled hole.

In this chapter, we have provided a model for the description of dipole emission in open waveguide systems. Our model is based on the resonant-state expansion with the correct mode normalization. We have derived the electromagnetic fields of a dipole in two different ways, namely by using the Green's dyadic and by relying on the reciprocity principle, as well as established an expression for the Purcell factor. Note that in our model, we have assumed that the so-called cut contribution in the Green's dyadic is negligible.

Based on this approach, we have calculated the change of the spontaneous emission rate of a dipole in two different kinds of hollow-core waveguide geometries. Our simulations show that for an accurate description it is necessary to take into account a relatively high number of excited waveguide modes. It turns out that in this case, some of the modes are close to the cut of the Green's dyadic and hence the cut contribution has to be considered in order to obtain accurate results. This will be a subject of future investigations.

~

CONCLUSION AND OUTLOOK

In conclusion, we have presented here a new theory for simulating the linear and nonlinear propagation of both bound and leaky mode in waveguides, including the more advanced and complex hollow-core fibers. The approach is based on a powerful and rigorous method, namely the resonant-state expansion, with an analytic mode normalization. The latter allows to apply the approach straightforwardly to different waveguide geometries and to restrict the computational domain to regions of spatial inhomogeneities giving substantial improvements in numerical simulations.

We have built our theory ab initio from the Maxwell's equations. Based on the concept of the Green's dyadic that can be represented as a sum over the correctly normalized eigensolutions of the system, we have derived a master equation. By considering the nonlinear polarization as the general source in this equation, we have obtained the nonlinear pulse propagation equation. This rigorous approach does not include any slowly varying amplitude approximation in contrast to the standard formulations and can be readily applied to both bound and leaky modes.

In the single-mode approximation, the master equation simplifies to the well-known nonlinear Schroedinger equation that includes a new definition for the Kerr nonlinearity parameter. Applying this equation for the description of the nonlinear pulse propagation in hollow-core fibers that are governed by leaky modes has revealed that the Kerr nonlinearity parameter has an imaginary part. While this was expected from previous works, we have found that, depending on the fiber parameters, the imaginary part can change its sign. If it is positive, it corresponds to nonlinear loss, while a negative imaginary part acts as a nonlinear gain for the overall attenuating pulses. The mechanism of the nonlinear gain can be explained by a self-focusing that reduces the pulse intensity at the interface of core and surrounding, which in turn decreases the energy dissipation through to exterior. Our numerical simulations for the pulse propagation in a capillary fibers demonstrate that it can have significant influence on the spectral and temporal evolution of an ultrashort pulse.

Our theory is neither restricted to simple waveguide geometries nor to the single-mode approximation, within which usually the spectral broadening of the initial pulse, also known as supercontinuum generation, is investigated. It can be easily applied to more complex waveguide geometries such as Kagomé fibers, and it can be extended to other nonlinear processes such as four-wave mixing.

In order to demonstrate this, we have used our theory to derive a rigorous description of four-wave mixing in waveguide geometries, which allows consideration of both bound and leaky modes within a single framework. For a proof-of-concept analysis and as an example system, we have applied our theory to a relatively complex gas-filled hollow-core annulus fiber. The numerical simulations reveal that our theory predicts a more efficient generation of the Stokes and anti-Stokes bands for the leaky mode system in comparison with the bound-mode theory. Another interesting point is that in our theory, the side-bands were found to occur roughly 50 cm earlier than predicted by the bound-mode theory. These findings originate from an accurate description of the nonlinear properties and, in particular, of the nonlinearity parameter of the considered waveguide.

Our theoretical and numerical investigations have demonstrated that leaky modes provide modulation instability in both the anomalous and normal dispersion regions. Furthermore, there is always a minimal nonzero background gain for the entire spectral range. It means that the modulation instability can occur for all frequencies. This can be considered as one of a fundamental differences of leaky modes to bound modes.

Within our theory, it is possible to describe a waveguide mode that is excited by arbitrary external or internal sources. Such dipole-fiber systems have important applications in fiber based sensors, non-classical light sources for quantum information and other devices. Consequently, we have applied our model to describe the emission of point sources in hollow-core waveguides and investigated the change of the spontaneous emission rate. Our simulations show that the model can properly describe the spontaneous emission of the dipole if the excited waveguide modes are far enough from the cut of the Green's dyadic. However, in most of the cases, for an accurate description, it is necessary to take into account a relatively high number of modes. In this case, the cut contribution has to be taken into account within the scope of the theory.

We are quite sure that our theory is not restricted to the cases considered here. It has unrevealed potentials and can include other effects

that we have neglected so far due to choice of the initial conditions. For example, it can further be extended to consider nonlinear dispersion effects by solving the master equation in the frequency domain. Additionally, it will be interesting to extend the theory for PT-symmetric systems since in most of the cases, they have an intrinsic gain and loss.

Since leaky modes play a crucial role in a large number of fiber geometries, we think that our theory opens new routes for tailoring the linear and nonlinear pulse propagation in these waveguides. The comparison of the standard theory with our theory reveals that the conventional theory is inappropriate for capturing all phenomena that arise during the propagation of leaky modes. Therefore, we believe that our theory can accurately describe and perform numerical modelling of experimentally observed features not only qualitatively but also quantitatively.

~

BIBLIOGRAPHY

- [5] G. Agrawal: *Nonlinear Fiber Optics*, 3rd edition, Academic Press (San Diego), 2001.
ISBN 0-12-045143-3, cit. on pp. 1–2, 37, 39–40, 44–45, 50, 52, 54, 57–58, 60–61, 66–70, 74–75, 78, 80.
- [6] Y. Kivshar and G. Agrawal: *Optical solitons: From fibers to photonic crystals*, Academic Press (San Diego), 2003.
ISBN 0-12-410590-4, cit. on p. 1.
- [7] J. Kerr: *A new relation between electricity and light: Dielectrified media birefringent*, Phil. Mag. **50**, 337–348 (1875).
DOI 10.1080/14786447508641302, cit. on p. 1.
- [8] J. Kerr: *A new relation between electricity and light: Dielectrified media birefringent (2nd paper)*, Phil. Mag. **50**, 446–458 (1875).
DOI 10.1080/14786447508641319, cit. on p. 1.
- [9] R. W. Boyd: *Nonlinear optics*, 2nd edition, Academic Press (San Diego), 2003.
ISBN 0-12-121682-9, cit. on pp. 1, 37–38.
- [10] A. Hasegawa and M. Matsumoto: *Optical solitons in fibers*, 3rd edition, Springer (Berlin), 2003.
ISBN 3-540-43695-2, cit. on pp. 1–2.
- [11] V. E. Zakharov and A. B. Shabat: *Exact theory of two-dimensional self-focusing and one-dimensional self-modulation of waves in nonlinear media*, Sov. Phys. JETP **34**, 62–69 (1972).
URL jetp.ac.ru/cgi-bin/e/index/e/34/1/p62?a=list, cit. on pp. 1–2.
- [12] M. J. Ablowitz and P. A. Clarkson: *Solitons, nonlinear evolution equations and inverse scattering*, Cambridge University Press (New York), 1991.
ISBN 978-0-521-38730-9, cit. on p. 1.
- [13] J. Satsuma and N. Yajima: *Initial value problems of one-dimensional self-modulation of nonlinear waves in dispersive media*, Prog. Theor. Phys. Suppl. **55**, 284–306 (1974).
DOI 10.1143/ptps.55.284, cit. on p. 2.

- [14] M. A. Foster, K. D. Moll, and A. L. Gaeta: *Optimal waveguide dimensions for nonlinear interactions*, Opt. Express **12**, 2880–2887 (2004).
DOI 10.1364/opex.12.002880, cit. on pp. 2, 41, 44–45, 50.
- [15] S. Afshar and T. Monro: *A full vectorial model for pulse propagation in emerging waveguides with subwavelength structures part I: Kerr nonlinearity*, Opt. Express **17**, 2298–2318 (2009).
DOI 10.1364/oe.17.002298, cit. on pp. 2, 38, 41, 44–45, 50–51, 58, 61, 67.
- [16] G. Li, C. M. de Sterke, and S. Palomba: *General analytic expression and numerical approach for the Kerr nonlinear coefficient of optical waveguides*, Opt. Lett. **42**, 1329–1332 (2017).
DOI 10.1364/ol.42.001329, cit. on pp. 2, 40, 44, 49, 67.
- [17] F. Benabid and P. J. Roberts: *Linear and nonlinear optical properties of hollow core photonic crystal fiber*, J. Mod. Opt. **58**, 87–124 (2011).
DOI 10.1080/09500340.2010.543706, cit. on pp. 2–3.
- [18] P. Russell, P. Hölzer, W. Chang, A. Abdolvand, and J. C. Travers: *Hollow-core photonic crystal fibres for gas-based nonlinear optics*, Nat. Photon. **8**, 278–286 (2014).
DOI 10.1038/nphoton.2013.312, cit. on pp. 3–4.
- [19] S. O. Konorov, A. B. Fedotov, and A. M. Zheltikov: *Enhanced four-wave mixing in a hollow-core photonic crystal fiber*, Opt. Lett. **28**, 1448–1450 (2003).
DOI 10.1364/ol.28.001448, cit. on pp. 3–4.
- [20] R. Sollapur, D. Kartashov, M. Zürich, A. Hoffmann, T. Grigorova, G. Sauer, A. Hartung, A. Schwuchow, J. Bierlich, J. Kobelke, M. Chemnitz, M. A. Schmidt, and C. Spielmann: *Resonance-enhanced multi-octave supercontinuum generation in antiresonant hollow-core fibers*, Sci. Appl. **6**, e17124 (2017).
DOI 10.1038/lssa.2017.124, cit. on p. 3.
- [21] M. Nisoli, S. De Silvestri, O. Svelto, R. Szipöcs, K. Ferencz, C. Spielmann, S. Sartania, and F. Krausz: *Compression of high-energy laser pulses below 5 fs*, Opt. Lett. **22**, 522–524 (1997).
DOI 10.1364/ol.22.000522, cit. on pp. 3, 46, 62.

- [22] S. Hädrich, H. Carstens, J. Rothhardt, J. Limpert, and A. Tünnermann: *Multi-gigawatt ultrashort pulses at high repetition rate and average power from two-stage nonlinear compression*, Opt. Express **19**, 7546–7552 (2011). DOI 10.1364/oe.19.007546, cit. on p. 3.
- [23] C. R. Rosberg, F. H. Bennet, D. N. Neshev, P. D. Rasmussen, O. Bang, W. Krolikowski, A. Bjarklev, and Y. S. Kivshar: *Tunable diffraction and self-defocusing in liquid-filled photonic crystal fibers*, Opt. Express **15**, 12145–12150 (2007). DOI 10.1364/oe.15.012145, cit. on p. 3.
- [24] J. Bethge, A. Husakou, F. Mitschke, F. Noack, U. Griebner, G. Steinmeyer, and J. Herrmann: *Two-octave supercontinuum generation in a water-filled photonic crystal fiber*, Opt. Express **18**, 6230–6240 (2010). DOI 10.1364/oe.18.006230, cit. on p. 3.
- [25] M. Vieweg, T. Gissibl, S. Pricking, B. T. Kuhlmey, D. C. Wu, B. J. Eggleton, and H. Giessen: *Ultrafast nonlinear optofluidics in selectively liquid-filled photonic crystal fibers*, Opt. Express **18**, 25232–25240 (2010). DOI 10.1364/oe.18.025232, cit. on p. 3.
- [26] M. Chemnitz, M. Gebhardt, C. Gaida, F. Stutzki, J. Kobelke, J. Limpert, A. Tünnermann, and M. A. Schmidt: *Hybrid soliton dynamics in liquid-core fibres*, Nat. Commun. **8**, 42 (2017). DOI 10.1038/s41467-017-00033-5, cit. on p. 3.
- [27] H. Crespo, J. T. Mendonca, and A. Dos Santos: *Cascaded highly nondegenerate four-wave-mixing phenomenon in transparent isotropic condensed media*, Opt. Lett. **25**, 829–831 (2000). DOI 10.1364/ol.25.000829, cit. on p. 4.
- [28] A. Snyder and J. Love: *Optical waveguide theory*, Chapman and Hall (New York), 1983. ISBN 0-412-09950-0, cit. on pp. 4–5, 12, 18, 21, 23, 26, 28–29, 44, 46, 72, 88, 96.
- [29] R. Sammut and A. W. Snyder: *Leaky modes on circular optical waveguides*, Appl. Opt. **15**, 477–482 (1976). DOI 10.1364/ao.15.000477, cit. on pp. 5, 23.

- [30] R. Sammut and A. W. Snyder: *Leaky modes on a dielectric waveguide: orthogonality and excitation*, Appl. Opt. **15**, 1040–1044 (1976).
DOI 10.1364/ao.15.001040, cit. on pp. 5, 22–23.
- [31] C. Sauvan, J. P. Hugonin, I. S. Maksymov, and P. Lalanne: *Theory of the spontaneous optical emission of nanosize photonic and plasmon resonators*, Phys. Rev. Lett. **110**, 237401 (2013).
DOI 10.1103/physrevlett.110.237401, cit. on pp. 5, 20, 23.
- [32] A. V. Maslov: *Rigorous calculation of the nonlinear Kerr coefficient for a waveguide using power-dependent dispersion modification*, Opt. Lett. **39**, 4396–4399 (2014).
DOI 10.1364/ol.39.004396, cit. on pp. 5, 40, 49, 67.
- [33] M. M. Elsawy and G. Renversez: *Exact calculation of the nonlinear characteristics of 2D isotropic and anisotropic waveguides*, Opt. Lett. **43**, 2446–2449 (2018).
DOI 10.1364/ol.43.002446, cit. on pp. 5, 40, 49, 67.
- [34] J. D. Jackson: *Classical electrodynamics*, 2nd edition, John Wiley and Sons (New York), 1975.
ISBN 0-471-43132-X, cit. on pp. 8, 94.
- [35] E. A. Muljarov and T. Weiss: *Resonant-state expansion for open optical systems: generalization to magnetic, chiral, and bi-anisotropic materials*, Opt. Lett. **43**, 1978–1981 (2018).
DOI 10.1364/ol.43.001978, cit. on pp. 10–11, 13, 17, 19, 24.
- [36] S. H. Schot: *Eighty years of Sommerfelds radiation condition*, Hist. Math. **19**, 385–401 (1992).
DOI 10.1016/0315-0860(92)90004-U, cit. on p. 11.
- [37] E. A. Muljarov, W. Langbein, and R. Zimmermann: *Brillouin-Wigner perturbation theory in open electromagnetic systems*, Europhys. Lett. **92**, 50010 (2011).
DOI 10.1209/0295-5075/92/50010, cit. on pp. 11, 13, 24.
- [38] M. B. Doost, W. Langbein, and E. A. Muljarov: *Resonant state expansion applied to two-dimensional open optical systems*, Phys. Rev. A **87**, 043827 (2013).
DOI 10.1103/physreva.87.043827, cit. on pp. 11–13, 17–18, 24, 97.
- [39] M. B. Doost, W. Langbein, and E. A. Muljarov: *Resonant-state expansion applied to three-dimensional open optical systems*, Phys. Rev. A **90**, (2014).
DOI 10.1103/physreva.90.013834, cit. on pp. 11, 13, 18–19, 97.

- [40] E. A. Muljarov and W. Langbein: *Resonant-state expansion of dispersive open optical systems: Creating gold from sand*, Phys. Rev. B **93**, (2016).
DOI 10.1103/physrevb.93.075417, cit. on pp. 11, 13.
- [41] D. Marcuse: *Light transmission optics*, 2nd edition, Van Nostrand Reinhold (New York), 1982.
ISBN 0-442-26309-0, cit. on pp. 12, 26, 28–29, 72, 94, 96.
- [42] M. Born and E. Wolf: *Principles of optics*, 7th edition, Cambridge University Press (Cambridge), 1999.
ISBN 0-521-642221, cit. on p. 12.
- [43] P. M. Morse and H. Feshbach: *Methods of theoretical physics*, McGraw-Hill (New York), 1953.
ISBN 978-0-07-043316-8, cit. on pp. 13, 18.
- [44] J. Mathews and R. L. Walker: *Mathematical methods of physics*, 2nd edition, Addison-Wesley (New York), 1964.
ISBN 978-0-80-537002-7, cit. on p. 13.
- [45] C.-T. Tai: *Dyadic Green functions in electromagnetic theory*, 2nd edition, IEEE Press (New York), 1994.
ISBN 0-7803-0449-7, cit. on p. 13.
- [46] L. J. Armitage, M. B. Doost, W. Langbein, and E. A. Muljarov: *Resonant-state expansion applied to planar waveguides*, Phys. Rev. A **89**, (2014).
DOI 10.1103/physreva.89.053832, cit. on p. 13.
- [47] T. Weiss, M. Schäferling, H. Giessen, N. A. Gippius, S. G. Tikhodeev, W. Langbein, and E. A. Muljarov: *Analytical normalization of resonant states in photonic crystal slabs and periodic arrays of nanoantennas at oblique incidence*, Phys. Rev. B **96**, (2017).
DOI 10.1103/physrevb.96.045129, cit. on pp. 13, 18, 37.
- [48] B. A. Fuchs and B. V. Shabat: *Functions of a complex variable and some of their applications*, Pergamon Press (New York), 1964.
ISBN 978-0-08-009404-5, cit. on pp. 13, 17–18.
- [49] S. V. Lobanov, G. Zorinians, W. Langbein, and E. A. Muljarov: *Resonant-state expansion of light propagation in nonuniform waveguides*, Phys. Rev. A **95**, 053848 (2017).
DOI 10.1103/physreva.95.053848, cit. on p. 13.

- [50] E. A. Muljarov and W. Langbein: *Exact mode volume and Purcell factor of open optical systems*, Phys. Rev. B **94**, 235438 (2016).
DOI 10.1103/physrevb.94.235438, cit. on pp. 18–19, 23, 87–88, 92.
- [51] T. Weiss, M. Mesch, M. Schäferling, H. Giessen, W. Langbein, and E. A. Muljarov: *From dark to bright: First-order perturbation theory with analytical mode normalization for plasmonic nanoantenna arrays applied to refractive index sensing*, Phys. Rev. Lett. **116**, 237401 (2016).
DOI 10.1103/physrevlett.116.237401, cit. on pp. 18, 37.
- [52] R. Coccioli, M. Boroditsky, E. Yablonovitch, Y. Rahmat-Samii, and K. Kim: *Smallest possible electromagnetic mode volume in a dielectric cavity*, IEE Proc. Optoelectron. **145**, 391–397 (1998).
DOI 10.1049/ip-opt:19982468, cit. on pp. 19, 87.
- [53] P. T. Leung, S. Y. Liu, and K. Young: *Completeness and orthogonality of quasinormal modes in leaky optical cavities*, Phys. Rev. A **49**, 3057–3067 (1994).
DOI 10.1103/physreva.49.3057, cit. on p. 19.
- [54] P. T. Leung and K. M. Pang: *Completeness and time-independent perturbation of morphology-dependent resonances in dielectric spheres*, J. Opt. Soc. Am. B **13**, 805 (1996).
DOI 10.1364/josab.13.000805, cit. on p. 19.
- [55] P. T. Kristensen, C. Van Vlack, and S. Hughes: *Generalized effective mode volume for leaky optical cavities*, Opt. Lett. **37**, 1649 (2012).
DOI 10.1364/ol.37.001649, cit. on p. 19.
- [56] P. T. Kristensen and S. Hughes: *Modes and mode volumes of leaky optical cavities and plasmonic nanoresonators*, ACS Photon. **1**, 2–10 (2013).
DOI 10.1021/ph400114e, cit. on p. 19.
- [57] M. Chemnitz and M. A. Schmidt: *Single mode criterion—a benchmark figure to optimize the performance of nonlinear fibers*, Opt. Express **24**, 16191–16205 (2016).
DOI 10.1364/oe.24.016191, cit. on pp. 21, 44.

- [58] E. A. Marcatili and R. A. Schmelzter: *Hollow metallic and dielectric waveguides for long distance optical transmission and lasers*, Bell Syst. Tech. J. **43**, 1783–1809 (1964).
DOI 10.1002/j.1538-7305.1964.tb04108.x, cit. on pp. 23, 46–48, 62, 94.
- [59] A. W. Snyder and D. J. Mitchell: *Leaky mode analysis of circular optical waveguides*, Opto-electronics **6**, 287–296 (1974).
DOI 10.1007/bf01423378, cit. on p. 23.
- [60] A. W. Snyder: *Leaky-ray theory of optical waveguides of circular cross section*, Appl. Phys. **4**, 273–298 (1974).
DOI 10.1007/bf00928381, cit. on p. 23.
- [61] A. W. Snyder and J. D. Love: *Tunnelling leaky modes on optical waveguides*, Opt. Commun. **12**, 326–328 (1974).
DOI 10.1016/0030-4018(74)90026-1, cit. on p. 23.
- [62] I. S. Gradshteyn and I. M. Ryzhik: *Table of integrals, series, and products*, 8th edition, Academic Press (Amsterdam), 2014.
ISBN 978-0-12-384933-5, cit. on pp. 30, 97.
- [63] H. Ebendorff-Heidepriem, P. Petropoulos, S. Asimakis, V. Finazzi, R. C. Moore, K. Frampton, F. Koizumi, D. J. Richardson, and T. M. Monro: *Bismuth glass holey fibers with high nonlinearity*, Opt. Express **12**, 5082–5087 (2004).
DOI 10.1364/opex.12.005082, cit. on pp. 30, 45, 93–94.
- [64] S. Kedenburg, T. Gissibl, T. Steinle, A. Steinmann, and H. Giessen: *Towards integration of a liquid-filled fiber capillary for supercontinuum generation in the 1.2-2.4 micrometer range*, Opt. Express **23**, 8281–8289 (2015).
DOI 10.1364/oe.23.008281, cit. on pp. 30, 45.
- [65] S. Both and T. Weiss: *First-order perturbation theory for changes in the surrounding of open optical resonators*, Opt. Lett. **44**, 5917–5920 (2019).
DOI 10.1364/ol.44.005917, cit. on p. 37.
- [66] C. Sauteret, J. P. Hermann, R. Frey, F. Pradere, J. Ducuing, R. H. Baughman, and R. R. Chance: *Optical nonlinearities in one-dimensional-conjugated polymer crystals*, Phys. Rev. Lett. **36**, 956–959 (1976).
DOI 10.1103/physrevlett.36.956, cit. on p. 37.

- [67] L. H. Acioli, A. S. L. Gomes, and J. R. R. Leite: *Measurement of high-order optical nonlinear susceptibilities in semiconductor doped glasses*, Appl. Phys. Lett. **53**, 1788–1790 (1988). DOI 10.1063/1.99781, cit. on p. 37.
- [68] B. Lawrence, W. E. Torruellas, M. Cha, M. L. Sundheimer, G. I. Stegeman, J. Meth, S. Etemad, and G. Baker: *Identification and role of two-photon excited states in a pi-conjugated polymer*, Phys. Rev. Lett. **73**, 597–600 (1994). DOI 10.1103/physrevlett.73.597, cit. on p. 37.
- [69] R. L. Sutherland: *Handbook of nonlinear optics*, 2nd edition, Marcel Dekker (New York), 2003. ISBN 0-8247-4243-5, cit. on p. 43.
- [70] P. Russell: *Photonic crystal fibers*, Science **299**, 358–362 (2003). DOI 10.1126/science.1079280, cit. on p. 45.
- [71] K. Kikuchi and K. Taira: *Highly nonlinear bismuth oxide-based glass fibres for all-optical signal processing*, Electron. Lett. **38**, 166–167 (2002). DOI 10.1109/ofc.2002.1036560, cit. on p. 45.
- [72] S. Kedenburg, M. Vieweg, T. Gissibl, and H. Giessen: *Linear refractive index and absorption measurements of nonlinear optical liquids in the visible and near-infrared spectral region*, Opt. Mat. Express **2**, 1588 (2012). DOI 10.1364/ome.2.001588, cit. on pp. 45, 47.
- [73] K. Kedenburg, A. Steinmann, R. Hegenbarth, T. Steinle, and H. Giessen: *Nonlinear refractive indices of nonlinear liquids: Wavelength dependence and influence of retarded response*, Appl. Phys. B **117**, 803–816 (2014). DOI 10.1007/s00340-014-5833-y, cit. on pp. 45, 47.
- [74] M. Chemnitz, R. Scheibinger, C. Gaida, M. Gebhardt, F. Stutzki, S. Pumpe, J. Kobelke, A. Tünnermann, J. Limpert, and M. A. Schmidt: *Thermodynamic control of soliton dynamics in liquid-core fibers*, Optica **5**, 695–703 (2018). DOI 10.1364/optica.5.000695, cit. on p. 45.
- [75] M. Nisoli, S. Stagira, S. De Silvestri, O. Svelto, S. Sartania, Z. Cheng, M. Lenzner, C. Spielmann, and F. Krausz: *A novel-high energy pulse compression system: Generation of multigigawatt sub 5 fs pulses*, Appl. Phys. B **65**, 189–196 (1997). DOI 10.1007/s003400050263, cit. on p. 46.

- [76] B. Schenkel, J. Biegert, U. Keller, C. Vozzi, M. Nisoli, G. Sansone, S. Stagira, S. De Silvestri, and O. Svelto: *Generation of 38-fs pulses from adaptive compression of a cascaded hollow fiber supercontinuum*, *Opt. Lett.* **28**, 1987–1989 (2003). DOI 10.1364/ol.28.001987, cit. on p. 46.
- [77] M. Dinu, F. Quochi, and H. Garcia: *Third-order nonlinearities in silicon at telecom wavelengths*, *Appl. Phys. Lett.* **82**, 2954–2956 (2003). DOI 10.1063/1.1571665, cit. on p. 47.
- [78] P. P. Ho and R. R. Alfano: *Optical Kerr effect in liquids*, *Phys. Rev. A* **20**, 2170–2187 (1979). DOI 10.1103/physreva.20.2170, cit. on p. 47.
- [79] A. Couairon and A. Mysyrowicz: *Femtosecond filamentation in transparent media*, *Phys. Reports* **441**, 47–189 (2007). DOI 10.1016/j.physrep.2006.12.005, cit. on p. 51.
- [80] K. J. Blow and D. Wood: *Theoretical description of transient stimulated Raman scattering in optical fibers*, *J. Quantum Elect.* **25**, 2665–2673 (1989). DOI 10.1109/3.40655, cit. on pp. 52, 80.
- [81] I. Cristiani, R. Tediosi, L. Tartara, and V. Degiorgio: *Dispersive wave generation by solitons in microstructured optical fibers*, *Opt. Express* **12**, 124–135 (2004). DOI 10.1364/opex.12.000124, cit. on pp. 52, 80.
- [82] J. M. Dudley, G. Genty, and S. Coen: *Supercontinuum generation in photonic crystal fiber*, *Rev. Mod. Phys.* **78**, 1135–1184 (2006). DOI 10.1103/revmodphys.78.1135, cit. on pp. 52, 54.
- [83] A. M. Zheltikov: *Let there be white light: Supercontinuum generation by ultrashort laser pulses*, *Phys. Uspekhi* **49**, 605 (2006). DOI 10.3367/ufnr.0176.200606d.0623, cit. on p. 54.
- [84] R. L. Carman, R. Y. Chiao, and P. L. Kelley: *Observation of degenerate stimulated four-photon interaction and four-wave parametric amplification*, *Phys. Rev. Lett.* **17**, 1281 (1966). DOI 10.1103/physrevlett.17.1281, cit. on p. 57.

- [85] R. H. Stolen, J. E. Bjorkholm, and A. Ashkin: *Phase-matched three-wave mixing in silica fiber optical waveguides*, Appl. Phys. Lett. **24**, 308–310 (1974).
DOI 10.1063/1.1655195, cit. on p. 57.
- [86] C. Lin, W. A. Reed, A. D. Pearson, and H. T. Shang: *Phase matching in the minimum-chromatic-dispersion region of single-mode fibers for stimulated four-photon mixing*, Opt. Lett. **6**, 493–495 (1981).
DOI 10.1364/ol.6.000493, cit. on p. 57.
- [87] K. O. Hill, D. C. Johnson, B. S. Kawasaki, and R. I. MacDonald: *CW three-wave mixing in single-mode optical fibers*, J. Appl. Phys. **49**, 5098–5106 (1978).
DOI 10.1063/1.324456, cit. on p. 57.
- [88] R. Stolen and J. Bjorkholm: *Parametric amplification and frequency conversion in optical fibers*, J. Quantum Elect. **18**, 1062–1072 (1982).
DOI 10.1109/jqe.1982.1071660, cit. on p. 57.
- [89] P. Baldeck and R. Alfano: *Intensity effects on the stimulated four photon spectra generated by picosecond pulses in optical fibers*, J. Lightwave Technol. **5**, 1712–1715 (1987).
DOI 10.1109/jlt.1987.1075465, cit. on p. 57.
- [90] K. Washio, K. Inoue, and S. Kishida: *Efficient large-frequency-shifted three-wave mixing in low dispersion wavelength region in single-mode optical fibre*, Electron. Lett. **16**, 658–660 (1980).
DOI 10.1049/el:19800467, cit. on p. 57.
- [91] M. E. Marhic, N. Kagi, T. K. Chiang, and L. G. Kazovsky: *Broadband fiber optical parametric amplifiers*, Opt. Lett. **21**, 573–575 (1996).
DOI 10.1364/ol.21.000573, cit. on p. 57.
- [92] K. Inoue, K. Nakanishi, K. Oda, and H. Toba: *Crosstalk and power penalty due to fiber four-wave mixing in multichannel transmissions*, J. Lightwave Technol. **12**, 1423–1439 (1994).
DOI 10.1109/50.317531, cit. on p. 57.

- [93] F. Forghieri, R. W. Tkach, A. R. Chraplyvy, and D. Marcuse: *Reduction of four-wave mixing crosstalk in WDM systems using unequally spaced channels*, *Photon. Tech. Lett.* **6**, 754–756 (1994).
DOI 10.1109/68.300184, cit. on p. 57.
- [94] I. H. Malitson: *Interspecimen comparison of the refractive index of fused silica*, *J. Opt. Soc. Am.* **55**, 1205–1209 (1965).
DOI 10.1364/josa.55.001205, cit. on pp. 59, 72.
- [95] A. Börzsönyi, Z. Heiner, M. P. Kalashnikov, A. P. Kovács, and K. Osvay: *Dispersion measurement of inert gases and gas mixtures at 800 nm*, *Appl. Opt.* **47**, 4856–4863 (2008).
DOI 10.1364/ao.47.004856, cit. on pp. 59, 72.
- [96] M. Zeisberger, A. Hartung, and M. A. Schmidt: *Understanding dispersion of revolver-type antiresonant hollow-core fibers*, *Fibers* **6**, 68 (2018).
DOI 10.3390/fib6040068, cit. on p. 58.
- [97] W. van Saarloos and P. C. Hohenberg: *Fronts, pulses, sources and sinks in generalized complex Ginzburg-Landau equations*, *Physica D* **56**, 303–367 (1992).
DOI 10.1016/0167-2789(92)90175-m, cit. on p. 68.
- [98] V. A. Vasiliev, Y. M. Romanovskii, D. S. Chernavskii, and V. G. Yakhno: *Autowave processes in kinetic systems: Spatial and temporal self-organisation in physics, chemistry, biology, and medicine*, D. Reidel Publishing Company (Boston), 1987. ISBN 978-94-010-8172-6, cit. on p. 71.
- [99] P. Grelu and N. Akhmediev: *Dissipative solitons for mode-locked lasers*, *Nat. Photon.* **6**, 84–92 (2012).
DOI 10.1038/nphoton.2011.345, cit. on p. 71.
- [100] H. Garcia, A. M. Johnson, F. A. Oguama, and S. Trivedi: *New approach to the measurement of the nonlinear refractive index of short lengths of silica and erbium-doped fibers*, *Opt. Lett.* **28**, 1796–1798 (2003).
DOI 10.1364/OL.28.001796, cit. on p. 72.
- [101] A. Börzsönyi, Z. Heiner, A. P. Kovács, M. P. Kalashnikov, and K. Osvay: *Measurement of pressure dependent nonlinear refractive index of inert gases*, *Opt. Express* **18**, 25847–25854 (2010).
DOI 10.1364/oe.18.025847, cit. on p. 72.

- [102] N. M. Litchinitser, A. K. Abeeluck, C. Headley, and B. J. Eggleton: *Antiresonant reflecting photonic crystal optical waveguides*, *Opt. Lett.* **27**, 1592–1594 (2002). DOI 10.1364/ol.27.001592, cit. on p. 72.
- [103] E. Betzig and R. J. Chichester: *Single molecules observed by near-field scanning optical microscopy*, *Science* **262**, 1422–1425 (1993). DOI 10.1126/science.262.5138.1422, cit. on p. 87.
- [104] T. H. Taminiau, F. D. Stefani, F. B. Segerink, and N. F. van Hulst: *Optical antennas direct single-molecule emission*, *Nat. Photon.* **2**, 234–237 (2008). DOI 10.1038/nphoton.2008.32, cit. on p. 87.
- [105] T. M. Monro, S. Warren-Smith, E. P. Schartner, A. Francois, S. Heng, H. Ebendorff-Heidepriem, and S. Afshar: *Sensing with suspended-core optical fibers*, *Opt. Fiber Technol.* **16**, 343–356 (2010). DOI 10.1016/j.yofte.2010.09.010, cit. on p. 87.
- [106] D. G. Bergman and M. I. Stockman: *Surface plasmon amplification by stimulated emission of radiation: Quantum generation of coherent surface plasmons in nanosystems*, *Phys. Rev. Lett.* **90**, 027402 (2003). DOI 10.1103/physrevlett.90.027402, cit. on p. 87.
- [107] R. F. Oulton, V. J. Sorger, T. Zentgraf, R. Ma, C. Gladden, L. Dai, G. Bartal, and X. Zhang: *Plasmon lasers at deep subwavelength scale*, *Nature* **461**, 629–632 (2009). DOI 10.1038/nature08364, cit. on p. 87.
- [108] I. S. Maksymov, M. Besbes, J. P. Hugonin, J. Yang, A. Beveratos, I. Sagnes, I. Robert-Philip, and P. Lalanne: *Metal-coated nanocylinder cavity for broadband nonclassical light emission*, *Phys. Rev. Lett.* **105**, 180502 (2010). DOI 10.1103/physrevlett.105.180502, cit. on p. 87.
- [109] J. T. Choy, B. J. M. Hausmann, T. M. Babinec, I. Bulu, M. Khan, P. Maletinsky, A. Yacoby, and M. Loncar: *Enhanced single-photon emission from a diamond-silver aperture*, *Nat. Photon.* **5**, 738–743 (2011). DOI 10.1038/nphoton.2011.249, cit. on p. 87.

- [110] M. Khajavikhan, A. Simic, M. Katz, J. H. Lee, B. Slutsky, A. Mizrahi, V. Lomakin, and Y. Fainman: *Thresholdless nanoscale coaxial lasers*, *Nature* **482**, 204–207 (2012).
DOI 10.1038/nature10840, cit. on p. 87.
- [111] E. M. Purcell: *Spontaneous emission probabilities at radio frequencies*, *Phys. Rev.* **69**, 681 (1946).
DOI 10.1103/PhysRev.69.37, cit. on pp. 87, 92.
- [112] W. Zakowicz and M. Janowicz: *Spontaneous emission in the presence of a dielectric cylinder*, *Phys. Rev. A* **62**, 013820 (2000).
DOI 10.1103/physreva.62.013820, cit. on p. 88.
- [113] T. Søndergaard and B. Tromborg: *General theory for spontaneous emission in active dielectric microstructures: Example of a fiber amplifier*, *Phys. Rev. A* **64**, 033812 (2001).
DOI 10.1103/physreva.64.033812, cit. on p. 88.
- [114] M. R. Henderson, S. Afshar, A. D. Greentree, and T. M. Monro: *Dipole emitters in fiber: Interface effects, collection efficiency and optimization*, *Opt. Express* **19**, 16182 (2011).
DOI 10.1364/oe.19.016182, cit. on p. 88.
- [115] S. Afshar, S. C. Warren-Smith, and M. T. M.: *Enhancement of fluorescence-based sensing using microstructured optical fibres*, *Opt. Express* **15**, 17891 (2007).
DOI 10.1364/oe.15.017891, cit. on p. 88.
- [116] S. C. Warren-Smith, S. Afshar, and T. M. Monro: *Theoretical study of liquid-immersed exposed-core microstructured optical fibers for sensing*, *Opt. Express* **16**, 9034 (2008).
DOI 10.1364/oe.16.009034, cit. on pp. 88, 93.
- [117] S. Afshar, Y. Ruan, S. C. Warren-Smith, and T. M. Monro: *Enhanced fluorescence sensing using microstructured optical fibers: A comparison of forward and backward collection modes*, *Opt. Lett.* **33**, 1473–1476 (2008).
DOI 10.1364/ol.33.001473, cit. on p. 88.
- [118] X. Brokmann, L. Coolen, J. Hermier, and M. Dahan: *Emission properties of single CdSe/ZnS quantum dots close to a dielectric interface*, *Chem. Phys.* **318**, 91–98 (2005).
DOI 10.1016/j.chemphys.2005.06.032, cit. on p. 88.

- [119] P. Anger, P. Bharadwaj, and L. Novotny: *Enhancement and quenching of single-molecule fluorescence*, Phys. Rev. Lett. **96**, 113002 (2006).
DOI 10.1103/physrevlett.96.113002, cit. on p. 88.
- [120] L. Novotny and B. Hecht: *Principles of nano-optics*, Cambridge University Press (Cambridge), 2006.
ISBN 0-521-53988-9, cit. on pp. 88, 92.



ACKNOWLEDGMENTS

At this place, I would like to thank all the people who helped and supported me throughout this time.

- Jun.-Prof. Dr. Thomas Weiss for giving me the opportunity to work at the 4th Physics Institute, for all his guidance, support, enthusiasm, advice and patience, for making everything possible and for the opportunity to get valuable input at numerous conferences and meetings.
- Prof. Dr. Günter Wunner for kindly agreeing to be my co-advisor despite his retirement and Prof. Dr. Stefanie Barz for being the head of the examination committee.
- Prof. Dr. Harald Gießen for his great effort to make the 4th Physics Institute fantastic working place and for all of his inspiring talks.
- Dr. Christine von Rekowski for all administrative affairs.
- Dr. Rostyslav Semenyshyn for his advice and interesting non-scientific discussions.
- Swaathi Upendar for being a great officemate and for her help with English.
- Steffen Both and Sascha Böhrkircher for their numerous help with finite element simulations and reading my thesis draft.
- Josselin Defrance for interesting scientific and non-scientific discussions.
- Dr. Maxim Nesterov for the numerous non-scientific discussions.
- Dr. Martin Schäferling for being my officemate and for the nice office door.
- All my current colleagues and former members of the 4th Physics Institute for the time spent together.

I also want to thank all my previous teachers and supervisors for their effort and guidance. Especially, I would like to highlight Umida Butanova, Bakhtiyor Ismoilov, Quronboy Botirov, Dr. Khatam Ashurov, Dr. Sadulla Tadjimuratov, Dr. Eduard Tsoy, Prof. Dr. Fatkhulla Abdulayev and Prof. Dr. Abdulaziz Abdumalikov as well as my friends Pulat Tadjimuratov, Khurshed Khamrakulov and Qodir Ismoilov.

Besides, I would like to thank my landlady Dr. Gisela Lackenbauer-Eisenmann for her hospitality and support.

Finally, my deepest thanks go to my parents Norgul (opam) and Mukhiddin (akam) as well as to my wife Kamila and my daughter Zarina. Without their constant support and patience this thesis would not have been possible.



CURRICULUM VITÆ

NAME	Izzatjon Mukhiddinovich Allayarov
BORN	06.08.1988 in Gurlan, Uzbekistan
CITIZENSHIP	Uzbek
CIVIL STATUS	Married
PERSONAL E-MAIL	allayarov.i@gmail.com
2020	Ph.D. thesis: "Theory of Leaky Mode Propagation in Optical Waveguide Geometries", University of Stuttgart, advisor: Jun.-Prof. Dr. Thomas Weiss
2015–2020	Research assistant, group of Jun.-Prof. Dr. Thomas Weiss, 4th Physics Institute, University of Stuttgart
2013–2015	Research assistant, group of Prof. Dr. Fatkhulla Abdullaev, Physical-Technical Institute, Uzbek Academy of Sciences.
2012	Military service.
2012	Master work: "Dynamics of impulses in microstructured fibers", advisor: Dr. Eduard Tsoy.
2010–2012	Master of Science in Theoretical Physics, National University of Uzbekistan.
2006–2010	Laboratory assistant, group of Dr. Khatam Ashurov, Arifov Institute of Electronics (at present Institute of Ion-Plasma and Laser Technologies), Uzbek Academy of Sciences.
2010	Graduate work: "Dynamics of fronts in nonlinear optical systems", advisor: Dr. Eduard Tsoy.
2006–2010	Bachelor of Science in Physics, National University of Uzbekistan.
2003–2006	40th specialized school, Gurlan.
1994–2003	20th middle school, Gurlan.

~

COLOPHON

This thesis was typeset with \LaTeX 2 ϵ using Robert Slimbach's Minion Pro font. The style was inspired by Robert Bringhurst's "*The Elements of Typographic Style*". It is available for \LaTeX via CTAN as CLASSICTHESIS.

